SURFACE FUNCTIONALIZATION OF GRAPHENE OXIDE FOR APPLICATION IN ORGANIC SOLAR CELLS

by

FOKOTSA VICTOR MOLEFE

submitted in accordance with the requirements
for the degree of

DOCTOR OF PHILOSOPHY

in the subject

PHYSICS

at the

UNIVERSITY OF SOUTH AFRICA

SUPERVISOR: PROF M S DHLAMINI

CO-SUPERVISORS: PROF B M MOTHUDI

JANUARY 2023

DECLARATION

Name: FOKOTSA VICTOR MOLEFE

Student number: 57649936

Degree: PHYLOSOPHIAE DOCTOR (PhD)

Exact wording of the title of the thesis as appearing on the electronic copy submitted for examination:

SURFACE FUNCTIONALIZATION OF GRAPHENE OXIDE FOR APPLICATION IN ORGANIC SOLAR CELLS.

I declare that the above thesis is my own work and that all the sources that I have used or quoted have been indicated and acknowledged by means of complete references.

I further declare that I submitted the thesis to originality checking software and that it falls within the accepted requirements for originality.

I further declare that I have not previously submitted this work, or part of it, for examination at Unisa for another qualification or at any other higher education institution.

(The thesis will not be examined unless this statement has been submitted.)

SIGNATURE

January 2023

DATE

Dedications

To my kids (Lehakoe and Kgalaletso) who were born while I was busy with my PhD and sincere gratitude goes to saint my mother (MaFokotsa) who guided me into intellectual pursuit.

"To God Be the Glory"

Looking to the future is the order of higher education. I'm shaping mine through Science.

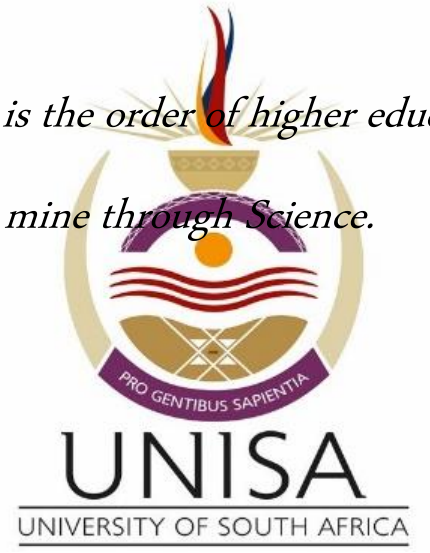

Acknowledgements

The research project conducted herein would not have been possible without considerable assistance from all the members of the physics department at University of South Africa (UNISA) including Postgraduate School at UNISA for advices and the training courses. Continuous support and funding from the National Research Foundation (NRF) of South Africa (SA), Department of Science and Technology (DST) under grant UID: 94951 and 111280 are highly acknowledged. Further financial support from the College of Science Engineering and Technology (CSET), School of Science (SoS) UNISA-Physics Department is appreciated.

Supervision

The PhD research work was supervised by Professor Mokhotjwa S. Dhlamini and co-supervised by Professor Bakang M. Mothudi from the University of South Africa (UNISA), Florida Science Campus in South Africa. Additional contribution to the work was from Professor Johann Bouclé from the Université de Limoges/CNRS, Limoges Cedex in France with the device fabrication, characterization and analysis of data.

I am immensely grateful and I express my enormous gratitude to Prof M.S. Dhlamini for his exceptional supervision, encouragement, guidance and the sustained support, he moulded it.

Collaboration

- The Université de Limoges/CNRS with the fabrication of graphene based solar cell devices, measurements for the analysis of the charge transfer between the donor and acceptor layers.

Additional Contributors

- Prof Mohammed Khenfouch for guidance with preparation of graphene oxide (GO).
- Prof Luyanda Lunga Noto for the PL, life-time measurements and luminescence mechanisms. Not forgetting his mentorship on research writing expertise and inviting me to contribute in scientific book chapters.
- Dr Mohammed Hamzah with the growth of holmium doped GO composites.

- Dr Langutani Eulenda Mathevula for assisting with FTIR and Raman measurements.
- Dr Sefako John Mofokeng for assisting with the PL measurements and discussions.
- Mr Mbongo Mduduzi who assisted with XRD measurements.
- Dr Seithati Angelina Qotso for fruitful discussions.

Special thanks go to Dr Youseff and Hesham from Université de Limoges/CNRS for their assistance in stepwise fabrication of solar cell devices and characterization thereof.

In this context I also thank the University of South Africa (UNISA) and the Université de Limoges/CNRS for supporting the international collaboration leading to the development of photovoltaic devices.

I wish to express my sincere heartfelt gratitude towards my entire family (**Batlokoa & Ditjhele**) alongside my best friends. I have lost many valuable people along this journey and I succeeding is because of their spirit guiding me. God blessed me with a glorious family: **Mpho (fiancé), Lehakoe (son) and Kgalaletso (daughter)** to circumvent for those I lost. I deeply appreciate patient understanding of my fiancé and her unfaltering support ❤️. I will always cherish your combined contributions towards the success of this astonishing work.

Ke lebohe Modimo wa lesedi wa Rammoloki, Mojari wa ditshito tsa batho Tlhatlhamacholo ka bophelo le bohlale boo a mphileng bona, kesa phela ka paballo yahae. Lesedi… Khanya!!

Ho Balefe (Batlokoa) batho baha Nkgaodise ba seala se kgaohile Motonosi!
Ha sea kgaoha se entse lehohoba!
Batho ba ha Makoro, ba mankga lefotha le mohla hosa hlajwang, lentse lenkga!
Batho ba tladiatsana e bohale le tswaka!

KGOMO KOPANYA DIBOKO,

Batho baha Malakoane Ditjhele baha Tsimane!
Batho ba sehwana se molalana Kobedi!
Se kgang metsi, seise ho morena thabeng, sere morena bona ke hlabile!

KERE KGOTSO, PULA, NALA, BASOTHO. HA DIATE TSA MORA WA LONA!

Abstract

The enormous increase in global energy demand concomitant the environmental impact of non-renewable fossil fuels led to exploration of energy sources that are safe, cheaper and sustainable. Within a range of renewable technologies, photovoltaics (PVs) are an emerging way of effectively generating sustainable energy. In photovoltaic devices, the most important aspect is the power conversion efficiency (PCE) which is driven by the crystal structure of the organic polymers, the surface morphology of the thin film and the choice of electron donor and acceptor materials. Multiple routes have been taken to achieve efficient charge transfer between poly(3-hexylthiophene) (P3HT) and graphene, but to the best that we can tell, not much has been done on the use of graphene oxide tailored with rare earth ions and other semiconductor materials.

The conducted research work is devoted to preparation of nanomaterials, growth of thin films and fabrication of devices based on P3HT, holmium (Ho), zinc oxide (ZnO) and graphene oxide (GO). These materials were chosen owing to their superior properties and abundance and they were prepared and deposited using simple synthesis routes and deposition techniques. The primary focus was to investigate the structural, morphological, spectroscopic and solar device properties of heterostructure films for application in organic photovoltaic cells. The properties of the thin films were analysed using X-ray diffraction (XRD), Raman spectroscopy, Fourier transform infrared spectroscopy (FTIR), scanning electron microscopy (SEM), UV-visible near-infrared spectroscopy (UV/VIS/NIR), Photoluminescence spectroscopy (PL), Time-correlated single photon counting (TCSPC) and Keithley 2400 technique, respectively.

This work began with the successful growth of P3HT and GO/P3HT thin films using the drop coating method. Properties of these thin films were investigated and found to have amorphous and crystalline domains and they revealed the interaction through a decrease in lattice spacing, an indication of strain on the thin films. The presence of GO changed the surface morphology to flaky-like nanostructures, as seen from SEM images. The FTIR spectra presented various vibrational frequencies symbolic of the interactions at the interface between GO/P3HT thin films. Further ionic interactions are revealed by the increase in absorbance and broadening of the absorption spectra of GO/P3HT thin films. The doping of GO with Ho was also found to impact absorption properties of P3HT positively. The

quenching of P3HT emission, ideal for photovoltaic applications was observed when grown with GO which indicates an efficient donor-accepter charge transfer process.

In an attempt to attain an efficient donor regioregular P3HT as it is a vital component for better performance of organic solar cells (OSC), we investigated the effect of deposition methods. The evaluated deposition methods for the growth of P3HT thin films operate in the absence of a vacuum and they produced thin films of different thicknesses. The crystallinity of P3HT revealed strong thickness dependence where 30 nm thin film had a low diffraction intensity and 148 nm thin film revealed the highest crystallinity. Raman analysis confirmed the high structural ordering of P3HT in terms of thicker thin films. A uniform P3HT thin film morphology was produced using the spin coating method. The increase in thin film thickness led to variations in absorption spectra due to change in defect states within the bandgap of P3HT. The luminescence properties revealed an increase in emission intensity of P3HT with the increment in the thin film thickness due to the increase in defect density.

We successfully applied the GO/P3HT, ZnO/P3HT and GO/ZnO/P3HT design architecture using spin coating method towards device fabrication. The crystalline structure of P3HT and GO were confirmed using XRD analytical technique where ZnO crystallized into hexagonal wurtzite structure. The chemical stoichiometry from EDS suggested the absence of impurities in the GO/ZnO/P3HT thin films. SEM results presented GO sheets intercalated in P3HT upon interaction. The bonding interactions from FTIR confirmed alteration of P3HT structure upon interaction with GO through a decrease in average conjugation length from 1.20 to 1.12. We witnessed a reduction in band gap energy which caused a decrease in energetic driving force for GO/P3HT. These observations correlated very well with the *J-V* characteristics whereby the incorporation of GO into GO/P3HT and GO/ZnO/P3HT devices yielded performance deterioration with a reduction of ~ 38 % in energy conversion efficiency. Thus, this makes ZnO/P3HT the most efficient device compared to GO/P3HT and GO/ZnO/P3HT devices. The fluorescent decay curves revealed a decline in exciton lifetime depicting a quicker charge transfer from P3HT to GO which resulted into a decrease in exciton diffusion length.

Keywords

GO, ZnO, P3HT, GO/ZnO/P3HT, Charge-transfer, Organic Solar Cells, Layered Nanostructures.

Abbreviations and Acronyms

CL	–	Cathodoluminescence
CT	–	Charge Transfer
DFT	–	Density Functional Theory
EDS	–	Energy Dispersive Spectroscopy
ET	–	Energy Transfer
ETL	–	Electron Transport Layer
FE-SEM	–	Field Emission - Scanning Electron Microscopy
FF	–	Fill Factor
FWHM	–	Full Width at Half Maximum
GO	–	Graphene Oxide
HTL	–	Hole Transport Layer
ITO	–	Indium Tin Oxide
JCPDS	–	Joint Committee on Powder Diffraction Standards
OPV	–	Organic Photovoltaic
P3HT	–	Poly(3-Hexylthiophene)
PCE	–	Power Conversion Efficiency
PL	–	Photoluminescence
PV	–	Photovoltaics
RE	–	Rare Earth
SEM	–	Scanning Electron Microscopy
TCSPC	–	Time Correlated Single Photon Counting
UV/VIS/NIR	–	Ultraviolet - Visible – Near Infrared
XRD	–	X-ray Diffraction

"Science knowledge changes as we discover new evidence. Technology helps us find this evidence"

-Unknown

I sure believe this is doable via Nanoscience and Nanotechnology.

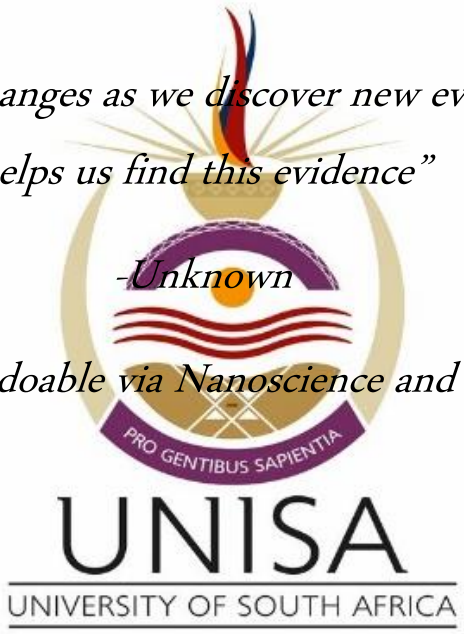

Table of Contents

List of Figures

"Sustainable development is development that meets the needs of the present without compromising the ability of future generations to meet their own needs"

-IISD.

I strongly believe solar cells can lead us to sustainable development without compromising what the future holds for generations to come.

Chapter 1: Introduction

1.1 Overview

Figure 1.1 depicts the map of the location of lights on Earth's surface. The white dots on the map represents lights found in various cities, ships at sea level and many other light sources. By having a look at Africa, one can see that it is largely void of illuminated cities in comparison to other continents which is symbolic of energy crisis. Government officials in Africa needs to find means of expanding the energy capacity because the energy demand is high and extremely expensive. The high energy demand is due to the economic growth in the continent. When it comes to South Africa, the poor electricity supply is brought about by the municipalities which fails to build proper infrastructures for good distribution.

Figure 1. 1 Satellite image of the world at Night [1].

The significant energy challenge is brought about by factors such as access to modern energy services and the traditional energy systems. After recognising the aforementioned energy challenges, we got motivated to prioritise fabrication of solar cell devices that will be used to draw solar radiation and convert it into electrical energy. With the use of solar cells, the African continent which is well blessed with sunlight can utilise the free and clean solar energy to light up remote and isolated houses that do not have means of connecting to the electricity grid. The development of solar cell devices is not targeting the disadvantaged countries only but the rest of the world for sustainable development.

1.2 Research Motivation and Rationale

Figure 1.2 represents the potential of Sub-Saharan Africa (SSA) with the huge amount of radiation it receives. The present research work is motivated by utilisation of this radiation towards the continent's industrialization needs with multiple technological innovations that will enable collection, conversion and storage of energy. The success in converting solar energy into electricity will ensure progress in one of Millennium Development goals published by the United Nations in 2000 whereby we need to ensure sustainable development by promoting renewable energies [2].

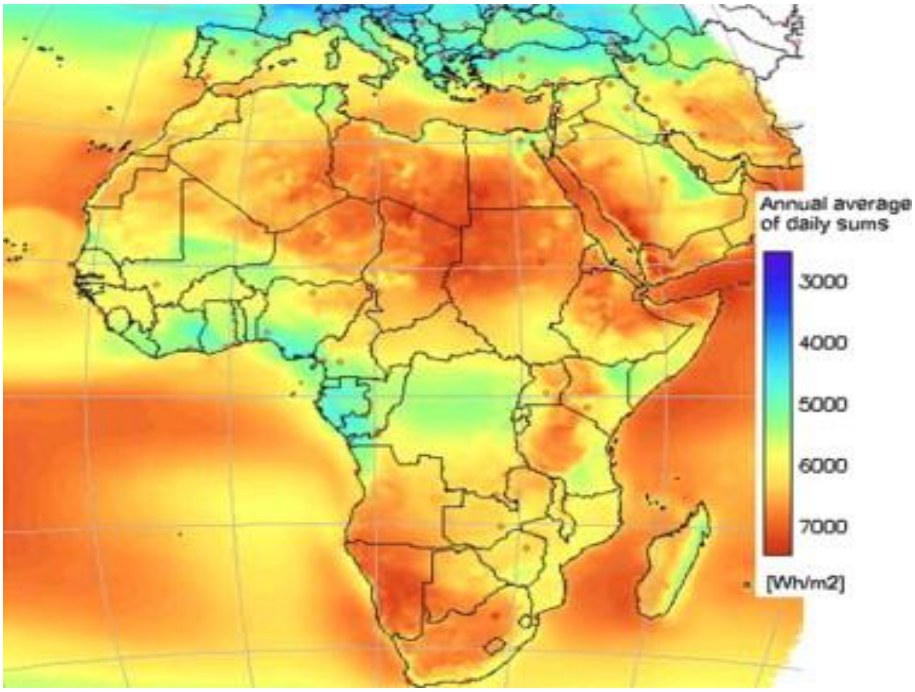

Figure 1. 2 Solar maps of Africa [3].

It is well known that fossil fuels are getting depleted and now energies generated using water, wind, geothermal energy or radiation from the sun respectively are endless and they pose no harm to the environment in terms of gas emissions. In the current project main focus is on solar energy because the earth's surface is receiving 174 PW which is way greater than 15 TW of power consumed globally [4]. This puts solar energy in the forefront as the most promising source of renewable energy (RE) for it can be converted into electrical energy using mechanisms of photovoltaics. The project involves preparation of materials in the nanometre regime and their utilisation for systematic growth of layered nanostructures using spin-coating method for solar cell devices. Development of solar cell devices which harness energy from the sun will help to reinforce energy security in most of the SSA regions where

it is sufficiently available. This energy will improve the quality of life of the people in rural areas by providing electricity for the lighting and powering essential appliances and devices at homes, businesses and public facilities [5].

To date in the field of organic solar cells, polymers are the most efficient donor materials. The primary goal of this research was to explore the use of graphene derivatives as an acceptor material in hybrid solar cells and to establish the power generation mechanism. The use of this carbon containing material will assist with enhancement of flexibility of devices when it comes into contact with polymer material. The mandate of this research was to fine-tune the interface of layered nanostructures for efficacy of the solar cells using nanostructured materials wherein P3HT is the donor material, ZnO plays the role of an interfacial layer and GO being the acceptor. All these materials were engineered at the nanoscale through the field of nanoscience and the solar cell devices were fabricated as part of nanotechnology application. The knowledge of how these materials behave at nanoscale will help us understand the underlying physics involved. We chose to work with materials in the nanometre regime because they exhibit multiple exciton generation (MEG). This MEG is very crucial for improving efficiency of solar cell devices because more than one photo-induced electron-hole pairs are formed. The use of the semiconductor materials in the form of layered structures will allow to cover greater portion of the solar spectrum leading to enhanced efficiency yield.

1.3 Problem Statement

There are many energy challenges faced globally and researchers are working relentlessly to come up with solutions. One of the priorities is to reduce the amount of material needed for device fabrication and that will minimize the market price of solar cells. Within different generations of solar cells, there are technical problems associated with converting the solar energy into electricity. The biggest challenge lies in the spectral distribution of radiation from the sun, changes in the latitude, seasons (winter, summer etc.) and weather impacts (rainy and cloudy days). The spectral mismatch among the employed materials causes another issue for energy conversion and solar energy spectrum which leads to absorbed light being not all utilized for generation of electrical power. With the use of latest technologies of solar cells, researchers developed good absorber materials that assists in enhancing the PCE.

1.3.1 Efficiency of solar cells

The costs of energy produced by photovoltaic (PV) devices can be reduced by improving the conversion efficiency as well as coming up with new methods that can lower production costs. Other major challenges that need to be addressed include stability of the PV devices and up-scaling. Studies have shown that, the PCE in solar cells is limited by fundamental factors such as imperfect absorption of the solar spectrum, recombination of the photo-generated charge carriers, shading losses, and series resistance losses [6, 7]. Most of the graphene-based organic solar cells have low efficiency due to high sheet resistance and low hydrophilicity of the spin coated graphene thin films. Thus, we have improved the deposition process and minimized impurities and recombination centers to ensure enhanced exciton generation and dissociation at the interface of our layered nanostructures.

1.3.2 Parameters that influence the efficiency of solar cells

One of the factors limiting the efficiency of solar cells is non-uniform grain size of crystals. At ambient air conditions, oxygen and water have been found to degrade the performance of most organic solar cells [8]. To reduce the aforementioned issues, it is very important to grow uniform, equally spaced and evenly shaped nano-crystalline materials. Such materials will create a nanoscale heterojunction, then photo-generated carriers travel short distances hence reducing the recombination of electrons.

1.3.3 Transparency of the top electrode

The low efficiency of SCs is caused by low transparency of top conductive electrode in photovoltaic devices. The top electrode should be highly transparent (transparency > 80%) to maximize sunlight transmission to the active area [9]. Thus, it is vital to develop transparent conducting electrode (TCE) with high transmittance and low resistance.

1.3.4 Use of Indium-tin oxide (ITO) doped with graphene

The acidity of poly (styrene sulfonic acid) (PSS) etches the ITO layer, and indium enters the organic active layer and degrades the device performance [10]. Furthermore, the rareness of indium in nature, brittleness and rising costs are some of the major challenges in this field of study. Doping ITO with graphene can help to fabricate the electrodes that are highly transparent and conductive to generate solar energy.

1.3.5 Polymer doped with graphene

Polymer can be used as an active layer to donate and accept electrons in order to improve the efficiency of solar cells. The inherent problem of organic solar cells lies in the donor-acceptor material [11]. Due to ineffective electron/hole transport caused by lengthy aliphatic ligands and unsatisfactory continuous interpenetrating networks, the usage of polymers is restricted. The in-situ synthesis of poly (3-hexylthiophene) (P3HT), where P3HT is used as a ligand can be followed to address this problem [12].

1.3.6 Light harvesting of the donor material

The power conversion efficiency (PCE) of photovoltaic devices generated using one dimensional (1-D) nanostructures such as nano-rods is very low due to limited light harvesting process caused by much small surface area and little light scattering [13]. A promising solution to improve charge collection efficiency is the introduction of highly conductive carbon materials, such as graphene into semiconductor nanomaterials [14]. Nanoparticles with large surface area that will ensure a large adsorption of most of the dye molecules are required for efficient light harvesting process to be achieved.

1.3.7 Efficiency of light conversion (charge transfer)

The trap levels on the surface of semiconducting nanomaterials slow down the electron transport and this hinders the enhancement of conversion efficiency [15]. Excellent passivation of the surface is crucial in order to achieve higher conversion efficiency of SCs. Thus, the creation of superior photo-anode materials is a successful strategy for improving SC performance.

1.3.8 Charge transport

The quantum dot sensitized solar cells (QDSSCs) have also experienced low efficiency when using un-doped ZnO. The poor performance is caused by the agglomeration of electrons in ZnO layer (photo-anode) induced by charge recombination at the semiconductor-electrolyte interface [16]. It is very crucial to facilitate charge extraction and prevent charge recombination at the interface between layered nanostructures and the anode/cathode electrodes to improve J_{sc}, V_{oc} and the PCE of the solar cells [17].

1.4 Aim and Objectives of the Research

The main aim for this research project is to employ an effective method to grow layered nanostructures, fabricate hybrid solar cell devices and carry out their characterization.

The specific objectives of this study are summarized as follows:

i. To prepare various nanomaterials to be used for growing layered nanostructures for application in organic solar cells.
ii. To characterize layered nanostructures for better understanding of their structure, composition, morphological, optical and electrical properties.
iii. To study the effect of Ho incorporation into GO nanoparticles grown on P3HT donor material.
iv. To investigate the best method of depositing P3HT for organic solar cells.
v. To evaluate the interactions between P3HT and GO using spectroscopic techniques.
vi. To fabricate organic solar cell devices and test their efficiency.

1.5 Thesis Outline

The research work conducted to compile this thesis consists of nine (9) chapters.

Chapter 1: The first chapter focused on the factors that brought enthusiasm to conduct the research, issues to be addressed and the main aim and how the rest of the thesis is constructed.

Chapter 2: This chapter reviews the existing literature on energy challenges, different types of photovoltaics the concept of photovoltaics (PV) and its current/future applications.

Chapter 3: Describes the methods of growing layered nanostructures and furnishes full details of the characterization techniques that were used to probe information and their way of operation.

Chapter 4: Investigates the charge and energy transfer between P3HT/GO nanocomposites. Published: *Adv. Mater. Lett.* **8** (2017) 246-250

Chapter 5: Discusses the growth and characterization of HoGO/P3HT.
Published: *J. Physics: Conf. Series* **984** (2018) 012003

Chapter 6: Compares various deposition methods for the growth of layered nanostructures and their characterization.

Chapter 7: Evaluates the interactions in GO/P3HT layered nanostructures grown using spin coating technique.

Chapter 8: Presents a simple approach on growth, characterization and fabrication of GO/ZnO/P3HT layered nanostructures.
Submitted: *Physica B* (2023)

Chapter 9: Summary, future work, publications and conferences.

1.6 References

[1] NASA image "Satellite photo of earth at night, https://geology.com/articles/satellite-photo-earth-at-night.shtml Accessed [17 March 2019].

[2] United Nations General Assembly, *resolution 2 session 55* United Nations Millennium Development Goals.

[3] T.C. Chineke and F.M. Ezike, *Energy Policy.* 38 (2010) 678-684.

[4] International Energy Agency, *World Energy Outlook 2010*; http://large.stanford.edu/courses/2010/ph240/riley2/docs/EIA-0484-2010.pdf Accessed [March 2019].

[5] N. Agarwal, A. Kumar and Varun, *Energy for Sustainable Development*. (2013).

[6] W. Shockley and H.J. Queisser, *J. Appl. Phys.* **32** (1961) 510-519.

[7] T. Tiedje, E. Yablonovitch, G.D. Cody, and B.G. Brooks, *IEEE Trans. Electron Devices*, **31** (1984) 711-716.

[8] W.J. Potscavage, S. Yoo, B. Domercq and B. Kippelen, *Appl. Phys. Lett.* **90** (2007) 1-4.

[9] H. Kim, J.S. Horwitz, G.P. Kushto, S.B. Qadri, Z.H. Kafafi, and D.B. Chrisey, *Appl. Phys. Lett.* **78** (2001) 1050-1052.

[10] J.H. Kim, T.W. Kang, S.I. Na, Y.Z. Yoo, and T.Y. Seong, *Curr. Appl. Phys.***15** (2015) 829-832.

[11] H.A. Alturaif, Z.A. Alothman, J.G. Shapter, and S.M. Wabaidur, *Molecules* **19** (2014) 17329-17344.

[12] A.S.U, C.R. Jegathese, S. Kings, and M.T. Jaffar, **11** (2016) 1258-1261.

[13] S.H. Lee, J. Kwon, D.Y. Kim, K. Song, S.H. Oh, J. Cho, E.F. Schubert, J.H. Park, and J.K. Kim, *Sol. Energy Mater. Sol. Cells* **132** (2015) 47-55.

[14] D. Chen, H. Zhang, Y. Liu, and J. Li, *Energy Environ. Sci.* **6** (2013) 1362.

[15] H.E. Wang, L.X. Zheng, C.P. Liu, Y.K. Liu, C.Y. Luan, H. Cheng, Y.Y. Li, L. Martinu, J.A. Zapien, and I. Bello, *J. Phys. Chem. C*, **115** (2011) 10419-10425.

[16] I. Robel, V. Subramanian, M. Kuno, and P.V. Kamat, *J. Am. Chem. Soc.* **128** (2006) 2385-2393.

[17] Y. Zhong, H. Zhang, D. Pan, L. Wang, and X. Zhong, *J. Energy Chem.* **24** (2015) 722.

"Do your duty and a little more and the future will take care of itself."

Andrew Carnegie

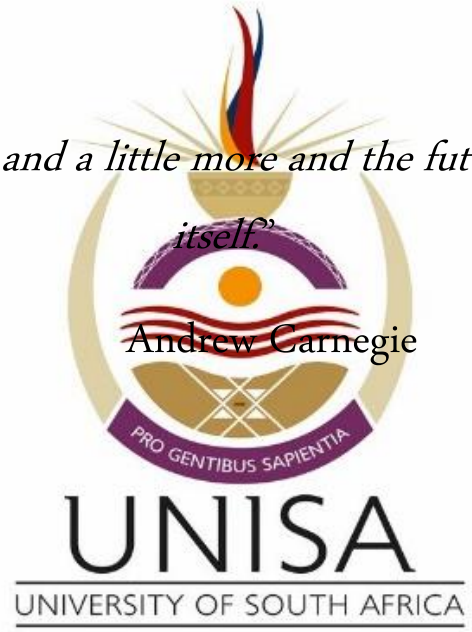

Chapter 2: Theoretical Background of Photovoltaic Cells, Graphene Fundamentals, Properties and Applications, Graphene in Organic and Inorganic Solar Cells

2.1 Introduction

Worldwide, the focus on clean energy sources has raised efforts to explore solar cells as one of the viable options. Renewable energy (RE) is considered as energy that comes from resources which are naturally restored, such as sunlight, wind and rain [1]. One of the potential renewable energy sources that can replace traditional fossil fuels is green energy generated from photovoltaic devices. The common sources of energy such as oil, coal and natural gas are getting depleted, due to an increase in energy demand [2]. Furthermore, there are environmental issues due to fossil fuels such as air and water pollution. Thus, shifting to RE can minimize some of the factors that are responsible for climate change, and ultimately ensuring cost effective energy supply [1]. As a result, it is in the mandate of International Energy Agency to make photovoltaic cells the leading source of electricity in the world by the year 2050.

Among others, organic [3], hybrid organic-inorganic [4], all-inorganic [5] and dye-sensitized [6] solar cells have been developed to serve as integrated energy sources. From the discovery of solar cells to date, Czochralski grown monocrystalline silicon was used as a main component of solar cells [7]. In order to have more charges collected efficacy of solar cells, one approach is to make use of electrically conductive carbon materials, such as fullerenes [8], carbon nanotubes (CNTs) [9] and graphene [10].

Recently, extensive research has been conducted on carbon which is considered the most fascinating element on the periodic table and abundant on earth. Carbon has unique electronic structure that allows hybridization to build up various networks like sp, sp^2 and sp^3 that leads to its well-known stable allotropes. There are mainly four carbon-based nanomaterials namely graphene, graphite, fullerenes (C_{60}) and carbon nanotubes respectively, that were discovered from allotropes of carbon. Among these allotropes, graphene is the primary structure because it can be arranged layer on top of another to form graphite, enclosed to form fullerenes and rolled up to form carbon nanotubes. Hence, there is much focus on graphene in fields such as Physics, Chemistry and Materials Science. Of the above fields, graphene has potential applications in Nanoscience and Nanotechnology. The word graphene is derived from the Greek word “graphein” and it means to write which is one of the first uses

of this material. Theoretically graphene was studied by P.R. Wallace in 1947 for calculations in solid state physics [11]. Graphene was effectively discovered experimentally by two scientists Andre K. Geim and Konstantin S. Novoselov in 2004 using adhesive tape to peel apart shavings of graphite [12]. In 2010 they received the Nobel Prize for an important discovery that helped in the upbringing of a new science in condensed matter physics. In their success with the experiments they managed to produce, isolate, identify and characterize graphene [13].

Graphene, in particular, is a robust and flexible two-dimensional (2D) membrane of carbon atoms arranged in a honeycomb lattice. These novel one-atom thick sheets possess unique crystalline structure and dimensionality that leads to new mechanical (Young's modulus 1.0 TPa), chemical, thermal, optical (transmittance ~ 98%) and electrical (such as low resistivity, high mobility, and zero band gap) properties due to its sp^2 hybridized carbons [14, 15]. It is gaining much attention as a result of its excellent conducting and semiconducting properties. The unique structure and various properties of graphene offer a great opportunity to meet the challenges of energy conversion [16]. Some results suggest that graphene is a semi-metal with near-zero band gap energy with a slight convergence within valence and conduction states [17]. Furthermore, graphene stands out because it has outstanding electron mobility (250,000 cm^2/Vs), high transparency and theoretically high specific surface area (2630 m^2/g) [18]. Graphene has been one of the top nanostructured materials due to its extensive applications in various industries. It is more functional and effective in devices such as sensors, solar cells, super capacitors and batteries [19].

In this study, we start by investigating the main factors that limit the efficiency of solar cells and find ways to improve using graphene derivatives. Our focus is on growth of layered nanostructures using GO, ZnO, Ho and P3HT and investigating how they will affect the output efficiency of photovoltaic cells. The main challenge is to hybridize the 2-D carbon nanostructure with metal oxide to form nanomaterials with potential applications in PV devices. In this study ZnO was used to facilitate the electron transport within structure of layered solar cells. ZnO is in the category of metal oxides which gained attention as transport layers which are easily processed in solution and have good stability [20, 21]. Our focus is on employing graphene derivative (GO) and utilize it as an acceptor material for the betterment of photovoltaic device efficiency.

2.2 Materials for Solar Cells, the use of Graphene and its Fundamentals

There is an ongoing research on preparation of nanomaterials and their use in fabrication of stable solar cells (SCs) that can improve the PCE in order to comply with the commercial standards. In view of this, from the past few decades, multiple researchers gave devotion to the potential applications of metal oxide semiconductor materials to solar energy conversion. In solar cells, semiconductors contain a crucial component known as photo-anode which acts as a substrate for dye adsorption and a transport pathway for the electrons produced [22, 23]. To attain an enhanced light harvesting efficiency, semiconductor photo-anode should be in the nanometer regime which gives rise to greater surface area for dye adsorption and effective electron transport pathway for electron harvesting [6]. Amongst the wide range of semiconductors that were studied, significant effort has been made on TiO_2 [24]. It has been employed mainly as the photo-electrode material in dye-sensitized solar cells (DSSCs). Since the 1991 discovery of dye-sensitized solar cells, TiO_2 nanostructures have received a tremendous deal of attention [25].

ZnO is also used in SCs as an n-type window material [26]. It is well known that the morphology of ZnO can be tailored by varying experimental parameters to suit its applications in DSSCs. In most cases, the PCE of ZnO solar cells is significantly lower than that of TiO_2 solar cells [27]. ZnO is preferred over TiO_2 because it is easy to prepare, control its structure and morphology, furthermore it possesses higher electron mobility and charge transport [28]. The utilization of ZnO in DSSCs requires its deposition as a porous film with high surface area in microns for enhanced dye molecules adsorption [29].

Lot of theories about carbon monolayer came to physical realization in 2004, when Andre Geim and Konstantin Novoselov including their fellow researchers at Manchester University showed that carbon monolayers exist as a stable form of carbon called graphene [12]. Structurally graphene is perceived as a sheet of sp^2 bonded carbon atoms densely arranged in a honeycomb crystal lattice. It is considered superstar in the world of nanotechnology due to its exceptional features such as thinnest material, transparency (3,000,000 sheets equal to 1mm), stiffest, strongest (Young's modulus >0.5-1 TPa, tensile strength ~130 Gpa) and largest surface-to-weight ratio (~2,700 m^2 /gram) [30]. Fascination to this material attracted scientists to prepare it for exploration of its remarkable properties and potential applications. A number of specific methods have been developed for the synthesis of graphene, some of which are commonly used. Since the discovery of graphene, various technologies such as

electron beam (EB) irradiation [31], chemical vapor deposition (CVD) [32], microwave method [33], electrospray deposition [6], hummers method [34], doctor blade method [35], mechanical exfoliation [13], epitaxial growth [36], arc discharge method [37] and chemical methods [38] have been used to prepare graphene sheets of various sizes. These methods are classified into two categories; chemical and physical process employed to obtain the single layer graphene (SLG). The aforementioned methods have capabilities and some drawbacks. Most of the methods are complex, they consume time and energy, and some require accurate control of temperature, atmosphere and reagents. Furthermore, the necessity for ultrahigh vacuum (UHV) conditions complicates other methods and the rising costs of single crystal substrates limit them for large scale applications [39].

The most common and the easiest method of producing graphene of the highest quality is mechanical exfoliation [40]. This is the first technique known as the Scotch tape method that has been used to originally exfoliate flakes of graphene from natural graphite [41]. But, the quantity of graphene acquired is small hence the method is best suited for research. Thus, one of the alternative methods to produce graphene in bulk is CVD. Between 2008 and 2009 CVD emerged and it was first reported as the vital route for the preparation and production of graphene [42]. The CVD method is promising because it is flexible and can produce large area sheets. CVD is also capable of producing chemically tuned 2D nanomaterials, such as substitution doped graphene [43] and C-graphene [44], by simply changing gas sources. Moreover, CVD enables doping of graphene, e.g. with HNO_3 in order to increase the carrier concentration, thereby shifting the Fermi level and reducing the resistance [45].

Several researchers have been trying to prepare graphene at ambient conditions such as pressure for a long time [38, 46]. Only recently they have discovered that large area single layer graphene (SLG) and few layer graphene (FLG) can be synthesized using CVD, yet the growth mechanism and several aspects of the properties of graphene prepared by CVD still remain unclear. It is important to use certain amount of hydrogen when preparing FLG graphene using CVD to keep stability between the production of reactive hydro-carbonaceous radicals and the etching of graphite layer during the CVD process [47]. Experimentally, it has been proven that if the methane to hydrogen ratio is too low, the etching reaction will be much faster than the establishment of graphene layers [48]. After successful synthesis of graphene, there have been several efforts geared towards understanding its properties. Various techniques that include XRD, TEM, SEM, UV-Vis, and PL have been used to explore the properties. It is highly important that the following techniques; SEM, TEM and

electron beam lithography are used to study the properties of graphene and graphene-device fabrication [49].

In 1839 Becquerel *et al.* [50] discovered the flow of electrical current wherein silver coated platinum electrodes were exposed to sunlight. It is evident from Łukasiak *et al.* [51] that photoconductivity in solids was discovered in 1873 by Smith *et al.* using selenium. Aazou *et al.* [52] reported that solar cell fabricated using gold coated selenium was built by Fritts *et al.* in 1883 who achieved the PCE of 1%. Since the PCE is low and the material used is very expensive, solar cells manufactured were not used abundantly to generate power. The huge stunt was made in 1954 at Bell Labs when the first silicon solar cell exhibiting a PCE of 6% was developed [53]. Thus far, silicon based solar cells are the most dominant with PCE higher than 25% for monocrystalline silicon [54]. Considerable efforts have been made since the discovery of DSSCs in 1991 owing to their high-energy conversion efficiency in PV devices [55].

Commonly, platinum (Pt) is found to be the abundant material to produce cathode electrodes for solar cells for it possess astonishing catalytic activity in reduction of triiodide ion (I_3^-) in addition to high electrical conductivity [56]. However, Pt is barely found in nature as a result it is highly expensive. Furthermore, Pt electrodes reflects incident light beam, leading to reduced efficiency under rear excitation, because it's a shiny metal. Currently, indium tin oxide (ITO) is the most widely used transparent electrode in solar cells, because of its low resistance and excellent optical transmission properties. But the challenge is it suffers from brittleness and high production costs. Besides, the diffusion of indium (I) will result into degradation of device performance, thus ITO cannot be effective for flexible applications. One more challenge for using ITO electrodes is because of limited supply of indium in nature. It is necessary to replace Pt and ITO with cheap and abundant materials with acceptable catalytic activity. On the other site, polymer-based materials have been used as additives in DSSCs, such as electrolytes, hole conductor and plastic substrates [57, 58]. The advantages of using polymeric materials include the construction of flexible solar cells, which are not only convenient for transportation but effective in challenging environmental conditions.

To address some of these challenges, various carbon-based materials were highly investigated to serve as alternative for ITO and Pt counter electrodes (CEs). One dimensional (1D) carbon nanotubes (CNTs) have the capability of increasing charge transport and thus improve the

performance of DSSCs. As a result of the creation of 1D CNT bridges between semiconductor nanoparticles like TiO_2 photo-anodes, CNTs in DSSCs provide an electron transport superhighway [59, 60]. The 1D bridge has a drawback, which is the poor point contact at the interface of TiO_2 and CNTs, which causes low charge transport and reduction in efficiency of the DSSCs [61]. To overcome this challenge, the incorporation of highly conductive graphene nanoparticles with TiO_2 matrix can help to enhance the transportation of charges. In the past the electrodes were made up of porous carbon, but recently the researchers began to investigate the possibility of using graphene as electrodes [62]. Among carbon allotropes, graphene nanostructures have been explored for several roles in solar cells because it's inexpensive and it possesses outstanding properties. It is used as a transparent electrode in DSSCs [63]. This is mainly due to graphene-based nanomaterial's that have shown intriguing characteristics, including a large surface area, excellent conductivity and very good capacitance at low cost of production [62]. Graphene with large surface area is in high demand, because it significantly reduces high inter-sheets contact resistance in comparison with small surface area graphene [64]. Graphene has the merit of performance stability. Jiang *et al.* [65] suggested that the 2D graphene bridges could offer DSSCs a solution to have lower recombination and faster electron transport.

Recently, significant effort has been made to incorporate heteroatoms, such as nitrogen, boron etc. into graphene oxide [66] and graphene nano-platelets [67] to improve their electro-catalytic activity. Significantly, chemical doping helps to reduce the sheet resistance of graphene. It is suggested that the concentration of the dopants should be minimal as large amounts tends to create carrier recombination centres or light-harvesting competition with dye molecules which greatly minimizes the performance of photo-electrode [68, 69]. Subsequently, other researchers prepared the Schottky junction solar cells by contacting a metal with a moderate doped semiconductor because it has the ability to convert solar to electric energy [70]. However, this type of solar cell has some shortcomings whereby most of the photon energy will be absorbed by the metal layer, resulting in a low rate of energy conversion. Furthermore, chemical doping with semiconductors such as GaAs has been explored and effectively it improved the solar cell efficiency [71]. For highly efficient solar cells, metal oxide inorganic semiconductors like NiO, WO_3, and V_2O_5 are used as hole extraction layers (HEL) to improve charge transport by lowering the energy barrier between the electrodes and the active layer [72-74]. In some of the research conducted, investigations have been made on the development of the graphene/silicon (G/Si) junction for solar cells.

The first graphene-doped hetero-junction solar cell was fabricated by Li *et al.* [75] in 2010 and they obtained PCE of 1.65%. Since then, efforts to alter the work function and lower the sheet resistance of graphene in order to increase the performance of graphene-based Si solar cells have continued [76, 77].

Solar cells made of graphene might have a theoretical efficiency limit of more than 60%, hence it is considered as candidate for third generation solar cells. Yong *et al.* [78] were the first to predict the efficiency of graphene-based OPVs, showing the possibility for single-cell efficiencies of more than 12% and 24% in a stacked structure. Their research findings propose that the tunable band gap and band-position features of graphene, including its superior thermal stability and mechanical integrity, making it a reliable material for building the next-generation of low-cost, high-efficiency, thermally stable, environmentally friendly, and lightweight flexible solar-energy-conversion devices. Graphene is believed to be a strong UV stabilizer; therefore, TiO_2 is added to it in order to absorb as much sunlight as possible and make it simple for dye molecules to give the electrons they have been able to capture to the surface of the semiconductor film [79]. Zhu and co-workers described the insertion of graphene into TiO_2 nanoparticle photo-anodes using one-step hydrothermal approach [80]. They characterized their material using techniques such as XRD, SEM, transmission electron microscopy TEM, Raman spectrometers, photocurrent density - voltage (J-V), EIS, IMVS, and IMPS. Wang and his colleagues created the P3HT/PCBM-graphene PV system, which uses graphene as an electron acceptor and P3HT as photoexcited electron donors [81]. They witnessed the increment in performance following the extension of the excitons dissociation area and to foster electron transfer through the graphene. A lot of work has been done on graphene, but its role and the mechanisms in photo-anode materials remain unclear. Hence, there is an ongoing research to finetune it for the improvement of PV devices.

Hybrid nanostructured heterojunction solar cells have been found to be promising PV technology for renewable energy harvesting because they are cost efficient [82]. A significant cost reduction is possible with these thin film solar cells because they require small amount of materials, cheap and few processing steps and they can be manufactured in bulk. Utilizing organized ZnO nanostructures as the acceptor substance and reduced graphene oxide (RGO) as the transparent conducting electrode to create RGO/ZnO/P3HT/PEDOT:PSS/Au, Yang *et al.* [83] created heterojunction solar cells. Due to the wide ZnO-nanotube interfacial area for charge separation and the high electrode conductance of RGO for current collection, their system demonstrated the highest solar energy harvesting efficiency where they achieved

0.46% PCE. Huang *et al.* [84] have reported the use of low-cost ambient pressure CVD graphene sheets as front electrodes for CdTe solar cells. They created a device using the following architecture glass/graphene/ZnO/CdS/CdTe/ (graphite paste) structure. This demonstrated a PV efficiency of 4.17 %, offering encouraging proof that the transparent conducting graphene sheets may be employed as a brand-new, reasonably priced front electrode material for thin film PV devices. The same research team used Cu-nanowire-doped graphene (Cu NWs/graphene) as the back contact in thin film CdTe solar cells [85]. Cu NWs/graphene in their study possessed a high electrical conductivity of 16.7 S cm^{-1} and a carrier mobility of 16.2 $cm^2V^{-1}s^{-1}$ with PCE of up to 12.1%. Graphene has been used as electron acceptor to fabricate PV devices with a bulk heterojunction (BHJ) architecture, the PCE of 14% was obtained using simulated 100 mW cm^{-2} [86]. Recently, the achieved PCE is much greater than 15% using hybrid organic-inorganic PV technology [87]. Moon *et al.* [88] reported the enhanced PV performance with graphene hybrid solar cells and they achieved ~10.3 % PCE. The recently recorded efficiencies may satisfy the requirements for most applications, yet there's a room for further improvement towards theoretical maximum of ~ 60% [78].

2.3 Solar Radiation Spectrum

The solar radiation spectrum is mainly provided as AM1.5G, where G represents the global sun which incorporates direct and diffuse light with air mass (AM) for air mass as shown in Figure 2.1. The number 1.5 symbolizes ratio of the solar irradiation path length (L_S) in the atmosphere over that corresponding to a vertical position of the sun (thickness of the atmosphere, L_A) for an incident angle θ relative to the normal of the earth's surface and an irradiation flux of 1000 $W\ m^{-2}$. It is crucial to understand that only a small portion of solar radiation reaches the surface of the earth while the other portion is lost through reflection and absorption by the earth. The estimation revealed that the accessible solar energy on the earth's surface is about a 10 000 times the world's energy consumption [89].

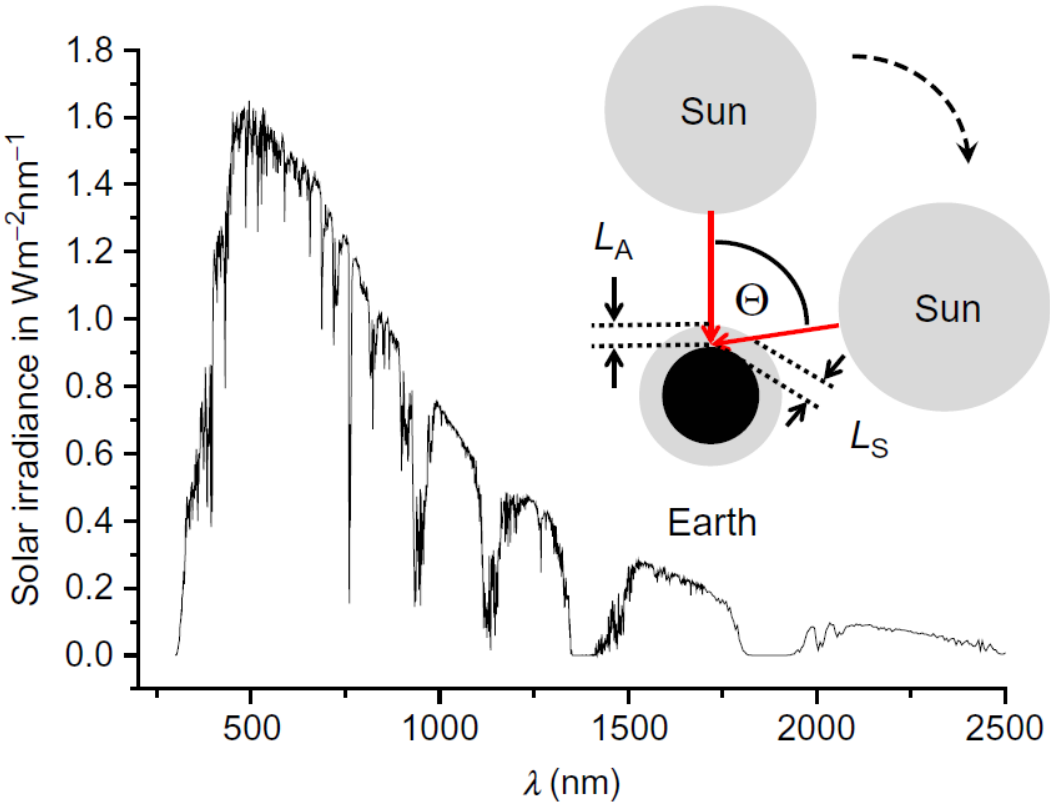

Figure 2. 1 Air-Mass 1.5G (AM 1.5G) solar irradiance spectrum and sketch showing definitions for parameters used [90].

2.4 Generations of Solar Cells

For many years, couple of methods have been probed for the conversion of light into electrical energy, and semiconductors appeared to be the most successful in attaining the goal. With the developments in technology, photovoltaic (PV) cells continued to give birth to various generations of photovoltaics. They are classified into four generations based on time of discovery and kinds of materials used to fabricate them. Each technology helped to build the next generation utilizing the physics factors like the power-voltage and current voltage relationships. Among the types of PV's, the common factor are the efficiency, durability, economic feasibility etc. which mainly depends on the capabilities of the type of SCs. Not all of them have been commercialised because others are not economically viable. Crystalline silicon, thin film silicon, amorphous silicon, Cu(InGa)Se_2, cadmium tellurite, dye-sensitized, organic and multi-junction solar cells are the most common types among those available in the market [91]. From afore mentioned, the silicon based SCs are the most dominant with about 93% supply in the market and others shares the remaining 7%. The silicon p-n junction SCs fall within the first generation (1 G) which achieved 6% of sunlight conversion from the

beginning while estimated to reach maximum of 22% [92]. This 1 G is subdivided into three categories: (i) wafers which uses crystalline/monocrystalline and multi-crystalline/polycrystalline Si (c-si and m-Si), (ii) thin-films based on amorphous Si, and (iii) advanced thin films doped with different elements to tune their bandgap also called hybrid panels. The second generation (2 G) of SCs is the thin film technology which is made up of multiple thin layers of PV materials, electrodes and wavelength converting materials. The introduction of 2 G came to cover the issue of high cost and the amount of material used in silicon SCs. In this generation several semiconductor materials are combined to form a multi-junction device with the aid of covering wide range of the solar spectrum resulting in higher absorption yield. Greater achievement was seen in 1986 when Tang came up with heterojunction wherein two materials were evaporated on top of each other in the so-called bilayer architecture [93]. They are mainly applied on textile products and flexible devices which can be folded with an advantage of being grown on large surface areas up to $6\,m^2$. However, the conversion efficiency is lower compared to that of 1 G of SCs. But the parameter that worked fairly well for 2 G was the $/W cost per watt delivery.

More developments in the PV industry brought the third generation (3 G) of SCs with the aim of obtaining higher performance than that of 1 G and 2 G at lower costs. Concurrently, the 3 G was developed with nano-crystalline films of active quantum dot-based PVs, tandem or stacked inorganic multilayers made of III-V materials like GaAs/Ge/GaInP2, or innovative device concepts like hot carrier cells [94]. This generation focused on integrating nanostructured materials such as quantum dots, nanowires, nanowells etc. to improve the efficiency through quantum confinement [95, 96]. The 3 G dealt with materials in nanoscale and upscaling to the macroscopic range with full attention devoted to charge and energy transfer processes. Furthermore, it investigated ways of optimizing charge collection and enhancing the energy capturing from solar spectrum. Different materials that exhibit photovoltaic properties were investigated within 3 G and organic materials became the hot topic due to their potential low cost and high optical absorption in this technology. The other candidate that grew tremendously in this technology is the dye sensitised solar cells (DSSCs). With the success of this technology more work need to be done on the improvement of device performance so they can surpass the other technologies in terms of cost per watt.

As technology matured, the fourth generation (4 G) of SCs emerged as a hybrid technology which make use of composite materials. This generation was developed with the intention of

strengthening the optoelectronic characteristics of affordable thin film PVs by combining organic and inorganic materials creating inorganics-in-organics architecture. It is referred to as novel semiconductor devices which does not rely on traditional p-n junction to separate photo-generated charges. Many different types of SCs are produced through this technology including flexible SCs that help to reduce manufacturing and installation cost. These technologies are already available in the international market and they came with new standards and testing schemes to keep the development ongoing [97]. It is more promising in obtaining competitive cost to efficiency ratios. To date, the most effective polymer solar cells (PSCs) have been based on the bulk heterojunction (BHJ) concept and the success in fabrication of BHJ was first done in 1995 by Halls and Yu [98, 99]. We have seen tremendous increase in solar energy harvesting and conversion into electricity through the use of 4 G offering better efficiency than other generations at affordable costs. The 4 G brought most successful types of SCs. To date the most efficient devices are perovskite SCs with the maximum PCE beyond 20 % obtained in few years as per National Renewable Energy Laboratory (NREL) report depicted in Figure 2.2. Perovskite SC is a highly competitive technology in terms of efficiency against its counterparts. It forms part of the latest developments in hybrid SCs that led to significant improvements in device performance. Moreover, it is enriched with rare earth metals which possess high charge carrier mobilities that promote efficient charge extraction.

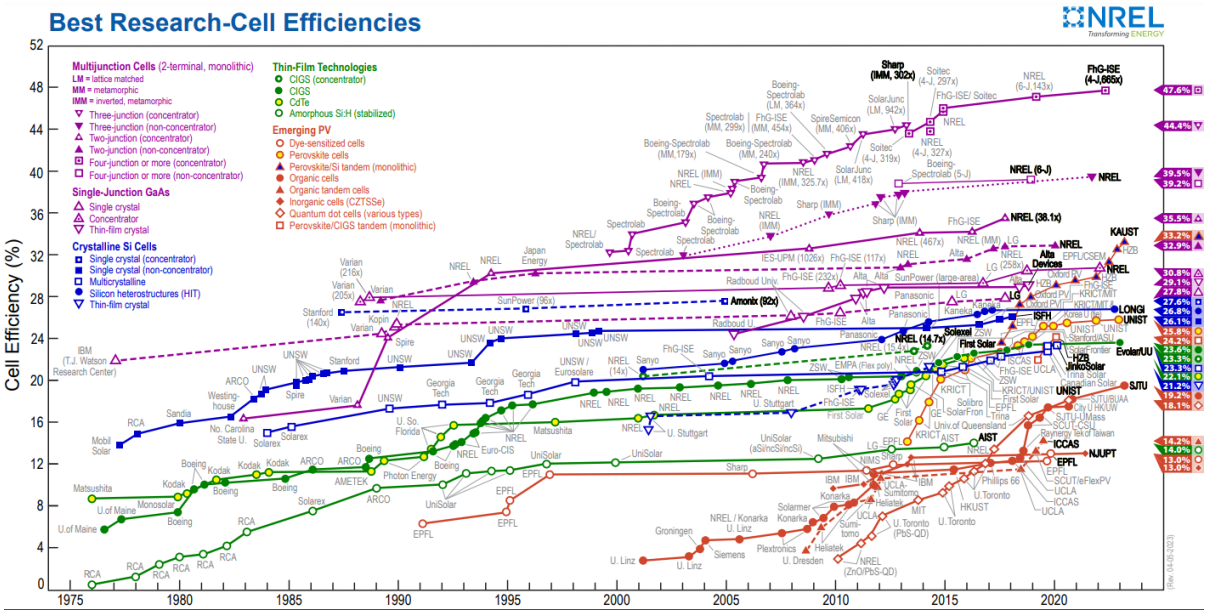

Figure 2. 2 NREL chart of the highest confirmed conversion efficiencies for various photovoltaic technologies, plotted from 1976 to present [100].

Moreover, the highly competitive cells in the emerging technology are the tandem SCs. They possess unique properties that include long carrier diffusion length, high absorption coefficient, high defect tolerance and ambipolar charge transportation [101]. Thus, they have shown the capability to surpass the efficiency limit of single junction SCs. Their added advantages such as process compatibility, narrow light absorption edge and tunable band gap put them in the glass of perovskite SCs with the state of the art silicon cells [102]. Moving forward with the idea of reducing costs while achieving high production, the organic materials have attracted wide range of researchers. The organic photovoltaics (OPV) are of high interest because of capabilities such as relying on abundant materials, being easily scalable and bearing the potential of very high speeds in roll-to-roll processing. However, significant progress has been made to date with regards to the efficiency and stability. The maximum power conversion efficiency obtained thus far is in the range 13-14% for single junction and bulk-heterojunction organic solar cells (BHJ OSC) [103, 104]. Moreover, their operational lifetime was estimated to a maximum of 10 years on the basis of exclusively intrinsic degradation process [105, 106]. Thus, improvements in these technologies approaches the idealised goals stepwise by using materials that can harness different regions of the solar spectrum and convert that energy into the operating region of specific solar cells.

2.5 Organic Photovoltaic Solar Cells, Renewable Source of Energy

Basically, a solar cell is a structured device wherein two layers of different semiconductor materials are grown a layer on top of another. Among various technologies of PVs aforementioned, PSCs well known as OPVs gained lot of attention due to their processing speed, processing simplicity and thermal budget. OPV stands out as promising technology in terms of providing solutions to challenges such high costs associated with PVs. In comparison to other SCs, they standout due to their material diversity, abundance and capability of large-scale fabrication of flexible devices. They are lightweight because they are not made of heavy glass sheets and metal frames, but their lifetime is limited in addition to their low efficiency. Moreover, they are environmentally friendly as they can be disposed at the molecular level. The semiconducting polymers and other organic materials are used to create different layers of the OSCs in the form of p-n junction diode.

Generally, the layered nanostructures for OPV-SC comprises a multi-layer structure where each layer in the stack is grown by varying different parameters to obtain an architecture

similar to the one presented in Figure 2.3. The device is grown on an ITO substrate which is a glass pre-coated with tin doped indium oxide (ITO) material. ITO is a transparent conductive bottom electrode that has a high work-function, mainly used for the collection of holes. It is the best performing transparent electrode material that brings along advantages such as high transparency over a huge spectrum of wavelengths, low electrical resistivity and high electrical conductivity. It possesses controllable thickness by adjusting layer-by-layer (LBL) deposition frequency. ITO is a good photo-anode that is mostly employed as a substrate for dye adsorption and transport path for the generated electrons [6]. The top electrode which is a non-transparent metallic material with a reflective surface to return light to the active component is evaporated on top of the active layer to form a complete SC device.

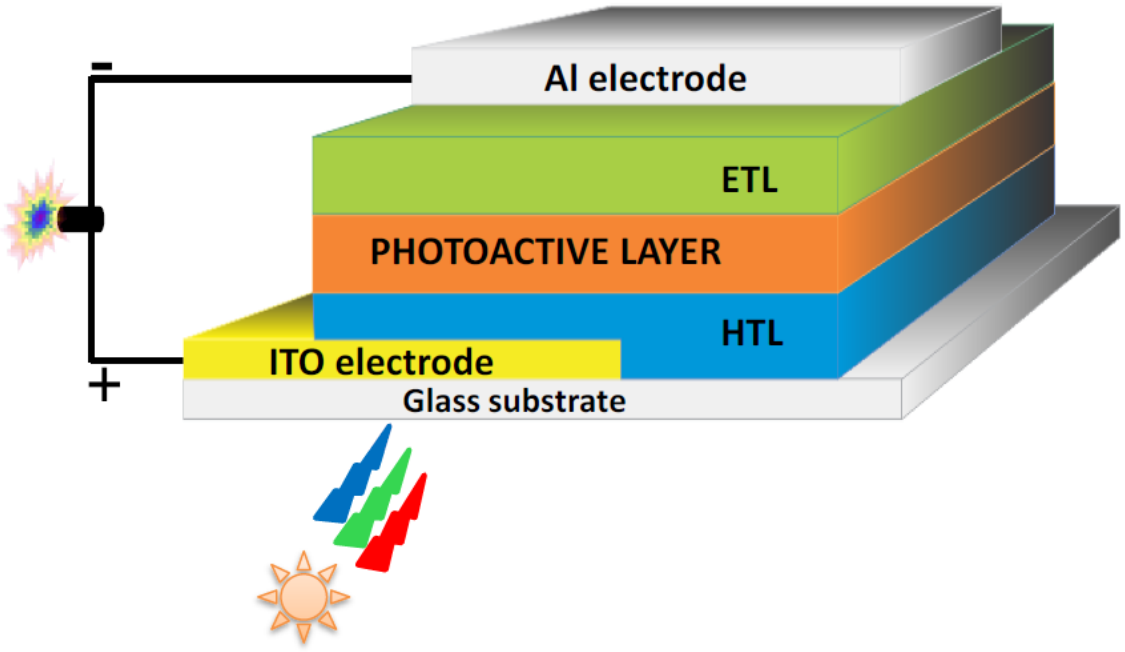

Figure 2. 3 Layered nanostructured solar cell layout [107].

The design of OPV-SC consists of photoactive layer made up of donor (D) material (polymer, here poly(3-hexylthiophene), P3HT) as well as the acceptor (A) material (carbon-based material, here graphene oxide (GO)) which are grown between a transparent conducting electrode (TCE) (eg. ITO) and a metal electrode (eg. Aluminium (Al)). For good device performance, these materials should have sufficient layer thickness for enhanced (photon absorption and exciton generation), wide D-A interface area that can be reached within the exciton diffusion limit. In between the D and A material, there's an intermediate layer usually made from inorganic semiconductors such as zinc oxide (ZnO) and titanium

dioxide (TiO_2) nanoparticles. The role of intermediate layer is to assist with mobility/transport of charges as they transition between photoactive layer and electrodes with mismatched energy levels and they can prevent charge recombination [105]. Additionally, it establishes a connection with the absorber layer while allowing the junction zone and absorber layer to receive the most intense light possible [108].

2.6 Generation of Electrical Current (Mechanism)

The technique used upon converting sunlight directly into electrical power by means of photovoltaic (PV) materials has been widely used in spacecraft industries and it is gaining more attention in the energy industry. There are several main processes taken in the operation of solar cells which include the absorption of light, charge separation and charge transport towards generating electricity using energy harnessed from the sun [109]. Detailed examination of these processes gives knowledge on behaviour of different materials and their role on generating electricity. Method of current creation is explained by quantum theory which outlines that light is built from tiny particles called photons. These photons have energy that relies on their respective frequencies of electromagnetic radiation (EMR). The energy obtained from visible part of EMR is sufficient to knock off electrons from the bound states to higher energy levels where they move with ease [110]. Basically, when radiation from the sun strikes the device, it penetrates through the transparent electrode and gets absorbed by the semiconductor donor and acceptor materials in photoactive layer. The electrons are transferred from donor material into the material having the lowest reduction potential known as acceptor material and the holes remains in the material with highest ionisation potential. This suggests that the absorbed light's energy is transferred to the semiconductor where it knocks the electrons loose and they start to travel freely creating holes. Thereafter, excitons are formed and they spread to the donor/acceptor contacts, where the excitons split into electrons on the lowest unoccupied molecular orbital (LUMO) level of the acceptor and holes on the highest occupied molecular orbital (HOMO) level on the donor. The built-in electric field propels the dissociated electrons and holes, which are then transferred to the negative and positive electrode, respectively, and they are gathered by the electrodes to carry out the photon-to-electron conversion [111]. All different types of PVs are designed and characterised in a way that resembles electrical circuits.

2.7 Efficiency Characteristics

When designing the photovoltaic modules, it is important to extract the parameters of the designed model. However, this is a challenging task because the structure is defined using the concept of solid-state physics. Obtaining the parameters of photovoltaic cells comes with various technologies, illumination, their size and the operating atmospheric conditions such as temperature [112]. The most crucial parameters of solar cells efficiency systems resembling the diode model are short-circuiting current I_{SC}, the ideality factor of diode n, the open-circuit voltage V_{OC}, the shunt resistance R_{sh} and the series resistance R_s [113, 114]. These parameters are used all together to determine the power conversion efficiency (PCE) given by equation (2.1) with FF depicting the fill factor [115]:

$$\eta_{in} = \frac{P_{out}}{P_{in}} = \frac{V_{OC} \times I_{SC} \times FF}{P_{in}} \qquad 2.1$$

Most of these important parameters can be extracted analytically but others are achieved from the experimental data. Usually, the Shockley diode equation also known as diode law is used to calculate the device features of the solar cells [116]. This numerical equation shows the implicit and non-linear I-V relationship of a device, then this equation is inquired to evaluate the effective extracted parameters. In practice, the solar cell external quantum efficiency (EQE) is determined by measuring the maximum cell power output P_m (W) and dividing it by the surface input powers P_S $(W.m^{-2})$ and the cell area A (m^2) shown in the equation (2.2):

$$EQE = \frac{P_m}{P_S \times A} \qquad 2.2$$

where P_m represents the load that maximizes the output voltage. Furthermore, parameters such as quantum efficiency η_Q which is governed by charge production and separation efficiency including the conduction efficiency together with afore mentioned parameters they are related by equation (2.3) which is similar to equation (2.1).

$$FF = \frac{P_m}{V_{OC} \times I_{SC}} = \frac{\eta_Q \times P_S \times A}{V_{OC} \times I_{SC}} \qquad 2.3$$

The current-voltage (I-V) relationship for the solar cell devices is presented by equation (2.4)

$$I = -I_{ph} + I_0[\exp(\frac{qV}{nkT}) - 1] \quad 2.4$$

where I_{ph} is the photocurrent I_0 is the reverse saturation current, V is the voltage applied or bias voltage and n is the diode factor.

The J-V measurements are useful in determining the sheet resistance using Van der Pauws's method. The carrier mobility (μ) measured in cm^2/Vs and carrier concentration (n) measured in cm^{-2} relates to the sheet resistance by the following expression in equation (2.5).

$$R_{sh} = \frac{1}{q} \quad (2.5)$$

2.8 References

[1] O. Ellabban, H. Abu-Rub, and F. Blaabjerg, *Renew. Sustain. Energy Rev.* **39** (2014) 748-764.

[2] D.B. Richardson and L.D.D. Harvey, *Energy* **93** (2015) 1447-1455.

[3] S. Yoo, B. Domercq, and B. Kippelen, *Appl. Phys. Lett.* **85** (2004) 5427-5429.

[4] W.U. Huynh, J.J. Dittmer, and A.P. Alivisatos, *Science* **295** (2002) 2425-2427.

[5] I. Gur and A.P. Alivisatos, **462** (2009).

[6] J. Liu, X. Fu, D.-P. Cao, L. Mao, J. Wang, D.-H. Mu, B.-X. Mi, B.-M. Zhao, and Z.-Q. Gao, *Org. Electron.* **23** (2015) 158-163.

[7] S.N. Rea, *J. Cryst. Growth*, **54** (1981) 267-274.

[8] T. Hasobe, S. Hattori, P.V. Kamat, Y. Urano, N. Umezawa, T. Nagano, and S. Fukuzumi, *Chem. Phys.* **319** (2005) 243-252.

[9] L. Yang and W.W.F. Leung, *Adv. Mater.* **25** (2013) 1792-1795.

[10] D. Chen, H. Zhang, Y. Liu, and J. Li, *Energy Environ. Sci.* **6** (2013) 1362.

[11] P.R. Wallace, *Phys. Rev.***71** (1947) 622-634.

[12] K.S. Novoselov, A.K. Geim, S.V. Morozov, D. Jiang, Y. Zhang, S.V. Dubonos, I.V Grigorieva, and A.A. Firsov, *Science* **306** (2004) 666-669.

[13] K.S. Novoselov, D. Jiang, F. Schedin, T.J. Booth, V.V Khotkevich, S.V. Morozov, and A.K. Geim, *Proc. Natl. Acad. Sci. U. S. A.* **102** (2005) 10451-10453.

[14] P. Hojati-Talemi and G.P. Simon, *Carbon N. Y.* **48** (2010) 3993-4000.

[15] H. Wang and Y.H. Hu, *Energy Environ. Sci.* **5** (2012) 8182.

[16] A. Taheri Najafabadi, *Renew. Sustain. Energy Rev.* **41** (2015) 1515-1545.

[17] P.A George, J. Strait, J. Dawlaty, S. Shivaraman, M. Chandrashekhar, F. Rana, and M.G. Spencer, *Nano Lett.* **8** (2008) 17-20.

[18] J.H. Byeon and Y.W. Kim, *ACS Appl. Mater. Interfaces* **5** (2013) 3959-3966.

[19] Y. Sun, Q. Wu, and G. Shi, *Energy Environ. Sci.* **44** (2011) 1113.

[20] W.C.H. Choy and D. Zhang, *Small*, **12** (2016) 416-431.

[21] G. Teran-Escobar, J. Pampel, J.M. Caicedo and M. Lira-Cantu, *Energy Environ. Sci.*, **6** (2013) 3088-3098.

[22] P. Sun, X. Zhang, X. Liu, L. Wang, C. Wang, J. Yang, and Y. Liu, *J. Mater. Chem.* **22** (2012) 6389.

[23] K. Park, Q. Zhang, D. Myers, and G. Cao, *ACS Appl. Mater. Interfaces*, **5** (2013) 1044-1052.

[24] B.S. Kwak, H. Lee, and M. Kang, *Chem. Eng. J.* **255** (2014) 613-622.

[25] D. Cheng, S. Huang, and W. Wang, *Chem. Phys.* **330** (2006) 423-430.

[26] T. Minami, T. Miyata, and Y. Nishi, *Sol. Energy*, **105** (2014) 206-217.

[27] A. Jana, P.P. Das, S.A. Agarkar, and P.S. Devi, *Sol. Energy*, **102** (2014) 143-151.

[28] S. Bi, F. Meng, Y. Zheng, X. Han, X. Tao, and J. Chen, *J. Power Sources* **272** (2014) 485-490.

[29] L. Dupuy, S. Haller, J. Rousset, F. Donsanti, J.F. Guillemoles, D. Lincot, and F. Decker, *Electrochem. commun.***12** (2010) 697-699.

[30] S.K. Misra, H. Pandey, and S.K. Misra, **2** (2013) 1-4.

[31] S. Kim, Y. Noh, S. Kwon, B. Kim, B. Lee, S. Yang, C. Jung, and S. Na, *J. Ind. Eng. Chem.* **26** (2015) 210-213.

[32] C. Mattevi and M. Chhowalla, (2011) 3324-3334.

[33] P. Hojati-talemi and G.P. Simon, *Carbon N. Y.* **48** (2010) 3993-4000.

[34] B.Y. Zhu, S. Murali, W. Cai, X. Li, J.W. Suk, J.R. Potts, and R.S. Ruoff, 1-19.

[35] P. Wang, F. He, J. Wang, H. Yu, and L. Zhao, *Appl. Surf. Sci.* (2015).

[36] C. Berger, Z. Song, T. Li, X. Li, A.Y. Ogbazghi, R. Feng, Z. Dai, A.N. Marchenkov, E.H. Conrad, P.N. First, and W.A de Heer, *J. Phys. Chem. B*, **108** (2004) 19912-19916.

[37] K.S. Subrahmanyam, L.S. Panchakarla, A. Govindaraj, and C.N.R. Rao, **113** (2009) 4257-4259.

[38] X. Shen, L. Jiang, Z. Ji, J. Wu, H. Zhou, and G. Zhu, *J. Colloid Interface Sci.* **354** (2011) 493-497.

[39] A. Reina, X. Jia, J. Ho, D. Nezich, H. Son, V. Bulovic, M.S. Dresselhaus, and K. Jing, *Nano Lett.* **9** (2009) 30-35.

[40] A.K. Geim, *Science* **324** (2009) 1530-1534.

[41] D.W. Chang, H.-J. Choi, A. Filer, and J.-B. Baek, *J. Mater. Chem. A* **31** (2014) 12136-12149.

[42] Y.I. Zhang, L. Zhang, and C. Zhou, *Acc. Chem. Res.* **46** (2013) 2329-2339.

[43] D. Wei, Y. Liu, Y. Wang, H. Zhang, L. Huang, and G. Yu, (2009).

[44] W. Cai, R.D. et al., Ruoff, *Science*, **321** (2008) 1815-1817.

[45] S. Bae, H. Kim, et al., *Nat. Nanotechnol.* **5** (2010) 574-578.

[46] K.S. Kim, Y. Zhao, H. Jang, S.Y. Lee, J.M. Kim, J.-H. Ahn, P. Kim, J.-Y. Choi, and B.H. Hong, *Nature*, **457** (2009) 706-710.

[47] H.J. Park, J. Meyer, S. Roth, and V. Skkalov, *Carbon N. Y.* **48** (2010) 1088-1094.

[48] A. Reina, S. Thiele, et al., *Nano Res.* **2** (2009) 509-516.

[49] Y.H. He, L. Wang, X.L. Chen, Z.F. Wu, W. Li, Y. Cai, and N. Wang, *Appl. Phys. Lett.* **99** (2011) 2009-2012.

[50] A.E. Becquerel, *Acad. des Sci.* **9** (1839) 561-567.

[51] L. Łukasiak and A. Jakubowski, *J. Telecommun. Inf. Technol.* **29** (2010) 3-9.

[52] S. Aazou, A. Ibral, et al., *J. Optoelectron. Adv. Mater.* **15** (2013) 395-404.

[53] D.M. Chapin, C.S. Fuller, and G.L. Pearson, *J. Appl. Phys.* **25** (1954) 676-677.

[54] M.A. Green, K. Emery, Y. Hishikawa, W. Warta, and E.D. Dunlop, *Prog. Photovoltaics Res. Appl.* **23** (2015) 1-9.

[55] B. O'Regan and M. Grätzel, *Nature*, **353** (1991) 737-740.

[56] Y. Hu, A. Yella, S. Guldin, M. Schreier, F. Stellacci, M. Grtzel, and M. Stefik, *Adv. Energy Mater.* **4** (2014).

[57] J. Xia, N. Masaki, M. Lira-Cantu, Y. Kim, K. Jiang, and S. Yanagida, *J. Am. Chem. Soc.* **130** (2008) 1258-1263.

[58] X. Yin, F. Wu, N. Fu, J. Han, D. Chen, P. Xu, M. He, and Y. Lin, *ACS Appl. Mater. Interfaces* **5** (2013) 8423-8429.

[59] L. Yang and W.W.F. Leung, *Adv. Mater.* **23** (2011) 4559-4562.

[60] A. Kongkanand, R.M. Domínguez, and P.V. Kamat, *Nano Letters* **7** (2007) 676-680.

[61] L.J. Brennan, M.T. Byrne, M. Bari, and Y.K. Gun'ko, *Advanced Energy Materials*, **1** (2011) 472-485.

[62] M.J. Allen, V.C. Tung, and R.B. Kaner, *Chem. Rev.* **110** (2010) 132-145.

[63] Q. Tai and X.-Z. Zhao, *J. Mater. Chem. A*, **2** (2014) 13207-13218.

[64] F. Ban and S. Majid, *J. Electrochem.* **7** (2012) 4345-4351.

[65] N. Yang, J. Zhai, D. Wang, Y. Chen, and L. Jiang, *ACS Nano*, (2010) 4887-894.

[66] H. Fang, C. Yu, T. Ma, and J. Qiu, *Chem. Commun. (Camb).* **50** (2014) 3328-3330.

[67] M.J. Ju, J.C. Kim, H.J. Choi, I.T. Choi, S.G. Kim, K. Lim, J. Ko, J.J. Lee, I.Y. Jeon, J.B. Baek, and H.K. Kim, *ACS Nano*, **7** (2013) 5243-5250.

[68] Y.Y. Dou, G.R. Li, J. Song, and X.P. Gao, *Phys. Chem. Chem. Phys.* **14** (2012) 1339-1342.

[69] F. Gong, H. Wang, and Z.-S. Wang, *Phys. Chem. Chem. Phys.* **13** (2011) 17676-1782.

[70] Y. Ye, L. Dai, P.C. Wu, C. Liu, T. Sun, R.M. Ma, and G.G. Qin, *Nanotechnology* **20** (2009) 375202.

[71] H. He, X. Yu, Y. Wu, X. Mu, H. Zhu, S. Yuan, and D. Yang, *Nano Energy* **16** (2015) 91-98.

[72] J. Jung, D.L. Kim, S.H. Oh, and H.J. Kim, *Sol. Energy Mater. Sol. Cells* **102** (2012)

103-108.

[73] S. Han, W.S. Shin, M. Seo, D. Gupta, S.J. Moon, and S. Yoo, *Org. Electron. physics, Mater. Appl.* **10** (2009) 791-797.

[74] K. Zilberberg, S. Trost, H. Schmidt, and T. Riedl, *Adv. Energy Mater.* **1** (2011) 377-381.

[75] X. Li, H. Zhu, K. Wang, A. Cao, J. Wei, C. Li, Y. Jia, Z. Li, X. Li, and D. Wu, *Adv. Mater.* **22** (2010) 2743-2748.

[76] X. Miao, S. Tongay, M.K. Petterson, K. Berke, A.G. Rinzler, B.R. Appleton, and A.F. Hebard, *Nano Lett.* **12** (2012) 2745-2750.

[77] T. Cui, R. Lv, Z.-H. Huang, S. Chen, Z. Zhang, X. Gan, Y. Jia, X. Li, K. Wang, D. Wu, and F. Kang, *J. Mater. Chem. A* **1** (2013) 5736.

[78] V. Yong and J.M. Tour, *Small* **6** (2010) 313-318.

[79] F.A. Jumeri, H.N. Lim, Z. Zainal, N.M. Huang, A. Pandikumar, and S.P. Lim, *J. Power Sources* **293** (2015) 712-720.

[80] M. Zhu, X. Li, W. Liu, and Y. Cui, *J. Power Sources* **262** (2014) 349-355.

[81] Z. Liu, D. He, Y. Wang, H. Wu, and J. Wang, *Synth. Met.* **160** (2010) 1036-1039.

[82] Z. Pan, H. Gu, M. Wu, Y. Li, and Y. Chen, *Opt. Mater. Express* **2** (2012) 58-65.

[83] K. Yang, C. Xu, L. Huang, L. Zou, and H. Wang, *Nanotechnology* **22** (2011) 405401.

[84] H. Bi, F. Huang, J. Liang, X. Xie, and M. Jiang, *Adv. Mater.* **23** (2011) 3202-3206.

[85] J. Liang, H. Bi, D. Wan, and F. Huang, *Adv. Funct. Mater.* **22** (2012) 1267-1271.

[86] Z. Liu, Q. Liu, Y. Huang, Y. Ma, S. Yin, X. Zhang, W. Sun, and Y. Chen, *Adv. Mater.* **20** (2008) 3924-3930.

[87] S. Kazim, M.K. Nazeeruddin, M. Grtzel, and S. Ahmad, *Angew. Chemie - Int. Ed.* **53** (2014) 2812-2824.

[88] B.J. Moon, K.S. Lee, J. Shim, S. Park, S.H. Kim, S. Bae, M. Park, C.L. Lee, W.K. Choi, Y. Yi, J.Y. Hwang, and D.I. Son, *Nano Energy* **20** (2016) 221-232.

[89] A. Nozik, *Phys. E Low-dimensional Syst. Nanostruct.* **14** (2002) (1–2): 115-120.

[90] G.B. Jean-Claude and C. Anne-Sophie, *Handbook on the Physics and Chemistry of RareEarths*, **44** (2014) 169-281.

[91] M.H, Ahmadi, M. Ghazvini, M. Sadeghzadeh, M.A. Nazari, R. Kumar A. Naeimi and T. Ming, *Energy Sci. Eng.* **6** (2018) 340-361.

[92] D.M. Chapin, C.S. Fuller and G.L. Pearson, *J. Appl. Phys.* **25** (1954) 676.

[93] C.W. Tang 2-layer organic photovoltaic cell. *Appl. Phys. Lett.* **48** (1986): 183-185.

[94] K.D.G.I. Jayawardena, L.J. Rozanski, C.A. Mills, M.J. Beliatis, N.A. Nismy and S.R. Silva, *Nanoscale* **11** (2013) 8411-8427.

[95] A.J. Nozik, *Nano Lett.* **10** (2010) 2735-2741.

[96] M.A. Green, *Mater. Sci. Eng. B* **74** (2000) 118-124.

[97] L. sa'd Basha, Cairo University, Online thesis and Dissertations. Accessed [February 2020].

[98] J.J.M. Halls, C.A. Walsh, N.C. Greenham, E.A. Marseglia, R.H. Friend, S.C. Moratti and A.B. Holmes, *Nature* 376 (1995) 498.

[99] G. Yu, J. Gao, J.C. Hummelen, F. Wudl, A.J. Heeger, *Science* 270 (1995) 1789.

[100] https://www.nrel.gov/pv/cell-efficiency.html Accessed [20 January 2020.

[101] Y. Li, B. Shi, Q. Xu, L. Yan, N. Ren, Y. Chen, W. Han, Q. Huang, Y. Zhao, X. Zhang, *Adv. Energy Mater.* **11** (2021) 2102046.

[102] J.H. Noh, S.H. Im, J.H. Heo, T.N. Mandal, S.I. Seok, *Nano Lett.* **13** (2013) 1764-1769.

[103] W. Zhao, S. Li, H. Yao, s. Zhang, B. Yang and J. Hou, *J. Am. Chem. Soc.*, **139** (2017) 7148-7151.

[104] Z. Xiao, X. Jia and L. Ding, *Sci. Bull.*, **62** (2017) 1562-1564.

[105] W.R. Mateker and M.D. McGehee, *Adv. Mater*., **29** (2017) 1603940.

[106] R. Roesch, K.-R. Eberhardt, S. Engmann, G. Gobsch and H. Hoppe, Sol. Energy Mater. Sol. Cells, **117** (2013) 59-66.

[107] P.S. Mbule *PhD theis* University of the Free State, South Africa (2013).

[108] B.E McCandless and S.S Hegedus, *Proceedings of the 22nd IEEE Photovoltaic Specialists Conference* (1991) 967-972.

[109] K. Feron, W.J. Belcher, C.J. Fell and P.C. Dastoor, *International Journal of Molecular Sciences*, **13** (2012) 17019-17047.

[110] J. Nelson, *Imperial College UK*, ISBN: 978-1-86094-349-2.

[111] J. Hou and X. Guo, *Organic Solar Cells* **3** (2013).

[112] R. Abbassi, A. Abbasi, M. Jemli, S. Chebbi, Renew. *Sustain Energy Rev.* **90** (2018) 453-474.

[113] A.R. Jordehi, *Renew. Sustain. Energy Rev.* **61** (2016) 354-371.

[114] K. Ishaque, Z. Salam. *Sol. Energy*, **85** (2011) 2349-2359.

[115] H.Q. Wang, M. Batentschuk, A. Osvet, L. Pinna and C.J. Brabec, *Adv. Mater.* **23** (2011b) 2675.

[116] M. Raugei and E. Leccisi, *Energy Pol*. **90** (2016) 46-59.

Chapter 3: Experimental and Investigation Procedures

Researchers are undertaking studies to create novel materials with improved characteristics and functioning at affordable prices compared to the existing ones. They achieve this by employing several physical and chemical methods that are designed to increase the functionality of nanomaterials by fine-tuning properties with the aim to have better control over the nanoparticle size, shape and distribution [1]. Many preparation methods and characterization techniques were used to synthesize nanomaterials and probe properties thereof. This chapter's goal is to furnish a clearer understanding of these techniques.

3.1 Thin-Film Deposition Methods

There are various routes that have been proposed to synthesise and fabricate nanomaterials wherein top-down and bottom-up approaches are being followed. The top-down approach is a process of miniaturizing or cracking down chunk/bulk materials (macro-crystalline structures) into nanomaterials (nano-crystalline structures) while retaining their original integrity. The bottom-up fabrication is the process of building of nanomaterials using smaller particles the size of an atom (aggregating materials using molecules/atoms). These two approaches are very useful and they bring vital role in both modern industry and mostly in fields of nanotechnology. For the preparation of nanomaterials, attrition or ball-milling is a usual illustration of top-down method whereas the colloidal dispersion is an excellent illustration of bottom-up approach [2]. Many bottom-up approaches have been developed for the preparation of nanomaterials through condensation of molecules on the substrate to coalescence of atoms in liquids. These approaches are important for growing thin films which are materials deposited on the substrate of choice to make a layer of solid material. The solid material formed represents the most condense phase interconnected into a crystal structure that is mostly crowded by impurity atoms. In the study undertaken here three various deposition methods were explored for growing thin films and they are explained in the following subsections.

3.1.1 Spin coater

Spin coater is one of the well-known ubiquitous methods for growing uniform thin film materials on the surface of substrates through the process called spin coating. This method has been used since the beginning of 20th century and it was developed with time because of technological advances. It has wide range of applications in industries and technology sectors

for growing of thin films because of its high structural uniformity [3]. In the field of micro-fabrication, it is employed to create thin films thinner than 10 nm. This method has more intense use in fabrication of transparent oxides on quartz or glass substrates with the advantage of self-cleaning and self-sterilizing properties [4]. Thin films of different thicknesses ranging from few nanometres (nm) to a few micrometres (µm) can be developed using this method. However, the process of growing thin films with spin coater is inherently less controlled as opposed to techniques that utilizes vapour, for example chemical vapour deposition (CVD). But in relation to dip-coating and drop-casting methods which we tested; one can grow a uniform good quality thin films hence we opted to use spin coater for the rest of research we conducted. The added advantage of the method is its simplicity, viability to setup which leads to high consistency and effective use. However, small changes in the spin process's parameters can have a big impact on the coated film's appearance hence the same parameters must be used for consistency when doing repeatability for spin coating [5].

The method is considered to be very effective on deposition of materials with good properties for photovoltaic applications due to increased number of publications. It was shown that during deposition of polymer materials while fabricating devices using this method, excessive crystallization can be avoided as the polymer is either separated or crystallized [6]. Thus, with the knowledge we have about this method we considered it best to enhance better results for our research findings.

3.1.1.1 Spin coater operating principle

The spin coater equipment used for growth of thin films in this study is VTC-100A Vacuum Spin Coater provided by MTI Corporation with the schematic represented in Figure 3.1.

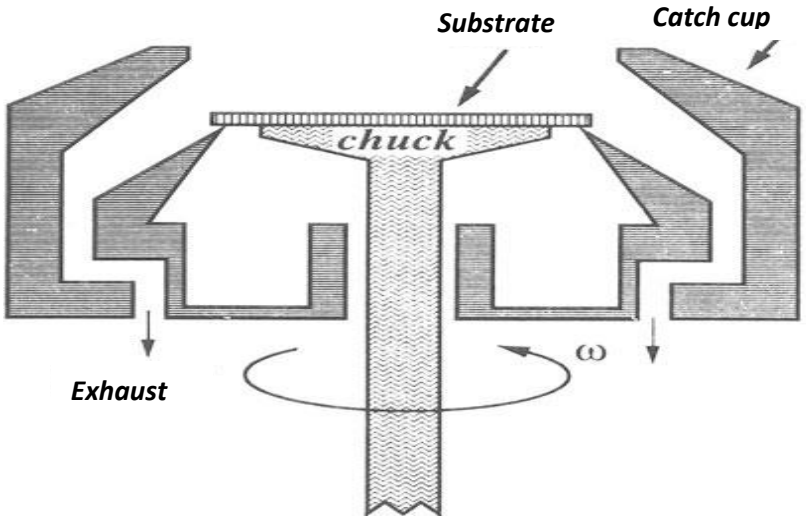

Figure 3. 1 The schematic representation of a typical spin coating system [7].

The catch cup in the schematic prevents the solution from spilling off to the environment for the safety of users. Then the spilled solution goes down the exhaust which is connected to the vacuum pump that sucks it to avoid contamination from re-circulation of various materials deposited. Additional component of the system is the spin chuck which is responsible for securing substrates from falling during the spinning process. The chuck operates at higher rotational speed while holding substrates tight by friction and centrifugal force, while allowing solution spilled to escape. It plays a role in aligning the substrate and ensuring that deposited material is uniformly distributed.

The process of growing thin films using spin-coater are clearly demonstrated by schematic diagrams in Figure 3.2. Upon growth of thin films using this system four stages (deposition, spin-up, spin-off and evaporation) takes place for the material to be coated on the surface of a substrate.

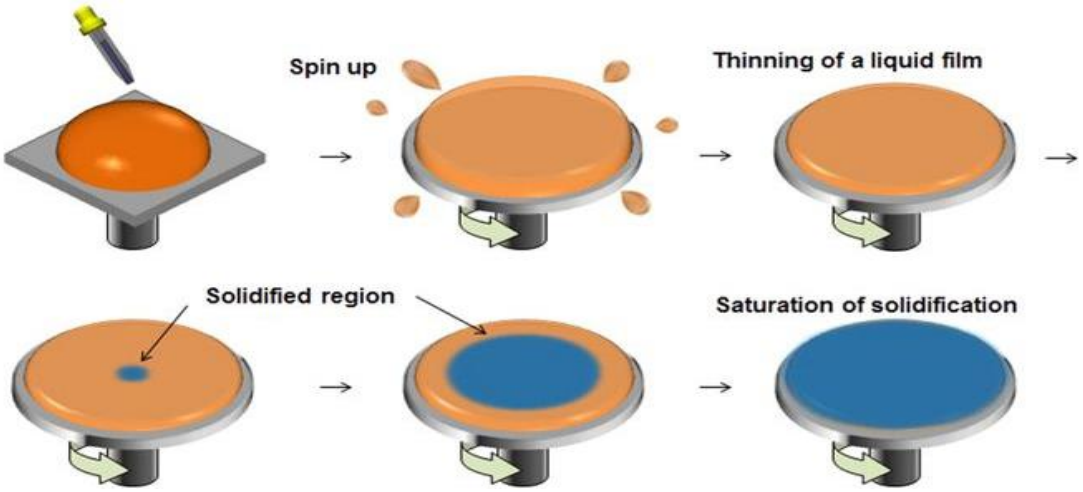

Figure 3. 2 Schematic diagram showing the spin-coating steps [8].

The process starts by loading the substrate on top of the spin chuck. In the first step called dispense, a small puddle of nanomaterials in liquid form is dropped onto the centre of a substrate which is then allowed to spin at a certain speed (typically around 3000 rpm) [9]. There are two methods of dispensing resin on a substrate namely static dispense and dynamic dispense. During the static dispense method, a small puddle of resin fluid is deposited at the centre of the substrate taking into account the size of the substrate. When working with larger substrates or material with high viscosity, a big puddle needs to be deposited so that the entire

substrate can be coated. Then dynamic dispense is the process in which a resin is deposited while the substrate is rotating at a lower speed of about 500 rpm. This helps to spread the material evenly on the substrate. Dynamic dispense is preferred over static dispense because in an event the substrate or material to be deposited has poor wettability this process has the ability to avoid voids which are likely to be formed [10]. After the dispense step, the substrate speed is increased by tuning acceleration which helps to thin the fluid such that desired thickness is attained. Spin speed for this stage is in the range 1500-6000 rpm.

The spinning occurs through centripetal acceleration which makes the solution to spread evenly across the surface of the substrate. Most of the nanomaterial's solution gets flung to the walls of the spin coater and the solution spread on the surface of the substrate forms a plasticised film. This is due to the centrifugal force together with the surface tensional force acting on the solution driving it radially outward to cover the surface of the substrate. The outward fluid flow and evaporation causes the formation of a thin film [11]. The thin film formed dries within a minute as the solvent evaporates fast due to the high air flow caused by the spinning speed. Properties of the thin film formed such as thickness etc. depend on parameters used for spinning and the viscosity of the material. Moreover, the thickness depends on the concentration of the solution as well as the solvent. When the angular speed of spinning is very high, the film formed becomes thinner. After completing the spin coating process, a separate drying step is sometimes considered for further drying without thinning the film. The separate drying is vital for thick films as it increases the physical stability of the film before handling.

3.1.2 Dip coater

Dip coating is one of the well-known techniques for growth of thin films and it is the oldest commercially applied coating process. It has a wide range of applications in industries and laboratories due to its cost effectiveness, simple processing and high-quality films [12]. In the year 1939 it was used to deposit sol-gel derived silica films from which the first patent based on it was issued to Jenaer Glaswerk Schott & Gen [13]. The use of this system in industries began in 1940s during seminars at Schott, then from the late 1950s it was adopted in the automobile industry for production of rear-view mirrors [14]. With more years passing by the method was adopted in optical coating field for antireflective and solar control glasses. The dip coating method of growing thin films is a rapid (~10s), dynamic self-assembly process with a steady and continuous nature. There are many other deposition techniques for coating

materials such as spin coater, spray coating etc. to mention few, which are practical for the growth of films through the coating process. The process is fast and simple but it is bested by the spin coater because of the uniform and thin layers it produces. When using this method, there are challenges towards obtaining homogeneous coating due to intermolecular interactions between the substrate and molecules in the solution.

3.1.2.1 Dip coater operating principle

To carry out process of dip coating one does not need any sophisticated equipment except a beaker for solution and a clamp to hold the substrate. The process of film formation takes several steps as indicated in Figure 3.3.

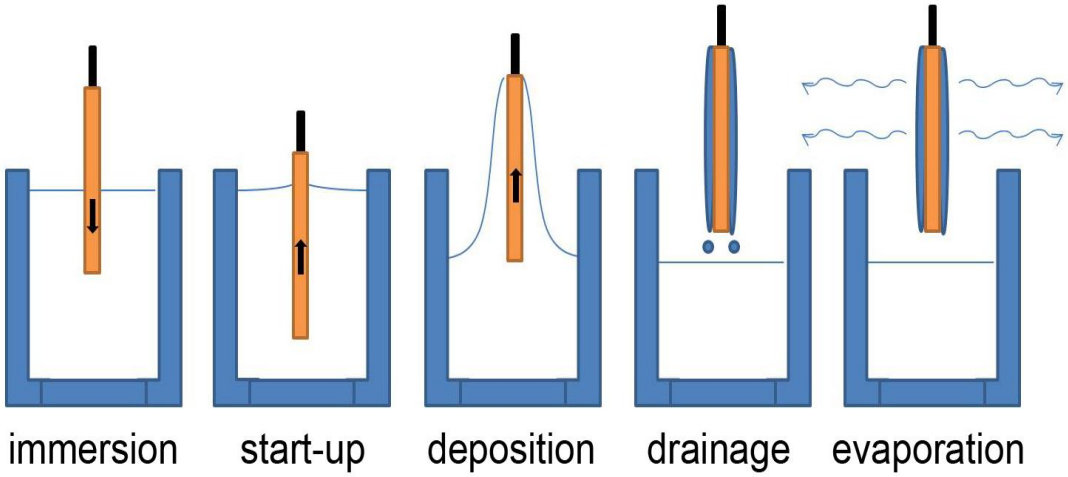

Figure 3. 3 Schematic representation of stages undertaken during dip coating process [15].

During the process of dip coating, a substrate is submerged in the solution to be coated at a constant speed. The substrate is kept in the solution for some time to allow interaction between solution and substrate for complete wetting. Then a coherent liquid film is entrained during the withdrawal of the substrate at a constant speed from the liquid coating medium. The moment a substrate is totally withdrawn a layer of material deposited is seen on both sides of the substrate and substrate is held to allow drops of solution in excess to be drained. This is followed by evaporation of volatile liquids which consolidates drying; a transition that takes place in a few seconds. After this stage, any turbulence or variation in the atmosphere normally causes inhomogeneity on the film formed. Subsequently the obtained film might need sintering to dry out organic residues and induce crystallization of the functional oxides. The thickness of the film depends on the solvent used to prepare final solution and the

withdrawal rate. However, this method was not considered best to be adopted for the entire project based on the results obtained.

3.1.3 Drop casting

Drop casting is a simple and cost-effective solution phase deposition technique for the production of thin films. The application of this method is limited to deposition on small area thin solid films, but it offers high throughput in order to be viable for industrial device fabrication [16]. This technique is designed to provide large single crystals for applications in electronics including pharmaceutical research. It has been modified to enhance the quality of deposited thin films by exposing the drop cast solution to unidirectional sound waves (~100 Hz) [17]. To some extent, it is a bit similar to spin coating technique but it does not involve spinning of the substrate during deposition. However, it aims at creating homogenous dispersion of nanomaterials which is collected and drop cast on a pre-cleaned substrate and dried to form a solid film. Although it is an easy method to adopt when conducting experiments, there are couple of parameters that needs to be optimized to get uniform and moderated surface morphology [18].

3.1.3.1 Drop casting operating principle

When performing experiments using drop casting method there's a prominent advantage as it requires no special equipment. Development of thin-films using this method takes a few stages as represented by schematic diagram in Figure 3.4. Firstly, a small volume of solution is cast on the substrate and it spreads over covering the surface.

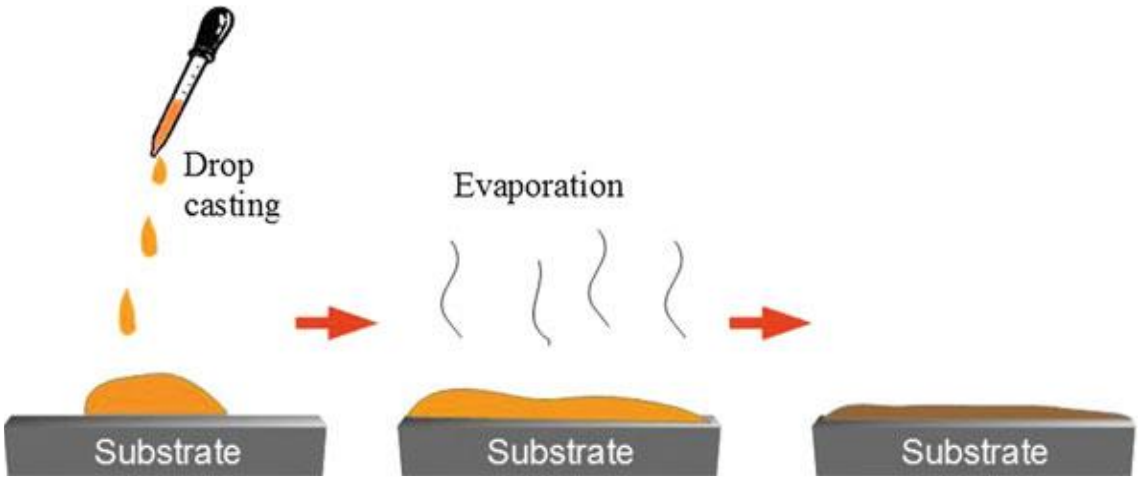

Figure 3. 4 Schematic representation of drop-casting technique [21].

The spreading of the solution is controlled by solution viscosity, surface tension, density, drop size and the impinging velocity via Weber (We) and Reynold numbers [19]. This is followed by spontaneous solvent evaporation which can be induced by heating of the substrate to speed up the evaporation process. During the evaporation, particles in the solution coalesce and make a thin film after drying. The film thickness depends on the content of solid in the solution which relates to concentration and volume drop casted on the substrate. Thin film quality and the uniformity are vital and they rely on surface tension of the substrate and solution deposited as well as the viscosity of the solution. Using this method, thin films of large surface area can be easily prepared but it is difficult to control the film thickness over the entire surface area which is a drawback of this method [20]. It is because of lack of adequate control over thin film characteristics we did not adopt drop casting for the entire project.

3.2 Device Fabrication

Fabrication of solar cell devices was done in XLIM at the University of Limoges using their clean room laboratories where all facilities are housed. Solar cell devices were fabricated by depositing layers of various nanomaterials on top of the other. Prior to fabrication a couple of processes were undertaken to clean the surface of substrate to ease the deposition and avoid contamination. During fabrication of solar cell devices, materials with various ionization potentials and electron affinities were brought together in order to create an electric field. Blending of the donor and acceptor helped with the charge collection and transfer. An organic PV active layer devised between transparent electrode and a metal electrode were created by using polymer as electron donor and graphene-based material as an electron acceptor. The ITO coated glass was etched and used as a transparent electrode.

3.2.1 Substrate etching

ITO coated substrates were placed on a support stand and two various nail polishes were applied on the 1 mm top part creating two-pixel system for etching. Beneath 1 mm polished area we left 2 mm space to be etched and covered the bottom part with two masking tapes (vinyl electrical and pressure sensitive tapes). They were then placed inside the oven for 5 min of drying the nail polishes. After drying they were detached from supporting stand and kept inside 30% hydrochloric acid (HCL) solution pre-warmed at 90℃ on a hot plate and etched for 2 min. Then substrates were removed from hard acid etching solution, placed into

DI water to stop the etching process, dried with a paper towel and tested with a multimeter to ensure proper etching. Finally, the nail polishes and masking tapes were removed and substrates were taken out for cleaning.

3.2.2 Substrate cleaning

The substrates were cleaned sequentially following standard cleaning procedure using, deionized water, acetone, ethanol and iso-propanol. They were placed inside a beaker which was put in an ultrasonic bath for a period of 10 min to get rid of any dust particles accumulated on the surface. After sequential cleaning with solvents they were blow dried using azote then placed in a UV-ozone for 15 min to ensure ultraclean surfaces free from variety of contaminants.

3.2.3 Deposition of materials

After cleaning of the substrates, the employed nanomaterials for investigation of various properties and fabrication of the devices were deposited using the spin coater. The deposition environment and resulting thin film are important based on material and its quality. GO and ZnO layers were deposited inside the fume hood. The P3HT layer was deposited inside the glove-box system which is under nitrogen rich vacuum to avoid contamination and degradation of lifetime when exposed to light.

3.3 Sample Characterization Techniques

The crystal phase of the samples was determined using advanced-state-of-the-art high-resolution XRD/SAXS system powered by guidance expert system software called Rigaku Smartlab X-ray diffractometer with CuKα (1.5418Å) radiation. Structural analysis from Raman were measured using HORIBA scientific technique. The FTIR spectra were taken at room temperature within the scan range of 400 – 4000 cm^{-1} by utilizing a Perkin Elmer spectrometer. The surface morphology was examined with the use of scanning electron microscope (Shimadzu model ZU SSX-550 Superscan SEM model with EDS and JEOL JSM-7800F thermal field emission scanning electron microscope (FE-SEM)). The chemical composition study thereof was conducted using an Oxford Instruments AzTEC energy dispersive spectrometer (EDS), with X-Max80 silicon drift detector (SDD) system, which is coupled to the FE-SEM. The optical measurements were carried-out using the (Perkin Elmer UV-VIS-NIR Lambda 1050) spectrophotometer. Photoluminescence analysis were done

using two various PL systems (Fluorolog with monochromatized 150 W xenon lamp as an excitation source and Tunable laser Fluorolog system using xenon lamp, 980 nm and YaG laser as different excitation sources. Full details on the importance of each technique and how it will be utilized for success of the project are discussed below.

3.3.1 X-ray Diffraction

The X-ray diffraction (XRD) is well known as a non-destructive method of identifying and quantitative determination of crystalline phases in solid materials such as powders and thin films [22]. XRD system uses X-rays which are electromagnetic waves with the wavelength in the range 0.01 nm – 10 nm. The X-rays were discovered by the German Professor named Wilhelm Conrad Roentgen in 1895 as he was working with cathode-ray tube in his laboratory and he won the first Nobel Prize in physics in 1901 for this outstanding work [23]. It is called a structural technique because the wavelength of X-rays ranges from the atomic scale which makes them comparable to the size of atoms, hence it is capable of probing structural arrangement of atoms and molecules in various nanomaterials. It is well known method of determining crystal structures, lattice constants, atomic spacing, grain size and degree of crystallinity in wide range of crystalline and amorphous materials [24]. The following parameters position (2θ), intensity and shape of diffraction peaks are of high importance in specifying space group, lattice parameters, chemical composition, texture, crystal structure, quantitative and qualitative phase analyses, as well as crystallite size [25, 26].

3.3.1.1 XRD operating principle

The XRD system employed to determine the crystal structure of the powdered nanomaterials and layered nanostructures in these studies is Rigaku SmartLlab technique with a schematic depicted in Figure 3.5 for components inside the chamber. Measurements were acquired using CuKα radiation (λ=1.5406 Å) at the scan rate of 0.2° s^{-1} and 2θ range (5-90°). It is a high-resolution diffractometer with novel features that assists a user with intricacies of experiments through a SmartLab Guidance software. The system consists of 9kW XG coupled with unique 5-axis goniometer and semiconductor HPAD detector “Hypix 3000” for both powder and thin film samples. Basically, it is a theta-theta diffractometer that houses variety of optical components. It consists of a tube (Cu radiation) and a scintillation detector. Moreover, there are interchangeable optical components for the tube and detector of the system. These components are encoded so that the computer can read which ones are

installed at the time of measurements. Its functionality allows measurements of powders, thin-films and liquids nanomaterial samples in 0D, 1D and 2D modes.

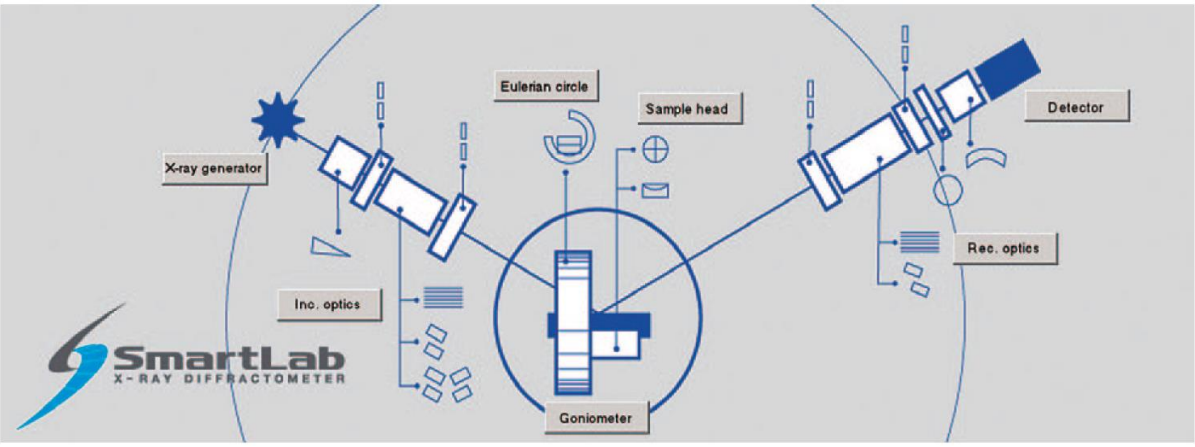

Figure 3. 5 Schematic representation of operational components of Smart lab guidance [27].

With the XRD system employed in this study three sets of experiments can be carried out depending on the scattering angle.

1. Wide angle X-ray scattering (WAXS) also called wide angle X-ray diffraction (WAXD) normally refers to the analysis of Bragg peaks scattered to the greater angles where ($2\theta > 1°$), they are known to be coming from sub-nanometre structures. This method is mostly used to analyse crystal packing and amorphous structures.
2. Small angle X- ray scattering (SAXS) provides the information on nanomaterials with the size in the range of several ten nanometres which takes place when ($2\theta < 2.3°$). It is mainly applied in the field of polymers to obtain information on crystalline lamella stacking structures [28].
3. X-ray reflectivity (XRR) is a method of analysing thin film nanoparticles where the information such as density, roughness and thickness of the films can be estimated. It involves the evaluation of incident X-ray beam intensity which is reflected by the sample at grazing angles. This method is applied in single-crystalline, poly-crystalline and amorphous material [29].

The added advantage of this technique when dealing with thin film samples is to acquire data at different grazing incidence modes that differs on the sample scanning geometry as shown in Figure 3.6:

1. Out-of-plane measurements: this mode is the well-known method of determining diffraction from different sorts of samples such as powders, bulk and thin films [30].

In this mode the scattering vector is pointed away from the surface of the sample while the observed planes are parallel to the surface. The incident X-ray beam strikes the planes and goes deeper into a sample within the range of tens of micro-meters.

2. In-plane measurements: herein, the scattering vector lies parallel to the thin film surface as the observing planes are perpendicular to the surface and the detector is moving parallel to the surface. The X-ray beam is limited to penetrate up to the depth of 100 nm of the surface of thin films. This mode helps to detect diffractions from extremely thin-films at minimized background intensity of the substrate [31].

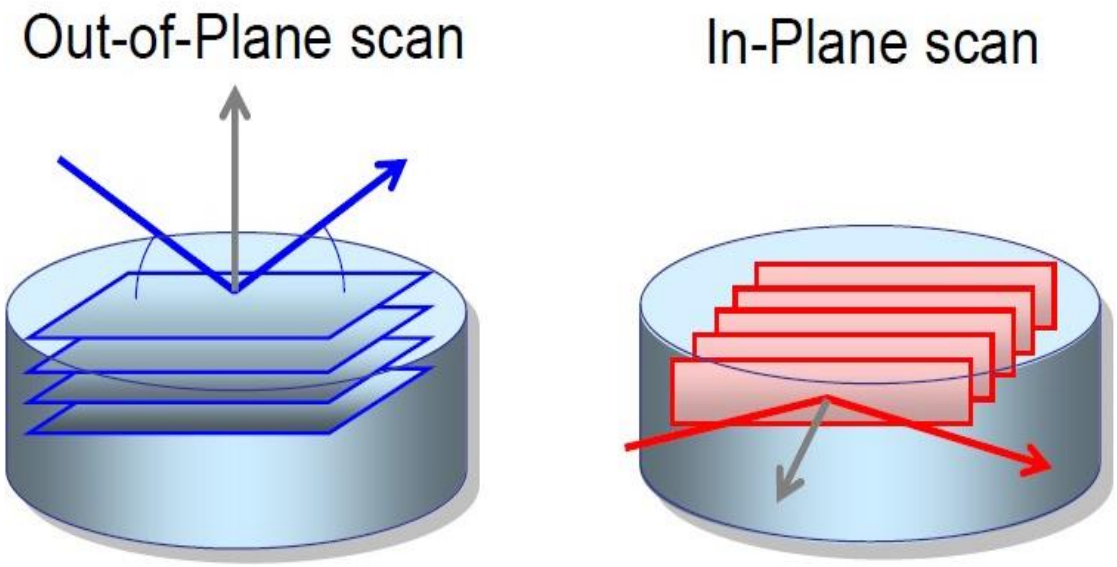

Figure 3. 6 Schematic representation of different scan modes of thin-films [32].

Upon operation of the system, X-ray photons from the X-ray tube interfere constructively with the crystalline sample on the sample stage. The high energy charged particles, such as electrons, are accelerated and collide with a metal target, such as Cu, in a sealed tube that is under vacuum to produce X-rays [23]. After collision with the target anode, the fast-moving electrons gets decelerated and less than 1 % of their energy is turned into X-rays, whereas 99 % of it is transferred into heat. Part of the focused X-ray beam is transmitted and part of it is absorbed by the sample as it interacts with atomic planes, in the process some are scattered and refracted while others are diffracted. The moment an X-ray beam is diffracted because of interaction with the sample as presented in Figure 3.7, one can measure the distance between the planes of the atoms by making use of Bragg's law shown in equation (3.1)

$$n\lambda = 2dsin(\theta) \tag{3.1}$$

where n symbolizes the order of the diffracted beam, λ is the wavelength of the incident light

beam, θ is the angle of incidence, and d denote the inter-planar spacing that sets the difference between the length and path for the rays scattered from the top plane and the rays scattered from the next plane parallel to the top one.

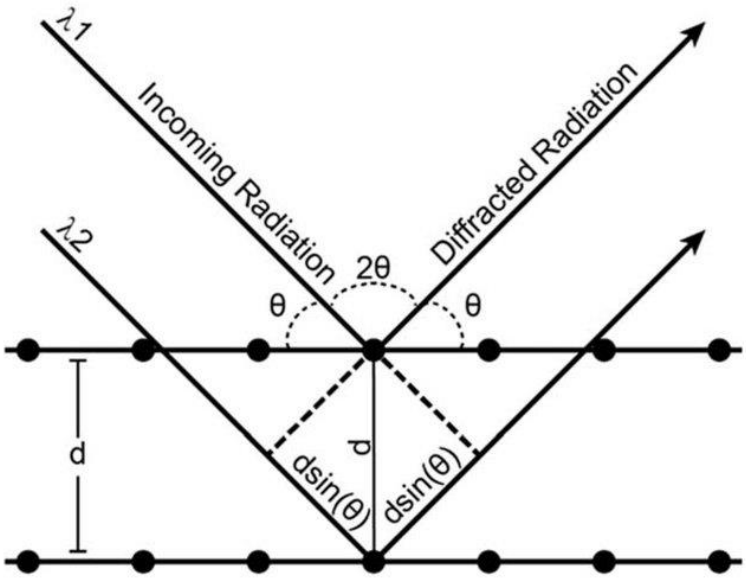

Figure 3. 7 Schematic representation of Bragg's law [33].

After collimating, the resultant X-ray is aimed at the sample. The intensity of the reflected X-rays is measured when the sample and detector are rotated. When the incident X-rays striking the sample conform to the Bragg law, constructive interference takes place and the sample's distinctive diffraction peak is seen [34]. The X-ray waves that were incident on the sample creates the oscillating electric field that interacts with the electrons in the sample. The incident angle of the X-rays is equivalent to the one of reflected X-rays. These electrons scatter the incoming electromagnetic radiation coherently. Then the diffraction takes place the moment atoms arranged in a periodic array scatter radiation at a specific angle [35].

3.3.2 Raman Spectroscopy

Raman spectroscopy is a non-destructive spectroscopic chemical analysis technique that helps to determine information about chemical phase, structure, crystallinity, polymorphs and molecular interactions. It relies on the Raman effect, which is a phenomenon of inelastic scattering of monochromatic light (Raman scattering) mainly coming from laser source. The Raman effect was discovered by Sir C.V. Raman and K.S Krishnam who obtained a Nobel Prize in Physics in the year 1930 for observing Raman scattering effect experimentally [36]. It provides information about intra- and inter- molecular vibrations including the reaction

mechanisms with kinetics thereof. Researchers from various fields makes use of this system to analyse materials in different forms containing molecular bonding such as solids, liquids, gases, powders and gels.

Raman is a widely used technique for the analysis of carbon-based materials. It is a spectroscopic technique that measures low-frequency, rotational and vibrational modes in a system [37]. The system is used to gain information on the quality of nanomaterials, their structure, including the existence of defects and the extent of functionalization [38]. It also helps to measure the bonding characteristics, estimate the thickness of films and help with hybridization status of the formed nanostructures. Moreover, it is aimed at measuring how materials can absorb or transmit light at various wavelengths.

3.3.2.1 Raman operating principle

Structural analysis of thin film nanostructures was conducted using HORIBA scientific system depicted in Figure 3.8 which is equipped with a 532 nm He-Ne laser with a spot size of approximately 2-3 nm which yields a spectral resolution better than 2 cm^{-1}.

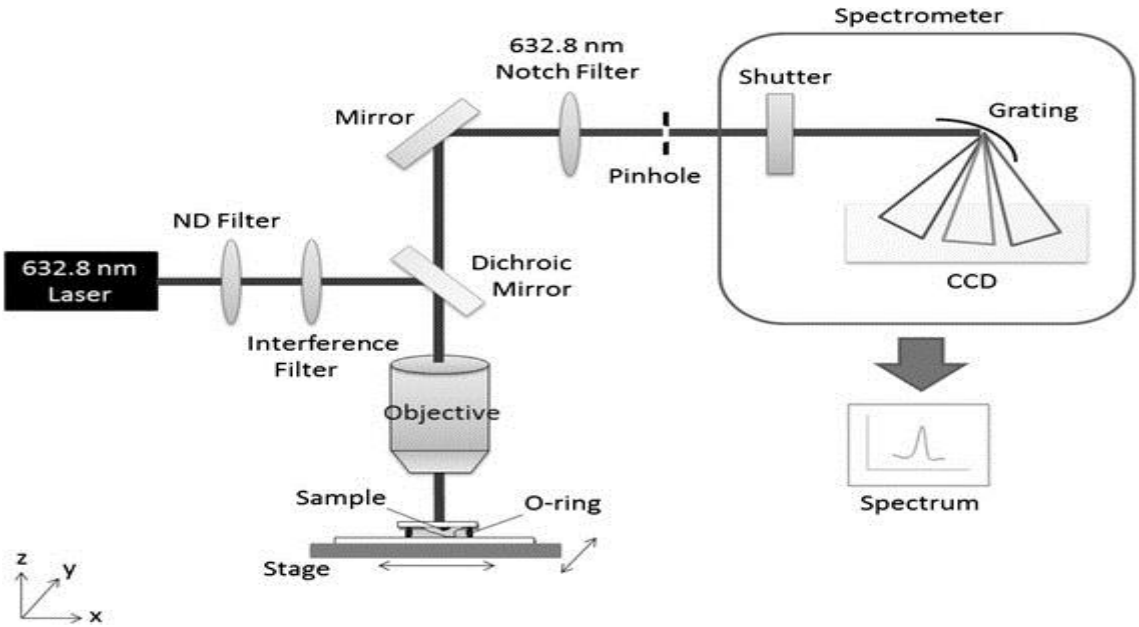

Figure 3. 8 Schematic diagram of the Raman platform setup [41].

The moment light interacts with molecules inside the sample, most of the photons get scattered at the same energy coming from an incident light beam. The energy of scattered photons gets shifted giving information about the vibrational modes in the system. Most of the incident monochromatic laser light has equivalent frequency compared to the frequency

of scattered light which initiates Rayleigh scattering. The smaller portion of scattered light has a frequency which differs with that of incident light and initiates Raman scattering. In most instances, the scattered light is measured at a right angle relative to the incident light [39, 40].

Thus, after illuminating the sample with laser light, lenses collect that light from the spot and sends it through a monochromator. Elastic Rayleigh scattering causes some wavelengths to be closer to the laser line than others, and these wavelengths are filtered out while the remaining light is scattered onto a detector.

It is of high importance to see change in polarization during molecular vibrations so that we can get a Raman spectrum. The Raman spectrum is obtained due to inelastic collision between incident monochromatic light and molecules in the sample. The Raman spectrum is a distinct chemical fingerprint for different materials which helps to identify unknown materials and distinguish them from others. From the spectrum of a certain material, we obtain peaks that indicates the intensity as a function of wavelength shift corresponding to peak position of Raman scattered light. Every peak represents a molecular bond vibration which includes C-C, C=C, N-O and C-H among others. During acquisition of measurements, the spectrum of Raman can be recorded in the range 4000-10 cm^{-1}. It is of noting that active normal modes of vibration in a Raman system for organic molecules transpires in the range 4000-400 cm^{-1}. Based on the design and optical components of Raman technique, typical Raman spectra covers the wavenumber region between 400-5 cm^{-1} and 4000-3800 cm^{-1} [42].

3.3.3 Fourier Transform Infrared Spectroscopy

The Fourier Transform Infrared Spectroscopy (FTIR) is an inexpensive spectroscopic technique for analysis of crystalline solids, amorphous materials and films [43]. The IR radiation was first discovered in 1800s by Sir William Hershel, and the potential use of IR spectroscopy was recognised for academic and industrial purpose in the middle of 20^{th} century. This led to the implementation of FTIR spectrometers which were using interferometer discovered by Albert Michelson [44]. It is mostly utilized to determine the types of functional groups that are present in the molecule [45]. FTIR uses invisible electromagnetic radiation called infrared found in the wavelength region (14286 - 10) cm^{-1}. Within that range researchers are more interested in the region (4000 - 400) cm^{-1} which is crucial for chemical analysis. All frequencies obtainable within this range contains a set of

functional groups in organic molecules. It can be used to identify absorption and photoconductivity of different materials that comes in various forms of matter (solids, liquids and gases) including unknown mixtures.

This device has the capacity to immediately track the vibrations of the functional groups that define molecular structure and control the progress of chemical reactions. Additionally, it helps to identify the presence of organic molecules and elements in our nanomaterials. The organic molecules which can be investigated have molecular bonds classified as electronic, translational, rotational and vibrational. In the spectrum, functional groups are seen with narrow spectral lines which represents specific structural feature. In our studies it was utilized to evaluate the types of compounds formed and investigate the bonding interactions or molecular structure in graphene nanomaterials.

3.3.3.1 FTIR operating principle

The spectroscopic technique used for the analysis of bonding interactions in graphene based nanostructured materials is Perkin Elmer Spectrum 100 infrared spectrometer.

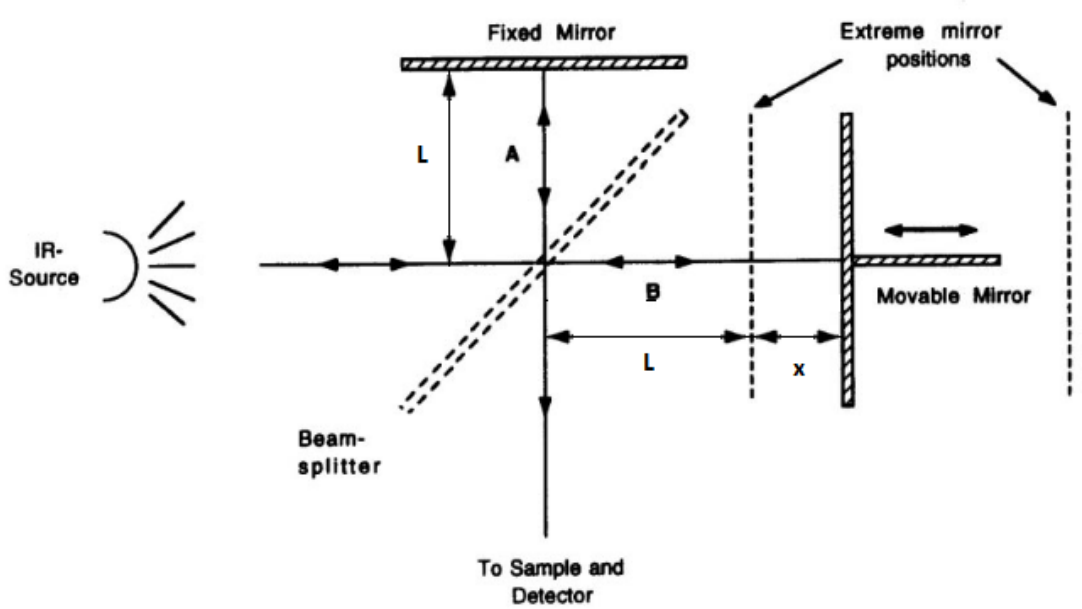

Figure 3. 9 Schematic representation of Michelson interferometer as used in FTIR spectroscopy [48].

FTIR works on the principle of Fourier transformation by first utilizing an interferometer to create an interferogram of a test signal, and then applying a Fourier Transform to the interferogram to produce the final spectrum [46]. The system is composed of interferometer, high-pressure mercury lamp, silicon-carbide rods, detector and data acquisition terminator

[47]. It uses black body to emit thermal radiation within its wavelength scan. The light beam (infrared radiation) gets collimated and goes through Michelson interferometer as presented in Figure 3.9. In this process, the light beam passes through a sample and gets absorbed while part of the beam is transmitted. The molecules get excited during absorption of IR radiation and reaches higher vibrational state. After absorption, those frequencies interact with the molecules to give fingerprint information on the chemical composition of the nanostructures. The acquired spectrum is given as absorption and percentage (%) transmittance versus the corresponding wavenumber giving molecular fingerprint of nanostructures.

3.3.4 Field Emission - Scanning Electron Microscope

The scanning electron microscope (SEM) is a surface morphological technique that primarily aims to assess the shape and size of materials by scanning with a high-energy beam of electrons in a raster scan pattern [49]. The first scanning microscope with a resolution limit of 100 µm was built by Knoll in the year 1935. Then a German Physicist Manfred von Ardenne outlined the theoretical principles underlying the system [50]. With more efforts taken in that space, Zworykin developed the first working SEM who demonstrated how secondary electrons created topographic contrast by positively biasing the collector relative to the specimen [51]. SEM is a scientific tool that examines items on a very tiny scale using a stream of extremely powerful electrons [52]. SEM is used to study the surface morphology (shape and size) and it assists with information about density of states of materials. It can also operate in conjunction with energy dispersive spectroscopy (EDS) for chemical composition (elements and compounds) of the sample's surface [49].

3.3.4.1 SEM operating principle

The SEM technique employed in this study is field emission scanning electron microscopy (FE-SEM) JEOL JSM-7800F with extremely high resolution, coupled with energy dispersive X-ray spectroscopy (EDS) and cathodoluminescence (CL). FE-SEM is the advanced state of the art system driven by recent developments in nanotechnology to give higher resolution and probing more information from the sample. The system has super hybrid lens (SHL) that provides extreme resolution of 0.8 nm at 15 kV and 1.2 nm at 1 kV. It generates a magnified image with a very low incident electron energy to reveal surface structures of extremely fine nanomaterials. In Figure 3.10 we have a schematic representation of FE-SEM which uses cold source to provide extremely focused high and low energy beam in contrast to standard

electron microscope that uses tungsten filament to generate electron beam. Field emission is known to be the emission of electrons which are ejected from the surface of a conductor due to strong electric field encountered.

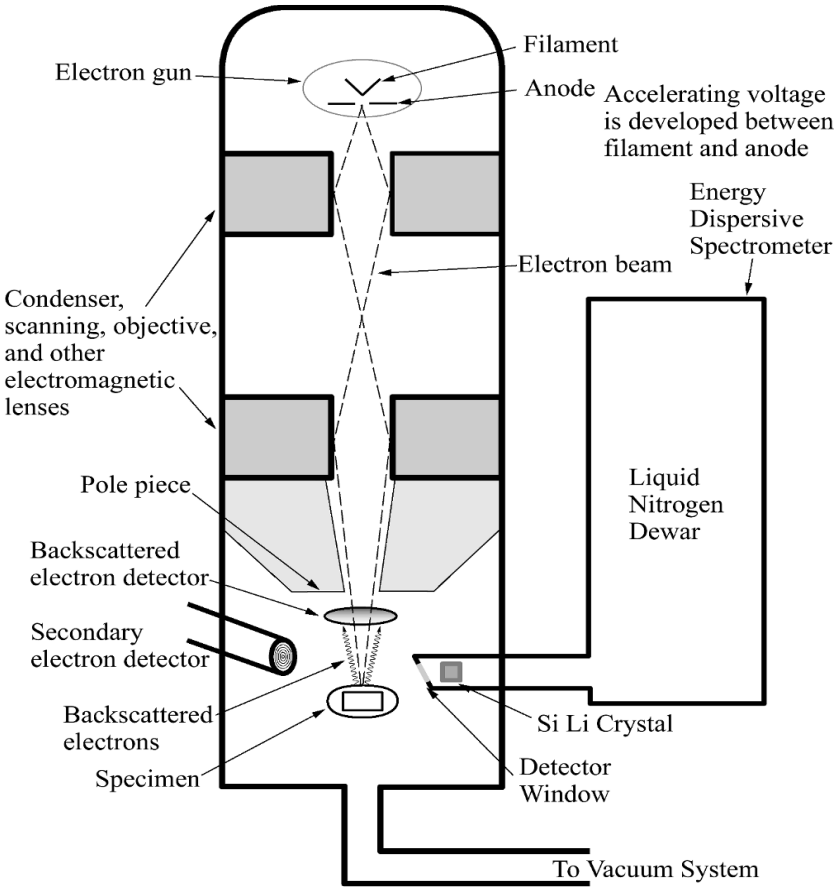

Figure 3. 10 Schematic diagram of electron beam column in SEM equipped with EDS [53].

The significant components of the FE-SEM entail the electron column, scanning system, detectors (secondary electron, back-scattered), specimen holder, display and the electronic controls. These components are housed inside the extremely high vacuum (~10^{-6} Pa). At the top of an electron column there's an electron gun which produces an electron beam. The electron column consists of two electromagnetic lenses in series (condenser lens and objective lens). These lenses direct and focus electron beam to the surface of a sample as a small probe which scans across the surface helped by the scanning coils. The projected electron beam ejects secondary and back scattered electrons when they come into contact with sample. Upon beam interaction with the atoms in the sample, an electronic signal is generated which contains information about the sample's surface topography and composition including properties such as electrical conductivity [52]. That signal is collected by detectors and sent to the viewing screen, producing an image.

3.3.5 Energy Dispersive Spectrometer (EDS)

Energy dispersive spectrometer (EDS) also known as energy dispersive X-ray spectroscopy (EDX) is an analytical technique which gives the information on chemical composition of various materials. Typically, it comes in conjunction with the SEM system to assist with chemical analysis of the obtained surface morphology. The EDS detectors were initially developed in the 1960s targeting applications in the nuclear space. In about a decade, they were incorporated for analysis in microscopic techniques such as SEM and transmission electron microscope (TEM). SEM became an indispensable technique for various applications in cutting-edge research laboratories over the years. The added advantage of using EDS system is the ease with which many different samples can be subjected to experimentation. It is a powerful method of identifying individual elements present in the surface layer of the sample. These elements are detected through process known as X-ray mapping. The system has the capability to do chemical composition on many different materials to a spot size in the range of few microns and generate elemental composition maps over a much broader raster area. The ability of this system allows the identification of materials and the impurities and helps to estimate their relative concentrations.

3.3.5.1 EDS operating principle

The components of an EDS system include an X-ray detector for detecting X-rays, liquid nitrogen dewar for the cooling process as well as software for analysis of the energy spectra. EDS relies on the interaction of X-rays with the sample where the system detects the X-rays from the sample during irradiation with high beam of electrons. When the focused electron beam interacts with the sample, electrons are ejected through the inner-shell ionization as presented in Figure 3.11 (a) and (b). The position left by an ejected inner shell electron gets occupied by a higher energy electron from the outer shell. During the interactions, a photon with the energy equivalent to that of the difference of the energy levels of the two shells may be produced [54]. Most of these photons possess energy in the X-ray range. Then the EDS detector divides the X-rays received from various elements into an energy spectrum which is then analyzed to distinguish specific elements. The amount of energy received from X-rays detected helps to get the identity of the atom thereof [34]. The system detects and measures X-rays produced inside the sample. X-rays travels some distance when emitted before

reaching the detector. While travelling, there is a possibility of X-ray absorption, and X-rays varying in energies possess various probabilities of absorption.

The system has a detection limit which allows it to identify elements from atomic number 4 (Be) to 92 (U). Furthermore, the limit depends on sample surface conditions, if the surface is smooth the limit detection is lower. It can detect major and minor elements with concentrations higher than 10 wt% (major) and minor concentrations (1-10 wt%) and 0.1 wt% for bulk materials [53]. The EDS generates a spectrum which consists of spectral peaks that represents the compound under investigation and composition thereof. Qualitative analysis of samples yields lines in the spectrum and is clearly outlined due to the simplicity of X-ray spectrum. The obtained spectrum is presented as a plot of X-ray counts as a function of energy in (keV) which is then interpreted using the software.

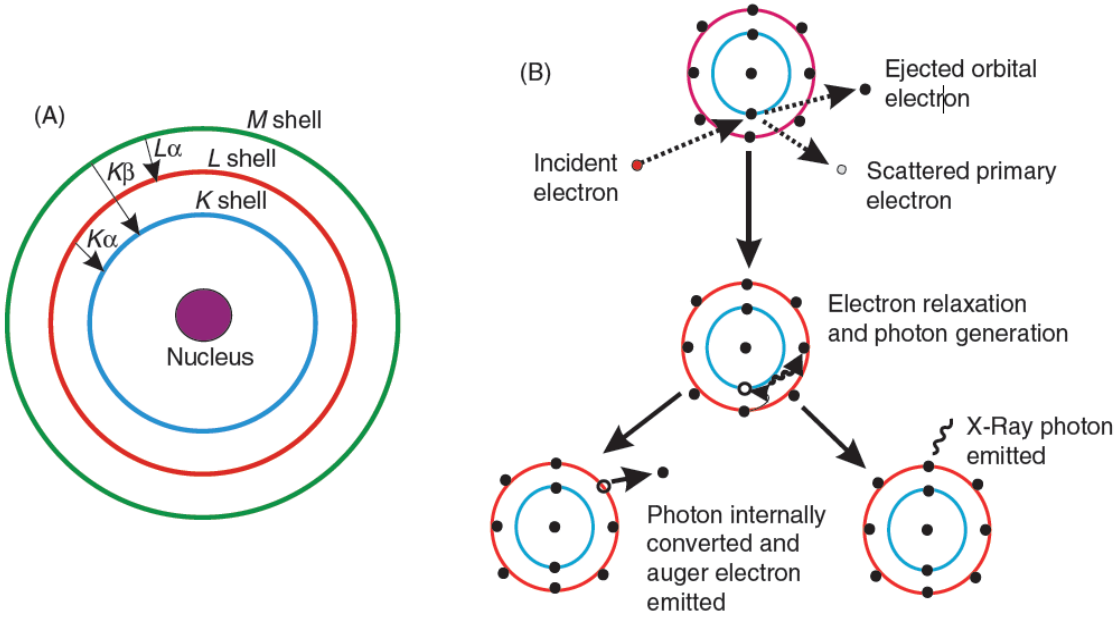

Figure 3. 11 (a) Schematic representation of electronic transitions in an atom leading to X-ray emission (b) interactions as an electron from the electron beam encounters an atom [55].

3.3.6 Ultraviolet Visible Near Infra-Red Spectroscopy

UV-Vis is an important spectroscopic characterization technique for qualitative and quantitative analysis of materials upon interaction with electromagnetic radiation. The system provides information on optical properties of materials such as band gap energy and size distribution and it serves as complimentary to the fluorescent spectroscopy [39]. The system evolved with years until the first combined UV-visible absorption spectrometer named Cary

11 was built by Varian in 1947 [56]. It is capable of analysing liquid, solid and gaseous samples with a wide range of applications in physical, chemical and biological research. It helps to monitor electronic transitions using light in the near ultraviolet, visible and near infrared regions from ground state to excited state in the target material. With this system one can achieve the optimum level of sensitivity, resolution and speed up to the NIR range. Two large sampling compartments, a number of snap-in modules, integrating spheres and a special patented Universal Reflectance Accessory (URA) are key components of this technique.

3.3.6.1 UV-VIS-NIR operating principle

The instrument used for optical properties is LAMBDA 1050 UV/VIS/NIR spectrophotometer from PerkinElmer with a resolution of about 1 nm shown in Figure 3.12.

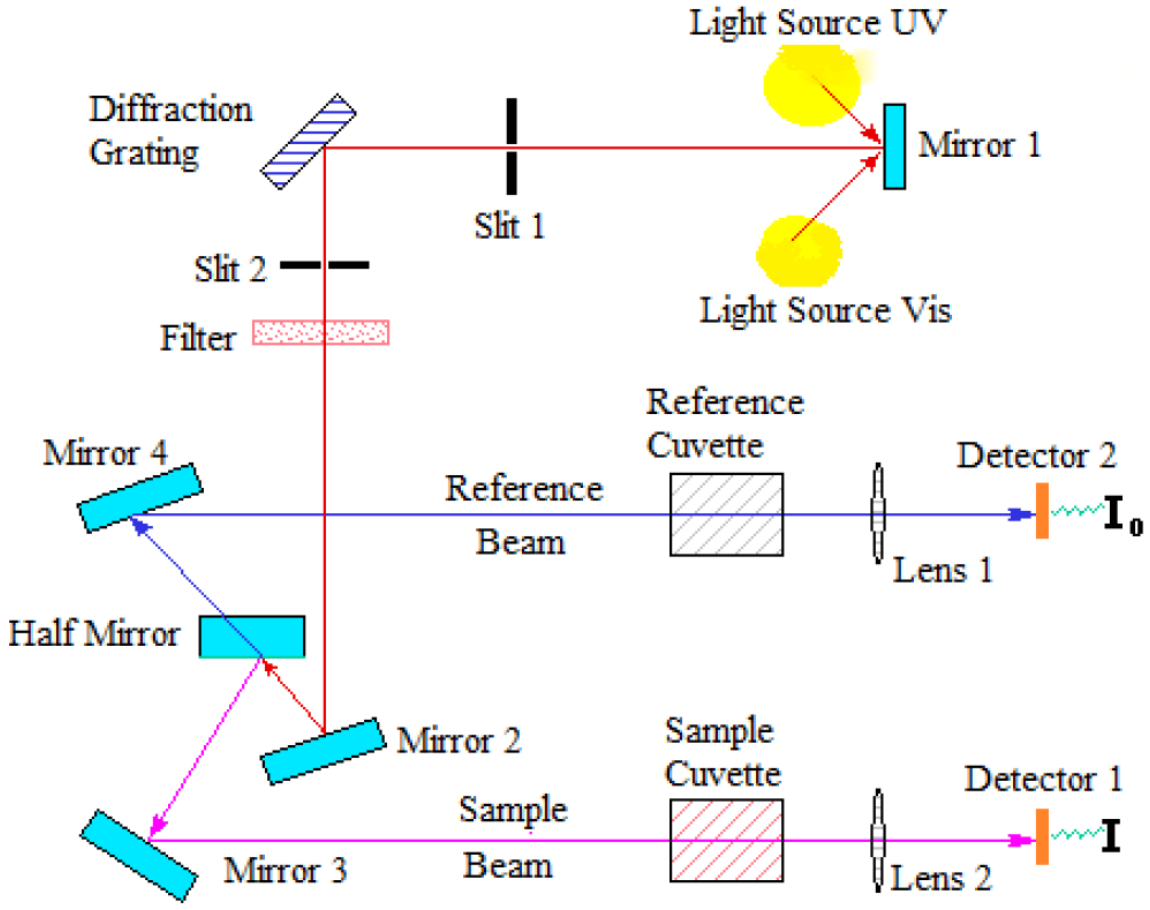

Figure 3. 12 Schematic diagram of UV/VIS/NIR spectrometer [58].

It consists of numerous vital components that includes light source, monochromator, sample holder, detector, signal processor and readout, all working together to facilitate the measurements on samples. The technique uses various electromagnetic radiation wavelengths

for data acquisition (UV radiation: 300 – 400 nm obtained using deuterium lamp, Vis radiation 400 – 765 nm and NIR radiation: 765 – 3200 nm which are covered by tungsten lamp). These ranges are crucial as their energy differences relates to electronic states of atoms and molecules.

During operation, the sample is irradiated with a beam of light which gets focused to the diffraction grating (monochromator) that splits it according to the respective wavelengths. After beam splitting, one beam gets directed to the sample while the other one is sent to the detector as a reference. The intensity of light sent to the sample is measured prior and after interaction with the material. For absorption to take place, light radiation (photons) must be enough to promote electrons from ground state to the first excitation state. After interaction between light and the sample, which is positioned inside an integrating sphere, light gets diffusely scattered by the sample while the other one is absorbed by the sample. The integrating sphere collects scattered light which gets detected at specific wavelength by (photo detector) that converts it into an electrical signal of certain intensity. The detector differentiates the collected light beam from the source beam to get the quantity that has been absorbed. Thus, an output is then plotted graphically in a spectrum as absorbance, reflectance or transmittance versus wavelength (nm) based on the chosen method of acquisition. All spectrums were corrected for substrate absorption with the appropriate baseline. The obtained absorption measurements were then normalized using the optical density (OD) which is evaluated according to equation (3.2):

$$I_T = (I_0 - I_R) \times 10^{-OD \times d} \tag{3.2}$$

where I_T, I_0 and I_R are the transmitted, impinging and reflected light respectively and d represents the thickness of a sample.

Upon interaction between matter and electromagnetic radiation, there are a couple of processes that transpires. Our focus on UV-VIS-NIR spectroscopy relies on the following processes:

1. Absorbance: is regarded as the intensity of light detected after part of it is reflected by the object while another is transmitted. It is the amount of light absorbed by the sample which is indirectly measured relative to the initial intensity that reached the sample. The absorbance measurement is mainly acquired to the solid materials such

as powder samples. This method was of high interest to our studies for investigating our solar cell devices respond to electromagnetic radiation.

2. Reflectance: is considered as the ratio of the electromagnetic energy reflected in comparison to the incident electromagnetic energy which comes from the source. Here we come across diffuse reflectance whereby light beam gets reflected in various directions due to rough surface of materials such as powders. This mode is mainly applied when working with thin film samples. General example can be a metallic sample that would reflect the incident beam backwards upon arrival at the surface.
3. Transmittance: is known as the ratio of the light intensity (I) transmitted through the sample to the intensity transmitted through the reference blank (I_0). It takes place when light passes through the sample and it is often given as a fraction of 1. This mode is mostly used to obtain information on materials that are sufficiently transparent (through liquid samples) to allow certain amount of light beam to pass.

The aforementioned quantities are somehow related by the basic principle of quantitative analysis called Bouguer-Lambert-Beer rule to allow conversion among them [57] as follows:

$$T = I/I_0 = e^{-kbc} \tag{3.3}$$

where k is the proportionality constant, b is the path length and c represents the concentration of the absorbing species. Equation (3.3) can be transformed into linear expression by applying the logarithm on both sides:

$$A = -\log T = -\log(I/I_0) = \log(I_0/I) = \varepsilon bc \tag{3.4}$$

and ε represents the molar absorption or an extinction coefficient. The expression presented in equation (3.4) well known as Beer's law which states that the absorbance is directly proportional to the number of molecules that absorb radiation at the specified wavelength.

3.3.7 Photoluminescence Spectroscopy

Photoluminescence (PL) is a well-known powerful non-destructive optical technique which is utilized to probe the electronic structure of various materials. It is a very useful physical technique to disclose the efficiency of charge carrier trapping, immigration and transfer in materials of different sizes and shapes [59]. The first recorded observation of photoluminescence was in 1965 by Nicolas Monardes, a Spanish physician and botanist who saw buish opalescence fluorescence from water infusion from the wood of a small Mexican

tree [60, 61]. This technique uses high energy photons to excite various forms of matter. Thus, one can clearly see that different forms of luminescence are described based on the mode of excitation. Materials that shows luminescent properties when subjected to the PL system to give out luminescence are called phosphors. The system is mainly used to examine the steady-state and time-resolved measurements.

The luminescence emission coming from photoluminescence spectroscopy can be sub-divided into three categories:

1. Fluorescence: Is known as an emission of light that ceases immediately after the removal of energy input. The emission coming from a material that fluoresces is very fast in a sense that it takes only short period of time in (ns).
2. Phosphorescence: Is considered as the emission of light that persists even after the removal of the excitation source. The light coming out from a material that phosphoresces usually last for a longer period ranging from hours to couple of days.
3. Delayed fluorescence: this is described as a decaying long-term ultra-weak photon emission after material has been exposed to light.

The difference between these forms of photoluminescence is based on the time an emission lasts after the removal of an excitation source which is 10^{-6} s between fluorescence and phosphorescence. The fluorescent and phosphorescent materials are mainly encrypted in documents such as passports and currency notes to minimise frauds because they can only be seen under UV illumination but not normal lighting.

This spectroscopic technique has a diverse range of applications in many scientific and technological fields such as biology, chemistry, materials science, medicine and physics [60, 62]. Among others the system helps with the detection of small amounts of impurities in naturally occurring solutions such as river and groundwater [63].

3.3.7.1 PL operating principle

The photoluminescence spectroscopy employed in this study is Fluorolog 3-2-IHR-TCSPC-P photoluminescence. Different excitation sources such as a laser, a xenon lamp or synchrotron radiation are used to create electron hole pairs in the structure of a sample to attain photoluminescence. The optical light generated from the aforementioned source is collimated to the sample using optical lenses. The tunable-laser PL uses laser and xenon lamp sources which has wavelength selectors, sample illumination and various detectors. When taking

measurements, materials are excited using either of the sources which has high power energy greater than band gap of materials. In order to get photoluminescence, light is directed onto the sample from the lamp housing as indicated in Figure 3.13. That light gets absorbed by the sample during the process called photo-excitation and re-emits it in the form of visible light giving off luminescence hence (photo-luminescence).

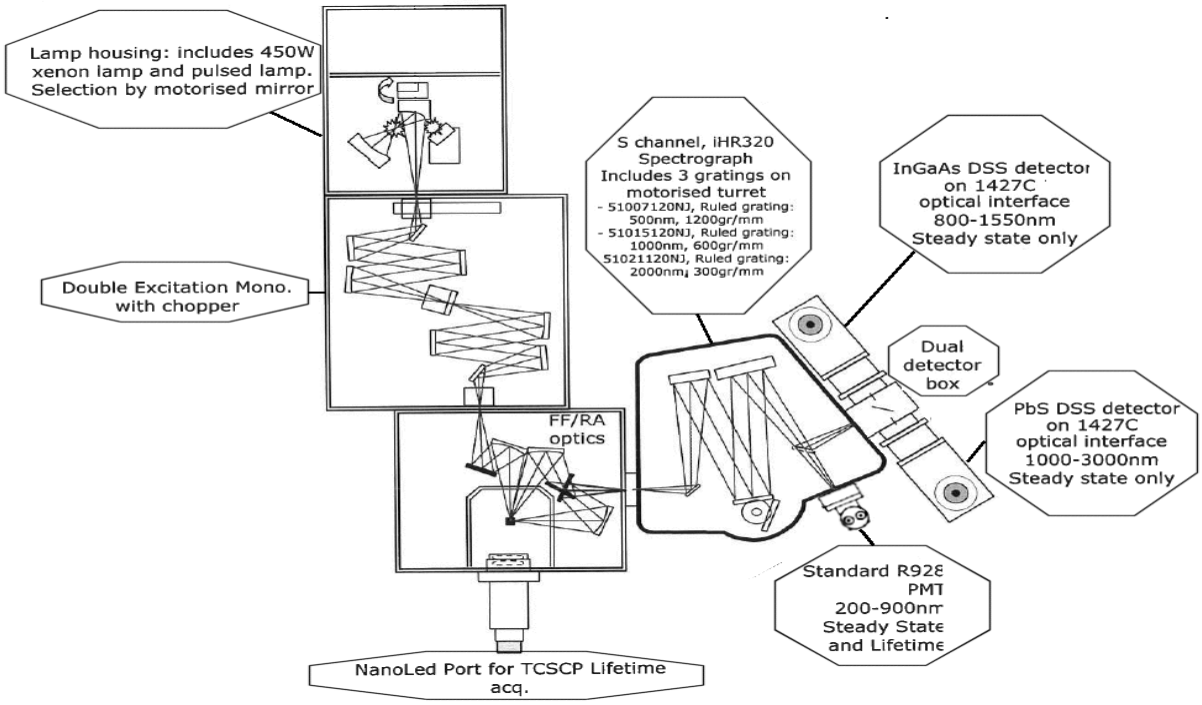

Figure 3. 13 Fluorolog 3-2-IHR-TCSPC-P photoluminescence setup schematic [64].

Upon completion of the measurements, the output signal comes as PL intensity as a function of the obtained light wavelength. That signal is a result of two main photo-physical processes during the creation of electron hole pairs and recombination thereof. The light intensity obtained while acquiring the spectra helps to understand properties of different materials which includes defects and their concentration. From that information full understanding of recombination mechanisms can be well understood looking at electronic transitions from the excited state to the ground state [65]. The PL lifetime measurements were conducted by employing FLS980 spectrometer (Edinburgh Instruments, UK), using time correlated single photon counting (TCSPC) and a picosecond diode laser at 509 nm as excitation source with temporal width of 150 ps.

3.3.8 Profilometry

Profilometry is an analytical technique mostly employed to evaluate surface profile of materials to quantify its roughness. It uses a probe which is moved on the surface of the films to acquire the height of deposited material to get their thickness with vertical resolution in the nanometer regime. The technique has been in existence for as long as four (4) decades and it has gained more advancements with improvement in technologies. Because of enhanced developments the system is gaining wide range of applications in industrial fields, optics manufactures, research and development. Lately it is of great use in the solar cell market where photovoltaic solar cell manufactures adopted it. Most scientists still prefer these techniques over optical ones because of accumulated measurement and the analysis technique to data, self-reliance by measuring direct contact with the actual measurement surface, and compatibility with accumulated measurement data from the past [66]. It can be used to analyze materials with different surfaces ranging from two-dimensional (2D) roughness surface, the step height analysis, three-dimensional (3-D) mapping as well as stress on thin films.

3.3.8.1 Profilometry operating principle

The system employed to determine thicknesses of thin-films is conventional contact-type called (Dektak 6M Veeco, US) surface profilometer with a 12µm shown in Figure 3.16.

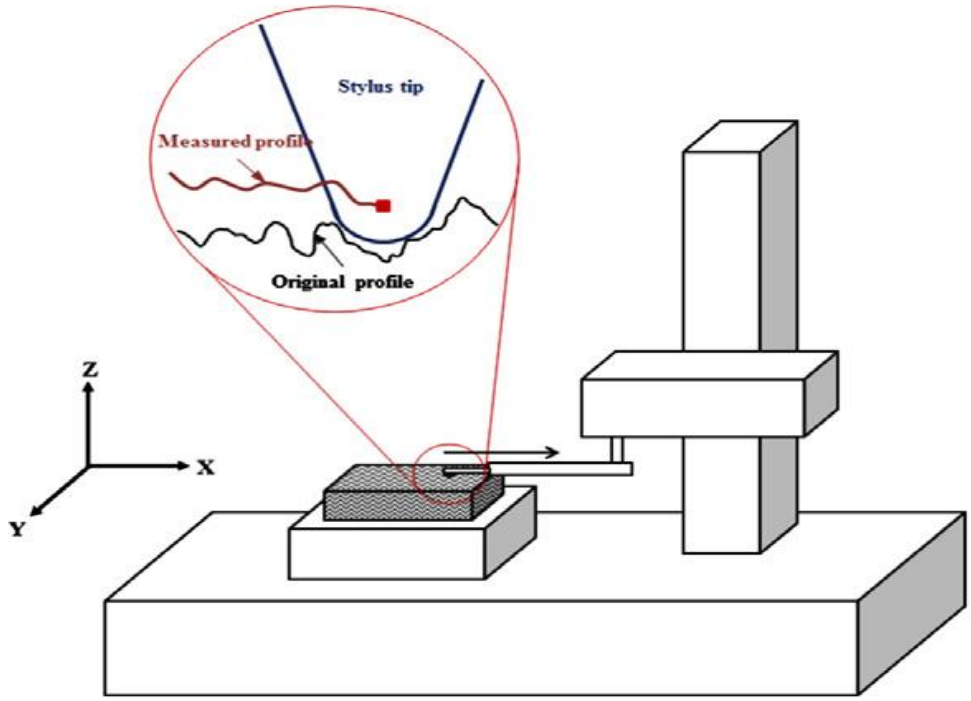

Figure 3. 14 Schematic representation stylus type profilometer [67].

This technique operates in a very simple way making use of the diamond stylus (needle) which runs over the surface. The thickness measurements are taken as the height of the profilometer needle changes at the step between the glass and the thin film and this height is recorded using capacitive transducer which gives profile of the surface.

3.4 Organic Solar Cell Device Characterization Technique

After successful fabrication of organic solar cell devices, it was vital to carryout electrical measurements to ascertain how effective is combination of various materials used to build a device for operation as a solar cell. Directly after depositing the top electrode we mounted the devices to the electrical probe of (J-V) system in the dust-free environment to avoid contamination. The device is placed gently onto the contact pad without sliding to avoid mechanical scratching that would cause shunts.

3.4.1 Current Voltage (J-V)

The current voltage measurement (J-V) method is a principal characterization technique that assists to determine the power conversion efficiency (PCE) of solar cells. It is an electrical technique which relies on the information provided by the characterization and measurements of electrical properties. They provide an insightful information about the quality of device fabricated. It is mainly used in the field of physics and electrical engineering to determine some basic parameters of different electrical devices.

3.4.1.1 IV Operating principle

The system used to carryout electrical measurements is Keithley 2400 source-measure unit, under simulated solar emission provided by a 1600W AAA NEWPORT solar simulator equipped with an AM1.5G filter, the sweeping speed was 0.25 mV ms^{-1}. The light intensity of solar simulator was calibrated with a reference diode from National Renewable Energy Laboratory (NREL) of the U.S Department of Energy which is certified with the spectral mismatch factor of 0.99. A schematic diagram showing general operating boundaries of the system is presented in Figure 3.17.

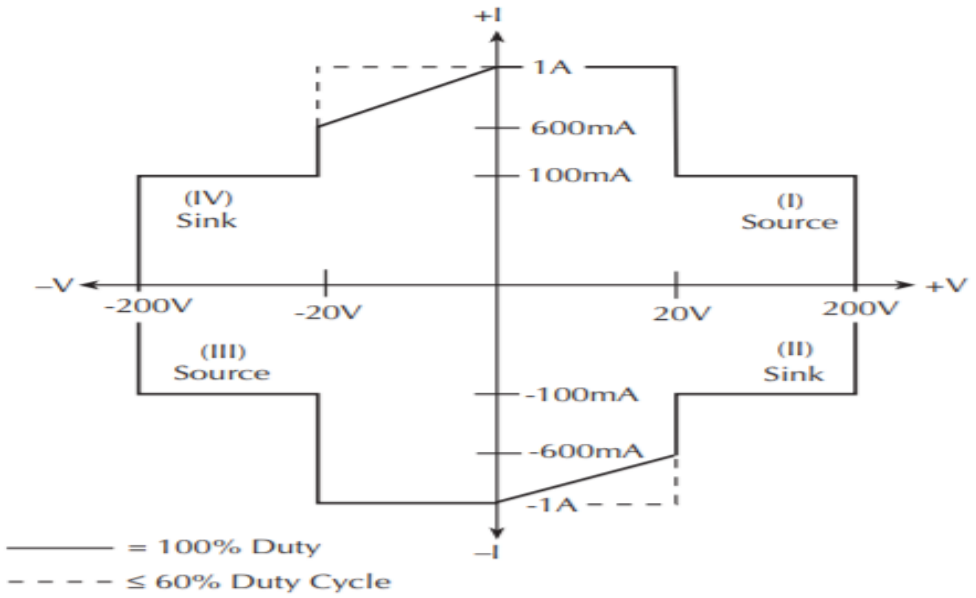

Figure 3. 15 Schematic diagram of Keithley 2400 operating boundaries [68].

The source meter instrument operates through four quadrants. The first and third quadrants holds the source which delivers power to a load whereas second and fourth quadrants contains a meant for dissipating power internally. When measuring current voltage characteristics of the cells, an external electric field is applied over the device while sweeping from reverse bias to the forward bias monitoring the current flow under illumination coming from solar simulator. The spectrum is presented where the change in extracted current is given as a function of the changing voltage. The resulting relationship is referred to as a current density-voltage (J-V) curve. PCE is determined from parameters that are measured by J-V curve using equation 2.1 presented in chapter 2.

3.5 References

[1] S. Shibata, K. Aoki, T. Yano and M. Yamane, Journal of solgel science and Technology,11, 279, (1998).

[2] J. Behari, Indian *J. Exp. Biol.* 48 (2010) 1008-1019.

[3] K. Norrman, A. Ghanbari-Siahkali and N.B. Larsen, *Annu. Rep. Prog. Chem., Sect.* C, 101 (2005) 174-201.

[4] D. Hanaor, G. Trianni, and C. Sorrell, *Surf. Coat. Tech.*, **205** (2011) 855-874.

[5] S. Middleman and A.K Hochberg, *Process Engineering Analysis in Semiconductor Devices Fabrication*, McGraw Hill, (1993) P. 313.

[6] M.S. Su, C.Y. Kuo, M.C. Yuan, U.S. Jeng, C.J Su. and K.H. Wei, *Adv. Mater.* 23 (2011) 3315-3319.

[7] R.G. Larson and T.J. Rehg, Spin Coating. In: Kistler S.F., Schweizer P.M. (eds) Liquid Film Coating. Springer, Dordrecht. (1997) 709-734.

[8] J.Y. Na, B. Kang, D.H. Sin, K. Cho and Y.D. Park, Understanding Solidification of Polythiophene Thin Films during Spin-Coating: Effects of Spin-Coating Time and Processing Additives.

[9] D.B. Mitzi, L.L. Kosbar, C.E. Murray, M. Copel, and A. Atzali, *Nature*, **428** (2004) 299-303.

[10] M.D. Tyona, A theoritical study on spin coating technique, *Advances in Materials Research*, **2** (2013) 195-208.

[11] N. Sahu, B. Parija and S. Panigrahi, Indian J. Phys. 83 (2009)493-502.

[12] J. Puetz and M.A. Aegerter (2004) Dip Coating Technique. In: M.A. Aegerter, M. Mennig (eds) Sol-Gel Technologies for Glass Producers and Users. Springer, Boston, MA.

[13] W. Geffcken and E. Berger, *Jenaer Glaswerk Schott & Gen., Jena* **736** (1939) 411.

[14] H. Dislich and P. Hinz, *J. Non-Cryst. Solids* **48** (1982) 11.

[15] D. Marongiu, PhD thesis, Università Degli Studi Di Milano-Bicocca, Dicembre 2010.

[16] S. Cyrus, MSc Thesis, Western Washington University (2017).

[17] P.J. Diemer , C.R. Lyle , Y. Mei , C. Sutton , M.M. Payne , J.E. Anthony , V. Coropceanu , J.-L. Brédas and O.D. Jurchescu , *Adv. Mater.*, 25 (2013) 6956 -6962.

[18] R. Ahmad, O.S. Wolfbeis, Y-B. Hahn, H.N. Alshareef, L. Torsi and K.N. Salama, *Materials Today Communications* (2018).

[19] E. Morteza and Z. Fatemeh, *Nanoscale Research Letters*, **10:462** (2015) 1-5.

[20] Y. Deng, E. Peng, Y. Shao, Z. Xiao, Q. Dong and J. Huang, *Energy Environ. Sci.* **8** (2015)1544-1550.

[21] Z. Yang, Z. Shasha, L. Lingbo and C. Wei, *J. Materiomics* **3** (2017) 231-244.

[22] R. Jenkins, and R.L. Snyder *John Wiley & Sons, N.Y* **138** (1996) 1-322.

[23] G. Crundwell, J. Phan, and K.A. Kantardjieff, *J. Chem. Ed.* **76 (**1999) 1242-1245.

[24] G. Cao *6th edition*, London (2004).

[25] R.J. Roe, Methods of X-ray and Neutron Scattering in Polymer Science, Oxford University Press, New York, 1999.

[26] N.S. Murthy, Recent developments in polymer characterization using X-ray diffraction, Rigaku J. **21** (2004) 15-24.

[27] K. Inaba, X-ray thin-film measurement technique, technical articles (31-01-2019).

[28] F. J. Balta, Calleja´, D. C. Bassett, and A. Keller, Polymer, 4, 269 (1963).

[29] M. Yasaka, X-ray thin-film measurement techniques V. X-ray reflectivity measurement, Technical articles, The Rigaku Journal, **26** (2010) 1-9.

[30] T. Mitsunaga, X-ray thin-film measurement techniques II. Out-of-plane diffraction measurements, Technical articles, **25** (2009) 7-12.

[31] S. Kobayashi, X-ray thin-film measurement techniques iV. Inplane XRD measurements, Technical articles, The Rigaku Journal, **26** (2010) 1-11.

[32] http://homepage.ntu.edu.tw/~kcyuan/form/For-Rigaku-Upload_thinfilm.pdf [Accessed: 06 February 2019].

[33] C.V. Stan, C.M. Beavers, M. Kunz and N. Tamura, X-ray Diffraction under Extreme Conditions at the Advanced Light Source, *Quantum Beam Sci.* **4** (2018) 1-33.

[34] F.V. Molefe, *MSc thesis*, University of the Free State, South Africa (2014).

[35] M.A. Prelas, G. Popouci and L.K. Bigelow CRC Press (1998).

[36] J. Qin et al. Advances in Raman spectroscopy and imaging techniques for quality and safety inspection of horticultural products, Postharvest Biology and Technology 149 (2019) 101-117.

[37] L.M. Malard, M.A. Pimenta, G. Dresselhaus, and M.S. Dresselhaus, *Physics Reports* **473** (2009) 51-87.

[38] A.C. Ferrari, J.C. Meyer, V. Scardaci, C. Casiraghi, M. Lazzeri, F. Mauri, S. Piscanec, D. Jiang, K. S. Novoselov, S. Roth, and A. K. Geim, *Phys. Rev. Lett.* **97** (2006).

[39] D.A. Skoog, F.J. Holler and S.R. Crouch, Principles of Instrumental Analysis, *6th edition* Thomson Brooks/Cole: Belmont, CA **351** (2007).

[40] H.H. Willard, Jr L.L. Meritt, J.J. Dean and Jr F.A. Settle, Instrumental methods of analysis. 7th ed. New Delhi: CBS Publisher & Distributors; 1988.

[41] Y.-H. Chiang, S.H. Wu, Y.-C. Kuo, H.-F. Chen, A. Chiou and O.K. Lee, Raman spectroscopy for grading of live osteosarcoma cells, Stem Cell Research & Therapy (2015) 6:81.

[42] J.M. Chalmers, H.G.M. Edwards and M.D. Hargreaves, Infrared and Raman spectroscopy in forensic science. 1st Ed. United Kingdom: John Wiley & Sons Ltd.; 2012.

[43] B.C. Smith, *Fundamentals of Fourier Transform Infrared Spectroscopy*. (2011).

[44] M. Naseska, FOURIER TRANSFORM INFRARED SPECTROSCOPY, Ljubljana, March 2016 http://mafija.fmf.uni-lj.si/seminar/files/2015_2016/FTIR_final_Naseska_Mimoza.pdf [Accessed 09 February 2019].

[45] D.L. Pavia, G.M. Lampman, and G.S. Kriz, *Introduction to Spectroscopy: a guide for students of organic chemistry*. (2009) 1979.

[46] O.M. Ntwaeaborwa, R.E. Kroon, H.C. Swart, Degradation of and energy transfer in oxide-based microscale and nanoscale phosphors doped with rare earth elements, PhD thesis, University of the Free State, Bloemfontein, South Africa, (2006).

[47] J. Shen, J. Liu, Y. Xing, H. Zhang, L. Luo and X. Jiang, *Journal of Analytical and Applied Pyrolysis* **133** (2018) 154-161.

[48] L.E. Amand and C.J. Tullin: The theory behind FTIR analysis, written documentation prepared for a distance course given by The Centre of Combustion Science and Technology, CECOST on ”Measurement Technology”, Lund, Sweden.

[49] J.I. Goldstein and H. Yakowits *Plenum Press*, London (1977).

[50] M. von Ardenne. Improvements in electron microscopes. GB 511204, convention date (Germany) 18 February 1937.

[51] A. Bogner, P.-H. Jouneau, G. Thollet, D. Basset and C. Gauthier, *Micron* **38** (2007) 390-401.

[52] S.J.B. Reed, Electron Microprobe analysis and scanning electron microscopy in geology, 2005, 2nd Ed, Cambridge Press, New York.

[53] K.P. Severin, Energy Dispersive Spectrometry of Common Rock Forming Minerals. Kluwer Academic Publishers, (2004) 225.

[54] J.I. Goldstein, D.E. Newbury, D.C. Joy, C.E. Lyman, P. Echlin, E. Lifshin, L. Sawyer, and J.R. Michael, Scanning electron microscopy and X-ray microanalysis. Third

Edition, Kluwer Academic / Plenum Publishers, New York Boston, Dordrecht, London, Moscow. (2003) 689 pages.

[55] T.M. Roane and I.L Pepper, Chapter 9 – Microscopic Techniques, Environmental Microbiology (Third Ed) (2015) 177-193.

[56] N.C. Thomas, *Journal of Chemical Education* **68** (1991) 631 – 634.

[57] G. Kortum, (1962) Kolorimetrie, Photometrie und Spektrometrie, Kap 1.5, 4. Aufl. Springer Berlin GOttingen Heidelberg, S 21 ff.

[58] N.H. Patel / Ph. D. Thesis / Sardar Patel University/ July−2015.

[59] Y. Cong, J. Zhang, F. Chen, and M. Anpo, *J. Phys. Chem. C* **111** (2007) 6976-6982.

[60] J.R. Lakowicz, Principles of Fluorescence Spectroscopy, 3rd ed.; Springer: New York, (2006).

[61] D. Jameson (2015) Keynote speech. FluoroFest. Cambridge, Ma.

[62] B. Valeur, Molecular Fluorescence: Principles and Applications; Wiley-VCH: Weinheim, (2002).

[63] K. Holliday, Inorganic Condensed Matter, Applications of Luminescence Spectroscopy, Encyclopedia of Spectroscopy and Spectrometry (Second Edition), (1999) 1057-1066.

[64] Horiba scientific, Handbook of spectroscopy, Introduction to Fluorescence, (2018) 133-155.

[65] K.K. Gupta, R.M. Kadam, N.S. Dhoble, S.P. Lochab, S.J. Dhoble, J. Lumin. 188 (2017) 81-95.

[66] J.-J. Park, K.-H. Kwon and N.-G. Cho, *Meas. Sci. Technol.* **17** (2006) 2380-2386.

[67] D.-H. Lee, 3-Dimensional profile distortion measured by stylus type surface profilometer, Measurement 46 (2013) 803-814.

[68] Keithley Model 2400 series Source Meter, User's Manual, Source-Measure Concepts 6-15 Accessed [18 March 2019].

Chapter 4: Spectroscopic Investigation of Charge and Energy Transfer in P3HT/GO Nanocomposite for Solar Cell Applications

4.1 Introduction

In the recent years, there has been a change in the energy landscape due to factors such as population increase and depletion of fossil fuels which has significantly increased the need for energy. The pursuit of sustainable energy sources revolves around renewable energy. According to scientists and engineers from various fields, nanotechnology may help society's efforts to address a number of its major energy-related issues. In the range of various carbon allotropes, graphene, which was experimentally found in 2004, is among the most promising nanomaterial for resolving the energy challenges [1]. Studies have been done to examine carbon nanostructures in particular after Manchester researchers won the Nobel Prize in 2010 for their discovery of graphene, verifying its significance in research and commercial applications [2]. Their quest has been driven by the remarkable qualities like charge transmission mechanical flexibility and high optical transparency [3]. Additionally, substantial research has been done on two of graphene's amazing derivatives which are graphene oxide (GO) and reduced graphene oxide (rGO) [1,2]. These nanomaterials can be produced from graphite, which was discovered to be a precursor for carbon nanostructures [6]. This opens the door to the possibility of producing graphene-based products on a big scale at low cost. The production of composite materials based on graphene for a variety of purposes is made selectively possible for applications in sectors such as optoelectronic devices [3], biological imaging [7] and energy storage in supercapacitors [8].

In recent times, multiple processes have been developed for creating GO nanocomposites which involve microwave [9], hydrothermal [10], sol-gel [11] and Hummers method [12] among others. The majority of these processes require a reactive oxygen background, which is essential for regulating the thin film quality. The Hummer's method stands out as a multi-step chemical process that requires (i) pre-intercalation, (ii) intercalation, (iii) oxidation and (iv) reduction chemistry. In terms of high yield and cost effectiveness, this top-down strategy is now the most practical. Moreover, it enhances the dispersion stability of the resultant GO and is environmentally friendly, with no surface flaws [13].

The vital component of solar cell devices in terms of the efficiency is the transparent electrode in the front panel. The widely used metal oxide for transparent electrodes is indium

tin oxide (ITO) due to its low resistance and high optical transmission characteristics in the visible spectral range [14]. Thus, it is important to note that ITO will not serve the purpose of flexibility because it is costly to manufacture and it is naturally brittle. The most promising nanomaterial to serve flexibility purpose is GO with adequate catalytic activity that can successfully replace ITO. In the study conducted by Koh *et al.* [15], they have discovered the comparable performance when monolayer graphene is used in place of ITO in organic solar cells. In their quest, they utilized P3HT as electron donor to functionalize GO by generating nanocomposite material. In this regard, P3HT because of its considerable electron delocalization along the molecular backbone provides thiophene derivatives that are well known for having large hole mobility. In light of this, P3HT/GO nanocomposite material with greater charge carrier mobility promises to enhance device performance. [12].

In solar cells, GO have been exploited as a novel class of effective materials for hole and electron extraction. The development of nanocomposites with GO acting as an electron acceptor and P3HT acting as an electron donor is likely to simplify charge transport for the developing field of solar technology. Sriram *et al.* [16] obtained ~ 407 nm emission at which originated from the interaction between GO and P3HT. The 610 nm emission for P3HT, which has never been reported before, and the switch to 600 nm emission for the P3HT/GO nanocomposite are what make this work unique. The additional emissions we saw indicate the emergence of new energy levels, and the quenching of the emissions we saw after the formation of the P3HT/GO nanocomposite is a desired attribute in photovoltaics.

In the research conducted here, P3HT and P3HT/GO thin film nanocomposite were grown using drop casting method on the glass substrate. A comparative study on grown P3HT and P3HT/GO thin film nanocomposites was undertaken to reveal strength of bilayer structure. The spectroscopic techniques helped to shed light on the functionalization and chemical interactions at the interface of P3HT/GO thin film nanocomposite. The primary goal is to examine the charge transfer characteristics of a donor (P3HT) to the acceptor (GO).

4.2 Experimental

4.2.1 Chemicals information

The chlorobenzene (CB anhydrous, 99.8%) natural graphite powder (G ≥ 99.5%) and regioregular poly (3-hexylthiophene-2,5-diyl) (rr-P3HT > 99%) were obtained from Sigma-Aldrich, Modderfontein Gauteng, South Africa and they were utilized without being purified.

4.2.2 Materials preparation

The chemical structure of P3HT and GO are presented in Figure 4.1. We adapted the modified Hummers method created by Khenfouch *et al.* to prepare the GO nanosheets [17]. We produced poly(3-hexylthiophene) P3HT, which aids in the creation of single or few-layer graphene sheets, to avoid GO restacking and aggregation. To create a solution with a 5% concentration, the P3HT was dispersed in chlorobenzene. The solution was stirred for 10 minutes in a closed vial to maintain a constant temperature of 80 ℃ on a magnetic hot plate. The temperature was reduced to 50 ℃ while constantly stirring the solution for 60 min and the solution was left to cool at room temperature. In preparation for thin film deposition, we cleaned the substrates sequentially using acetone, ethanol and DI water inside an ultrasonic bath and dried them in an oven at 50 ℃. The obtained solution of GO and P3HT were coated on the glass substrates. Following coating, any remaining solvents were removed by drying the P3HT and P3HT/GO thin films for two hours at 50 °C.

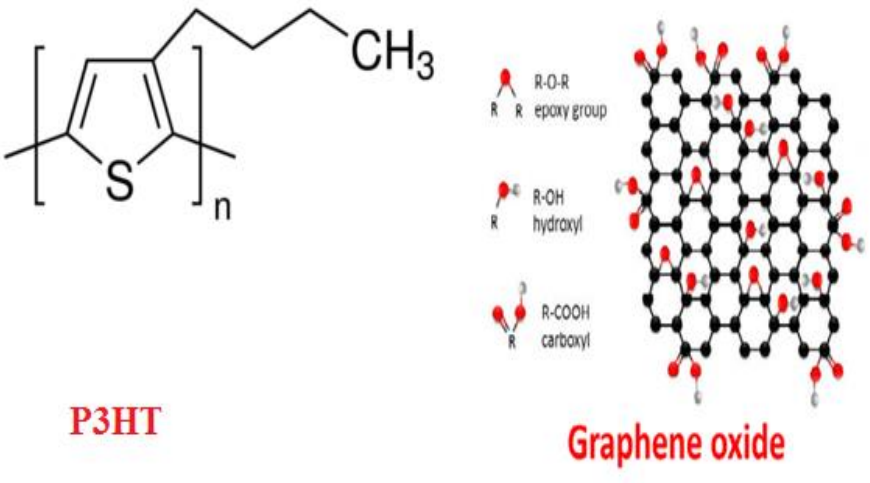

Figure 4. 1 The chemical structures of P3HT [18] and GO [19] nanomaterials used to grow thin films.

4.2.3 Nanocomposites characterizations

The crystalline phases of P3HT and GO/P3HT thin film composites were identified using Rigaku Smart Lab diffractometer with CuKα (1.5418Å) radiation. The surface morphology of the P3HT and GO/P3HT thin film composites were analysed using a Shimadzu model ZU SSX-550 Superscan SEM. The FTIR spectra acquisition was conducted using a PerkinElmer spectrometer in the scan range 400 to 4000 cm^{-1}. The optical studies were conducted in the wavelength range 200 - 900 nm using a (PerkinElmer Lambda 1050 UV/VIS/NIR Lambda) spectrometer in the absorbance mode. The solid-state measurements were acquired using a tunable-photoluminescence (PL) system.

4.3 Results and discussion

4.3.1 XRD analysis

Figure 4.2 shows the XRD structure of P3HT and P3HT/GO thin film nanocomposites. The P3HT spectrum resembles a narrow peak at 2θ = 6.65° which is assigned to (100) reflection which denotes crystalline phase of the polymer.

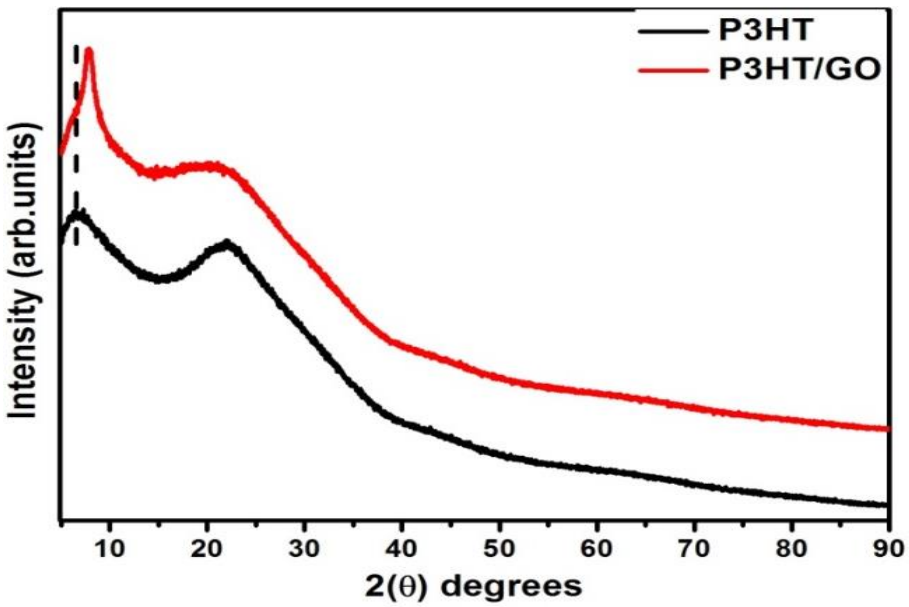

Figure 4. 2 The XRD patterns of the P3HT and P3HT/GO thin film nanocomposites.

4.3.2 SEM analysis

Moreover, a broader peak is apparent at ~ 2θ = 22.08° and is symbolic of the amorphous nature of P3HT. The diffraction spectrum of P3HT/GO thin film nanocomposite reveals the diffraction peaks witnessed in pristine P3HT as evidence that the lamellae of P3HT chains

adopt an "edge-on" orientation upon bonding at the interface. The nanocomposite's (100) orientation shows a change to a greater diffraction angle, mostly caused by a reduction in lattice spacing. Stylianakis *et al.* [20] witnessed similar behaviour and attributed diffraction peak shifting to the change in interplanar spacing due to restacking of functionalized GO sheets. The GO distinctive peak was seen at 2θ = 8° in contrast to its typical position, which is between 10° - 11°. The broader diffraction peak in the 2θ range 20 - 40° for both thin films denote that each of the stacked sheets is exfoliated into a nanosheet [12]. There were no additional peaks corresponding to the impurities or P3HT backbone.

The morphological study on grown P3HT and P3HT/GO thin film nanocomposites were probed using SEM and the acquired images are presented in Figure 4.3. From Figure 4.3 (a), we see clusters of flower-like nanostructures and some tiny oval particles lying on top of the flower-like structures. We noticed morphological change when growing P3HT onto GO thin film. In Figure 4.3 (b) we have the morphology that mimics flaky tree leaves and has wrinkled and crinkly appearance. The flaky nanostructure denotes distribution of GO layers within the polymer matrix. We propose that close contact between the basal plane of GO and P3HT is the cause of the observed alteration in surface morphology. The π-orbitals of the thiophene ring and the π-orbitals of the graphene are said to be responsible for the interface interaction [21].

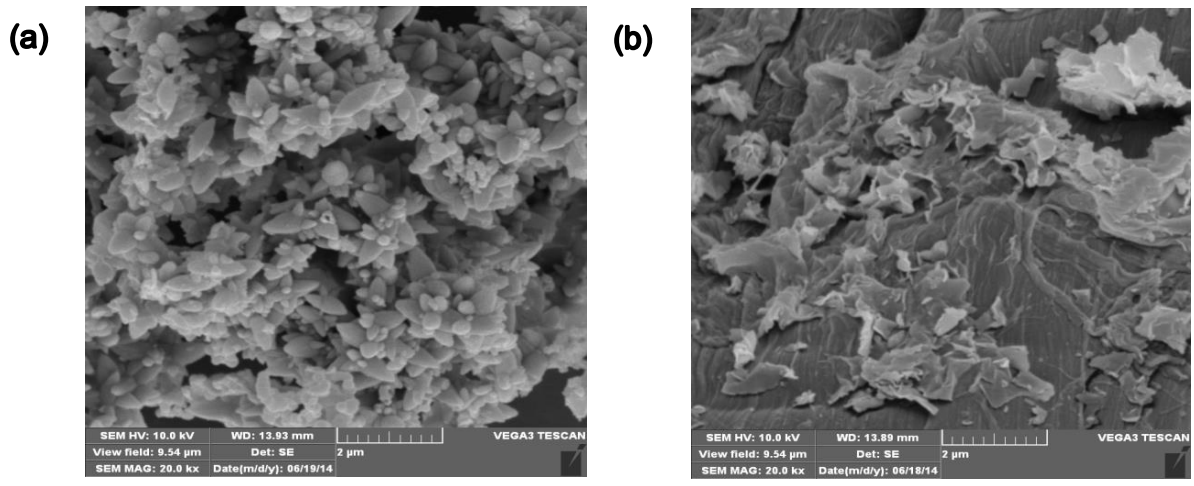

Figure 4. 3 The SEM images of (a) P3HT and (b) P3HT/GO thin film nanocomposites.

4.3.3 FTIR analysis

The FTIR spectra in Figure 4.4. is acquired in transmission mode to analyse the bonding interactions and the linkage between P3HT/GO thin film nanocomposites.

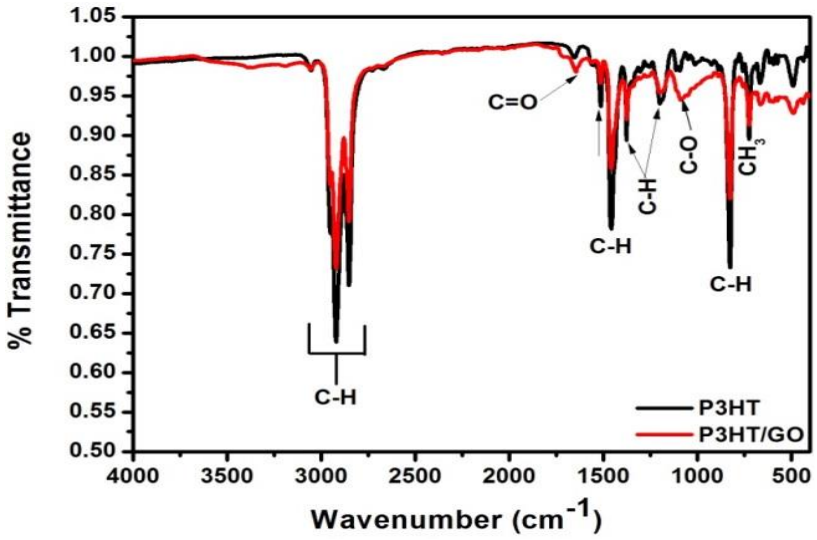

Figure 4. 4 FTIR spectra of P3HT and P3HT/GO thin film nanocomposites.

The P3HT spectra is dominated by three distinctive bands at positions ~ 2960, ~ 2925, and ~ 2855 cm^{-1} which originates from aliphatic C-H stretching mode of P3HT alongside the 821 cm^{-1} band which denote the aromatic C-H bending [22]. At ~ 1456 cm-1, the bending vibration of the C-H bond was noticed. The low intensity vibration bands of GO were populated at regions ~ 3372, ~ 3194 and ~ 1081 cm^{-1}. The stretching vibrations are responsible for the C-O bond at ~ 1081 cm^{-1}, which verifies the presence of functional oxide groups following oxidation [23]. From P3HT/GO thin film nanocomposite spectrum we saw a band at ~ 1648 cm^{-1} that resembles the amide I vibrational stretch (ν(C=O)) [24]. The results show that the interaction between GO and P3HT results in the derivatization of both the surface hydroxyl and carboxyl functional groups via the production of amides [23]. At 721 cm^{-1}, we found a band corresponding to the methyl rock mode and the CH_3 rocking vibration. The detected 1378 cm^{-1} C-H vibration band may result from thiophene's partial breakdown [25]. It is significant to note that the vibrational frequencies seen in P3HT are also present in P3HT/GO, but their relative intensity dropped following interaction with GO. The reduction in intensity is probably brought on by oxygenation when P3HT interacts with GO.

4.3.4 UV-vis analysis

For a deeper understanding of absorption behaviour on P3HT and P3HT/GO thin films, the optical absorbance measurements were carried out as shown in Figure 4.5. From the UV-Vis spectrum of pristine P3HT, it is evident that the polymer has an absorption at ~ 490 nm which resembles π-π^* transition [26].

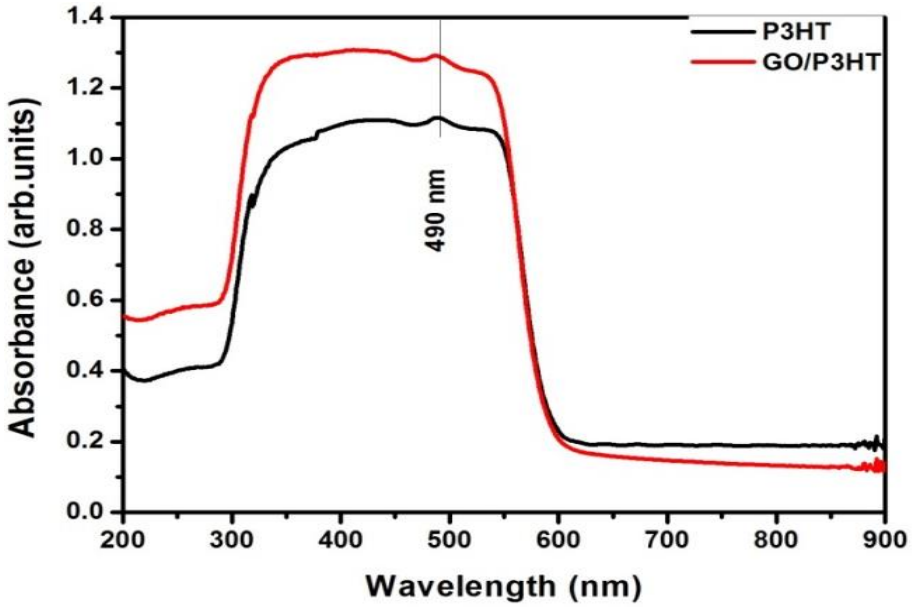

Figure 4. 5 Absorption spectra of P3HT and P3HT/GO thin film nanocomposites.

The P3HT/GO thin film nanocomposite has a broader and stronger absorption in comparison to pure P3HT. The change in absorption characteristics is indicative of the contribution that originates from GO in the optical absorption of P3HT/GO thin film nanocomposite. This may possibly be as a result of the chain segments in the amorphous P3HT having shorter effective conjugation lengths, which more closely localize the exciton wave function and raise its energy [27]. The interaction at the interface of P3HT/GO thin film nanocomposite is linked to inter-chain order (rise in P3HT chains disorder), which improves nanocomposite absorption [28]. This elucidate on the charge transfer from the donor polymer to the acceptor carbon-based GO.

4.3.5 Photoluminescence analysis

In Figure 4.6 (a) we have the emission spectra of P3HT and P3HT/GO thin films acquired at different excitations. Figure 4.6 (b) presents the contour map that is an array of emission spectra collected at various excitation levels, where the luminescence intensity depends on the excitation and emission wavelengths. We noticed gradual decrease in emission for both P3HT and P3HT/GO thin film nanocomposite as the excitation wavelength was increased. This phenomenon shows that the excitation wavelength influences emission intensity in a comparable manner. We assume that charge transfer based on excitation is what is responsible for the emission intensity quenching in P3HT and P3HT/GO thin film nanocomposite.

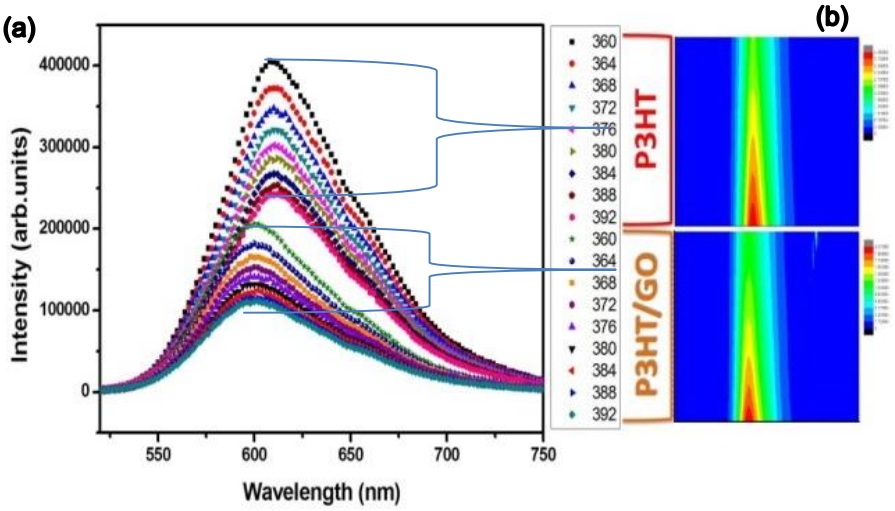

Figure 4. 6 PL emission spectra, (b) contour maps of P3HT and P3HT/GO thin film nanocomposites excited at different wavelengths.

Upon exciting at a wavelength of 360 nm, we obtained a strong fluorescence emission peaking at ~ 610 nm. In general, the P3HT emission is said to originate from defect states upon radiative recombination of polaron-exciton pairs into Franck-Condon states [29]. The luminescence emission of P3HT is remarkably diminished by growing GO with P3HT indicative of charge transfer taking place at the interface of P3HT/GO thin film nanocomposite. This is primarily caused by increased electrostatic attraction between the backbones of P3HT and GO, which changes the planarity of the P3HT [29]. Moreover, the intensity decrease is linked to GO which confines the photoemission following electron transfer from P3HT to the GO as a result of exciton dissociation. The variations in intensity takes place due to alteration in defect density. Zheng *et al.* [30] assigned the intensity decrease to weakening of the interchain connections of P3HT when incorporating GO sheets, indicating that P3HT/GO thin film nanocomposite has a substantial hetero interface. Similar intensity decrease has been reported by Bkakri *et al.* [31] using energy level diagram of P3HT:Graphene thin film nanocomposite depicting charge transfer mechanism. The observed correlation puts GO as suitable nanomaterial to serve as electron acceptor in photovoltaic devices. Contrary to our observation, Saini *et al.* [29] witnessed the enhancement in fluorescence emission embedding GO in the nanocomposite. Contrary to pristine P3HT thin film, the peak position of P3HT/GO thin film nanocomposite was blue shifted to ~ 600 nm at different excitations in the order 360 – 392 nm. The blue shift is believed to be caused by an increment in structural disorder of the polymer as witnessed in the UV-vis results [32]. By citing the previous work on P3HT irradiated with Ni ion, this blue shift shows the decreased conjugation length due to change in polymer conformation [33].

The observed slight blue shift for P3HT/GO compared to pristine P3HT can be attributed to increased percentage of short segments over long segments in the matrix owing to the interface interaction of the nanocomposites [34 - 35]. The transition from blue to red in the contour map indicates an increase in luminescence intensity. The extent to which the thin film nanomaterials were highly emissive is shown by the red area. The most intense region depicted by red colour reveals a shift to the shorter wavelength for thin film nanocomposite contrary to pristine P3HT.

Table 4.1 Comparative study between PL dynamics of P3HT and P3HT/GO thin film nanocomposites from the literature [29] and studies conducted here.

	Literature	**Current work**
	λ_{EM} **(nm)**	λ_{EM} **(nm)**
P3HT	650 and 688	610
P3HT/GO	650 and 688	600

Table 4.1 compares the emission spectra of P3HT and P3HT/GO thin film nanocomposites in the current investigation to those reported in other studies. Bkakri *et al.* [31], acquired an emission spectrum using 488 nm excitation that falls within absorption of P3HT in the absorbance measurements. They attained two fluorescence maxima at 650 and 688 nm, respectively. Following the addition of graphene, the observed emission bands were quenched. The PL intensity quenching was attributed to the transfer of electrons from P3HT to graphene because there were no extra spectral characteristics compared to those of P3HT. In our results the emission of P3HT and P3HT/GO thin film nanocomposite was obtained at various excitations taken from strong absorption presented in Figure 4.5. From pristine P3HT thin film, we obtained maximum emission at ~ 610 nm which is then confined by creating P3HT/GO thin film nanocomposite. Additionally, the emission spectra of P3HT/GO thin nanocomposite is blue shifted to ~ 600 nm. It is generally known that the wavelength in PL corresponds to the energy locations of the triplet state with respect to the ground state [31]. Thus, the change in peak position to the shorter wavelength leads to widening of the energy gap between the ground singlet state and the lowest triplet state. Therefore, the witnessed blue shift may be responsible for P3HT structural irregularity, i.e. the interaction at the interface of P3HT/GO minimizes the lattice deformation leading to the reduction of emission

intensity. This is consistent with SEM findings where we observed morphological alteration to nanoflakes for P3HT/GO thin film nanocomposite

4.4 Conclusion

The study conducted here focused on the growth of GO and P3HT thin films using chemically prepared nanomaterials. The interaction among GO and P3HT thin films was conducted using various spectroscopic techniques. The existence of groups containing oxygen confirmed by FTIR corroborated the significant interaction between GO and P3HT thin films. The increase in absorption spectrum demonstrated the π-π interaction between P3HT and GO thin films. Furthermore, the PL findings demonstrated that GO restricts the photoemission of P3HT, causing emission quenching. This interaction between P3HT and GO is indicative of the transpired superior charge transfer at the interface. The work generally offers guidance on coating multilayer thin film structures for photovoltaic applications.

4.5 References

[1] Novoselov, K. S.; Geim, A. K.; Morozov, S. V.; Jiang, D.; Zhang, Y.; Dubonos, S. V.; Grigorieva, I. V.; Firsov, A. A.; *Science*, **2004**, *306*, 666–669.

[2] Enoki, T.; *Carbon* **2011**, *49*, 2579.

[3] Lim, T. Kim, C. S.; Song, M.; Ryu, S. Y.; Ju, S.; *Synth. Met.* **2015**, *205*, 1–5.

[4] Zhu, Y.; Murali, S.; Cai, W.; Li, X.; Suk, J.; Potts, W. J. R.; Ruoff, R. S.; *Adv. Mater.* **2010**, *22*, 3906–3924.

[5] Chua C. K.; Pumera, M.; *Chem. Soc. Rev.* **2014**, *43*, 291–312.

[6] Li, B.; Nan, Y.; Zhang, P.; Wang, Z.; Lu, Q.; Song X.; *Diamond Relat. Mater.* **2015**, *55*, 87-94.

[7] Misra, S. K.; Pandey, H.; Misra, S. K.; *Int. J. Adv. Pharm.* **2013**, *2*, 1–4.

[8] Zang, X.; Li, X.; Zhu, M.; Li, X.; Zhen, Z.; He, Y.; Wang, K.; Wei, J.; Kang, F.; Zhu, H.; *Nanoscale* **201**5, *7*, 7318–7322.

[9] Kim, N.; Xin, G.; Cho, S. M.; Pang, C.; Chae, H.; Curr. *Appl. Phys.* **2015**, *15*, 953–957.

[10] Zhu, M.; Li, X.; Liu, W.; Cui, Y.; *J. Power Sources* **2014**, *262*, 349–355.

[11] Hintze,C.; Morita, K.; Riedel, R.; Ionescu, E.; Mera, G.; *J. Eur. Ceram. Soc.* **2016**, *36*, 2923–2930.

[12] Obreja, A. C.; Cristea, D.; Gavrila, R.; Schiopu, V.; Dinescu, A.; Danila, M.; Comanescu, F. *Appl. Surf. Sci.* **2013**, *276*, 458–467.

[13] Song, J.; Wang, X.; Chang, C. *Journal of Nanomaterials* **2014**, 1–6.

[14] Farhan, M. S.; Zalnezhad, E.; Bushroa, A. R.; Sarhan, A. A. D.; *Int. J. Precis. Eng. Manuf.* **2013**, *14*, 1465–1469.

[15] Koh,W. S.; Gan, C. H.; Phua, W. K.; Akimov, Y. A.; Bai, P.; IEEE J. Sel. Top. Quantum Electron. **2014**, *20*, 1–8.

[16] Sriram, P.; Nutenki, R.; Mandapati, V. R.; Karuppiah, M.; Kattimuttathu, S. I.; *Polym. Compos.* 2015, 1–11.

[17] Khenfouch, M.; Buttner, U.; Baitoul, M.; Maaza, M.; *Graphene* **3** (2014) 7-13.

[18] Omer, B.M.; *J. Nano- Electron. Phys.* **5** (2013) 1-67.

[19] Chiu N.F.; Huang, T.Y.; Lai, H.C.; Graphene oxide based surface Plasmon resonance biosensors, in: M. Aliofkhazraei (Ed.). Advances in Graphene Science. *InTech, Rijeka*. **8** (2013).

[20] Stylianakis, M. M.; Stratakis, E.; Koudoumas, E.; Kymakis, E.; Anastasiadis, S. H.; *ACS Appl. Mater. Interfaces* **2012**, *4*, 4864–4870.

[21] Iguchi, H.; Miyahara, K.; Higashi, C.; Fujita, K.; Nakagawa, N.; Tamba, S.; Mori, A.; Yoshitani, H.; Nakasuga, A.; Maruyama, T.; *FlatChem* **8** (2018) 31-39.

[22] Yu, D.; Yang, S. Y.; Durstock, M.; Baek, J. B.; Dai, L. M. *ACS Nano*, **2010**, *4*, 5633–5640.

[23] Ban, F. Y.; Majid, S. R.; Huang, N. M.; Lim , H. N.; *Int. J. Electrochem. Sci.* **2012**, *7*, 4345–4351.

[24] Romero-Borja, D.; Maldonado, J.-L.; Barbosa-García, O.; Rodríguez, M.; Pérez-Gutiérrez, E.; Fuentes-Ramírez, R.; de la Rosa, G.; *Synth. Met.* **2015**, *200*, 91–98.

[25] Kovacik, P.; College, O.; "Vacuum Deposition of organic molecules." PhD thesis University of Oxford.

[26] Shrotriya, V.; Ouyang, J.; Tseng, R. J.; Li, G.; Yang, Y.; *Chem. Phys. Lett.*, **2005**, *411*, 138–143.

[27] Brown, P. J.; Thomas, D.; Köhler, Wilson, A. J.; Kim, J.-S.; Ramsdale, C. Sirringhaus, H.; Friend, R.; *Phys. Rev. B* **2003** *67*, 1–16.

[28] Arranz-Andrés, J.; Blau, W. J.; *Carbon N. Y.* **2008**, *46*, 2067–2075.

[29] Saini, V.; Abdulrazzaq, O.; Bourdo, Dervishi,S. E.; Petre, A.; Bairi, V. G.; Mustafa, T.; Schnackenberg, L.; Viswanathan, T.; Biris, A. S.; *J. Appl. Phys.* **2012**, *112*, 054327.

[30] Zheng, F.; Xu, W.-L.; Jin, H.-D.; Hao, X.-T.; Ghiggino, K. P; *RSC Adv.*, **2015**, *5*, 89515.

[31] Bkakri, R.; Kusmartseva, O. E.; Kusmartsev, F. V.; Song, M.; A. Bouazizi.; *J. Lumin.* **2015**, *161*, 264-270.

[32] Jung, K. Y.; Bin Park, S.; Anpo, M.; *J. Photochem. Photobiol. A Chem.* **2005**, *170*, 247–252.

[33] Sharma, T.; Singhal, R.; Vishnoi, R.; Lakshmi, G.B.V.S.; Chand, S.; Avasthi, D.K.; Kanjilal, A.; Biswas, S.K. *Vacuum* **135** (2017) 73-85.

[34] Baghgar, M.; Labastide, J.A.; Bokel, F.; Hayward, R.C.; Barnes, M.D.; *J. Phys. Chem. C* **118** (2014) 2229-2235.

[35] Khenfouch, M.; Bajjou, O.; Baitoul, M.; Maaza, M.; *Opt. Mater.* **42** (2015) 479-483.

Chapter 5: Growth and Characterization of Hybrid (HoGO/P3HT) Graphene-Based Nanostructures for Photovoltaic Applications

5.1 Introduction

In-depth scientific research on renewable energy sources that can displace traditional fossil fuels has been conducted for a very long time. There is a growing need for renewable and ecologically acceptable energy sources. This has led to the development and testing of numerous types of photovoltaic cells, including those made of silicon, organic dyes, conducting polymers, graphene, and the hybrid cells [1]. When addressing global energy crisis, hybrid organic-inorganic thin film nanostructures, particularly organic semiconductors, are of interest. Organic conducting polymers are one of the materials of interest in the class of hybrid nanostructures because they have intriguing chemical structures.

Due to their remarkable optoelectronic capabilities and ease of preparation from solutions on a wide scale, semiconducting polymers have attracted considerable interest. The most adaptable polymer semiconductors being studied for many applications, including field-effect transistors, supercapacitors, and solar cells are polythiophenes, particularly poly (3-hexylthiophene) (P3HT) [2, 3]. Studies have demonstrated that modifying these polymers' surface morphologies with a functional layer of nanoparticles has a considerable impact on the effectiveness of manufactured devices [4]. However, because of the intricate semi-crystalline microstructure, which is made up of crystalline and amorphous domains, determining charge mobility continues to be difficult. Making use of novel nanomaterials with vast surface areas as active components is one strategy to enhance charge mobility. The nanomaterial of choice in this situation is graphene and its derivatives, whose substantial surface area might be employed to accept transferred charges. The conducting polymers and graphene have previously been produced separately and combined in a solution to create composite nanostructures [5, 6]. However, the performance of photovoltaic devices was fairly low due to the re-stacking property of graphene oxide layers. To improve the charge transport properties, we created HoGO nanocomposite by combining GO with holmium (Ho).

Holmium fall under the group of rare earth ions known as lanthanide, it has a number of intriguing characteristics, including strong magnetic moments and luminescence. The latter is demonstrated in photostable up-conversion nanoparticles, from which the transfer of energy amongst two elements (for example, erbium and ytterbium) results in multicolor

luminescence [7]. Because of the peculiar configuration of 4f electrons in Ho, it belongs to a class of elements having distinctive catalytic, magnetic and optical properties. It has one of the highest magnetic moments of any element, however, we are more interested in its spectroscopic properties. The addition of Ho ions into a host matrix by concept of doping can exhibit outstanding properties. This indicates that it can significantly reduce the charge recombination of photoinduced electrons and holes in semiconductors and increase photocatalytic activity and photosensitivity.

In this work, we discuss the effect of incorporating Ho as a dopant into GO for the formation of HoGO nanocomposite. The generated HoGO nanocomposite is then utilized as HoGO/P3HT thin film to be applied in optoelectronic devices for solar energy harnessing. The performance of grown HoGO/P3HT thin film nanocomposite is extensively investigated using structural, morphological and optical techniques to verify functionalization and interface interaction. The obtained results in this study shows that Ho in Go exhibit improvement in optical properties as those of ZnO doped with Ho for photovoltaic devices.

5.2 Experimental

5.2.1 Preparation and thin film growth using GO, Ho and P3HT

The method used to prepare P3HT for experimentation is similar to that described in our previous chapter [8]. We have used the modified Hummers method described by Khenfouch *et al*. for the synthesis of GO [9]. Prior to preparing holmium solution, we prepared sodium hydroxide (NaOH) solution by adding 0.1 g of NaOH in 50 ml of distilled water and we continuously stirred the solution for 10 min for complete dissolution of NaOH. Then, a 0.5 g of holmium (III) Nitrate ($Ho(NO_3)_3$) was added into 40 ml of distilled water and stirred for 30 min. Thereafter, 10 ml of the NaOH solution was added to 40 ml of the $Ho(NO_3)_3$ inside a china dish followed by heating at 90 °C for 24 hours in an oven. The solutions were mixed in a 1:1 Ho:GO molar ratio and ultrasonically agitated for 30 min to create the inclusion complex for the HoGO nanocomposite. The 1.2 x 1.2 cm^2 ITO substrates were used for thin film deposition and they were cleaned sequentially in DI water, ethanol and acetone for 15 min before deposition. To avoid polymer pre-aggregation and solution gelation, the P3HT solution was pre-heated at 50 °C for 15 min before coating [10]. Drop casting method was used to deposit thin film nanostructures onto the ITO substrates. Thin film nanostructures were dried in an oven at 50 °C for two hours right after deposition to get rid of any residue.

5.2.2 Thin films characterization

The purity and phase of created thin film nanostructures were acquired by X-ray diffraction technique in reflection mode (Bragg-Brentano geometry) utilizing a Rigaku Smart Lab diffractometer coupled with CuKα (1.5418Å) radiation. The surface morphology analysis was probed using the Field Emission Scanning Electron Microscope (FE-SEM) model (Shimadzu ZU SSX-550 Superscan). The stretching vibration alteration and formation of chemical bonds were studied in the scan range 400 to 4000 cm^{-1} by FTIR model PerkinElmer spectrometer. The absorbance studies on the thin-films were conducted in the range 250 - 800 nm using PerkinElmer spectrometer model 1050 UV/VIS/NIR Lambda coupled with an integrating sphere.

5.3 Results and discussion

5.3.1 XRD analysis

Figure 5.1 shows the XRD patterns of P3HT, HoGO and HoGO/P3HT layered nanostructures. The spectrum of pristine P3HT presents an amorphous basis of the polymer dominated by (100) peak at ~ 5.7°, which conform with XRD results of P3HT reported elsewhere [8]. Moreover, the spectrum has the ITO peaks denoted with asterisk (*) at 2θ positions ~ 21.5°, ~ 30.5° and 35.4°. From the HoGO nanocomposite, we observed the Ho peak marked with (#) at 2θ ~ 9.91° to confirm its presence in addition to ITO peaks.

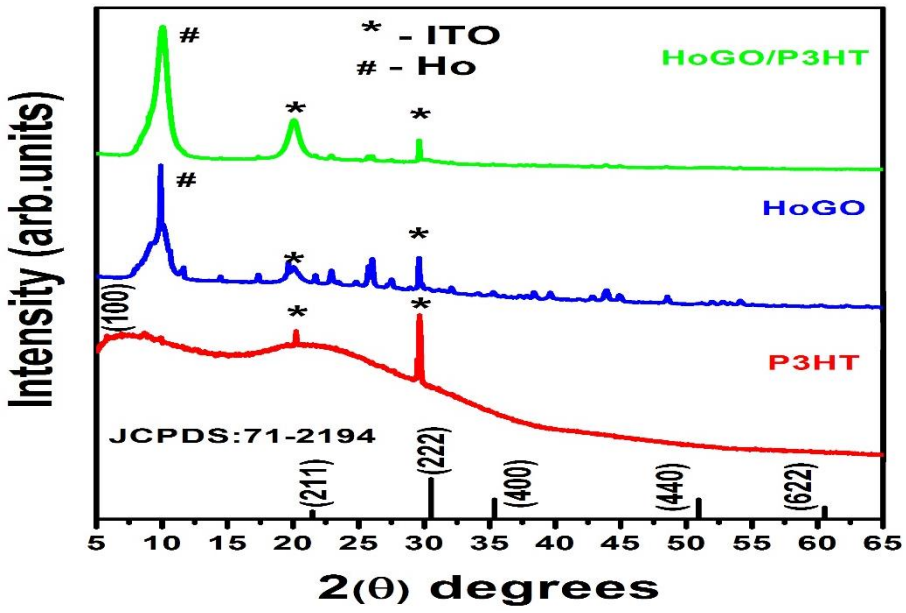

Figure 5. 1 XRD spectra of P3HT, HoGO and HoGO/P3HT layered nanostructures.

For the HoGO/P3HT layered nanostructure, the Ho diffraction patterns were broadened and ITO peaks are pronounced showing the reduction in crystallinity of the nanocomposite. According to the report by Zhao *et al.* [11], crystallization of P3HT is hindered by the crystalline entities upon interaction with other nanomaterials which causes less ordering of polymer moieties. In the multi-layered nanostructures, the GO peaks were masked by highly intense diffractions coming from Ho and glass substrate.

5.3.2 SEM analysis

Figure 5.2 (a) presents the agglomerates of small spherical nanoparticles for P3HT layered nanostructures. The results show that the nanoparticle distribution in relation to the substrate is not uniform as there are chunks of nanoparticles and some islands between them. The non-uniform morphology is caused by sensitivity of polymer to the thin film thickness [12].

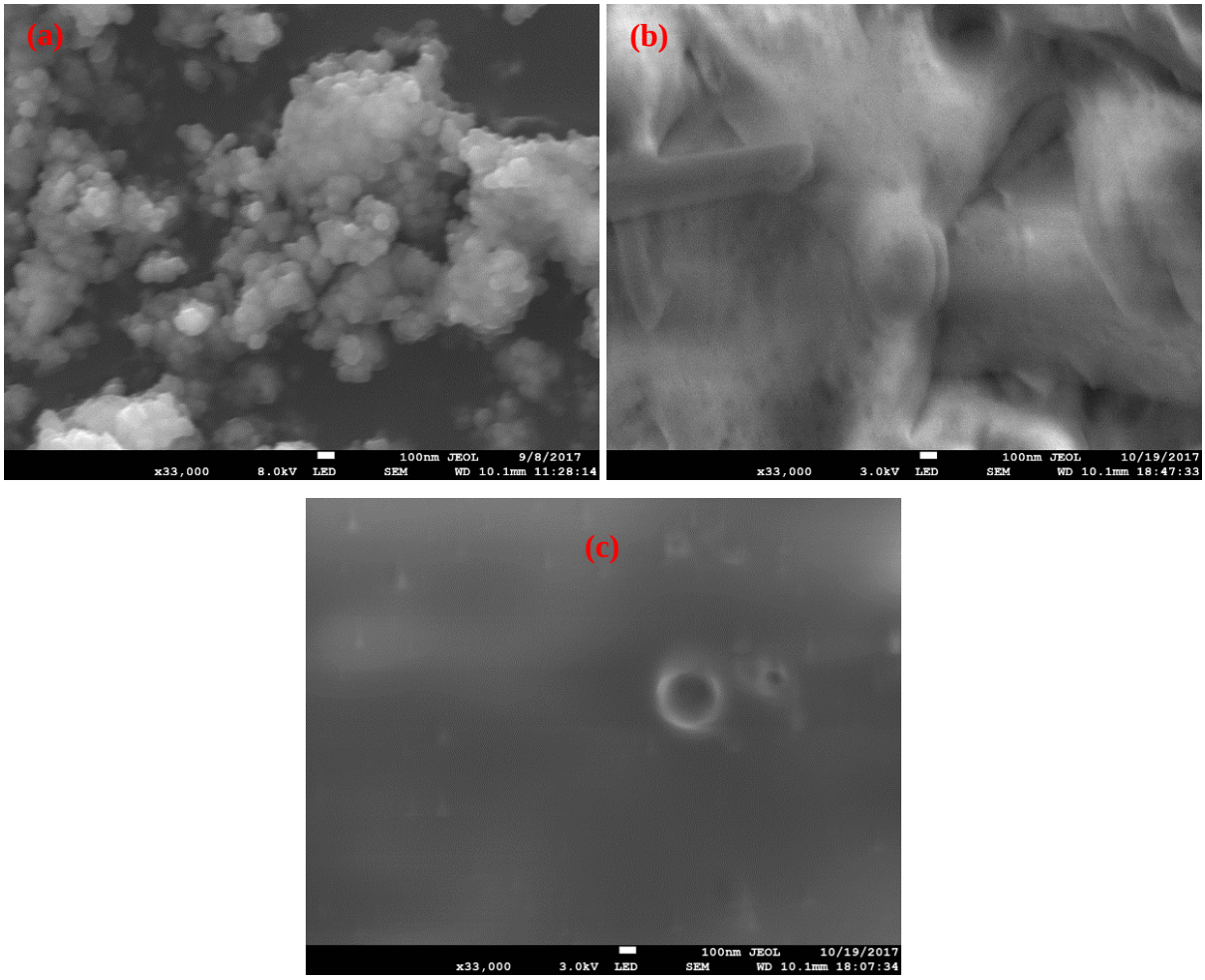

Figure 5. 2 SEM images of (a) P3HT, (b) HoGO and (c) HoGO/P3HT layered nanostructures.

The agglomeration of particles indicates the orientation and distribution of π-stacked aggregates inside an amorphous matrix of the polymer. Numerous investigations have indicated that the molecular weight, regioregularity, and polydispersity of regioregular P3HT have a significant impact on its surface appearance [13, 14].

Figure 5.2 (b) presents SEM morphology of HoGO where we observed mixed nanostructures such as wrinkles symbolizing GO sheets and rod-like structures showing successful doping with Ho^{3+} ions. In Figure 5.2 (c) we have the SEM image of HoGO/P3HT which presented a smooth surface morphology and small islands. The small islands that have been noticed are the result of degassing during drying process. This demonstrates that diffusion took place at the interface between HoGO and P3HT. Our findings are in line with the results by Tian *et al.* [15] who declared that the organic substances, such as polymers and tiny molecules, are more comprehensible and frequently used as components to modify nanoparticle morphology.

5.3.3 FTIR analysis

Figure 5.3 presents the FTIR spectra which assist in analysing different vibrational frequencies of the layered nanostructures in the frequency range 4500-500 cm^{-1}.

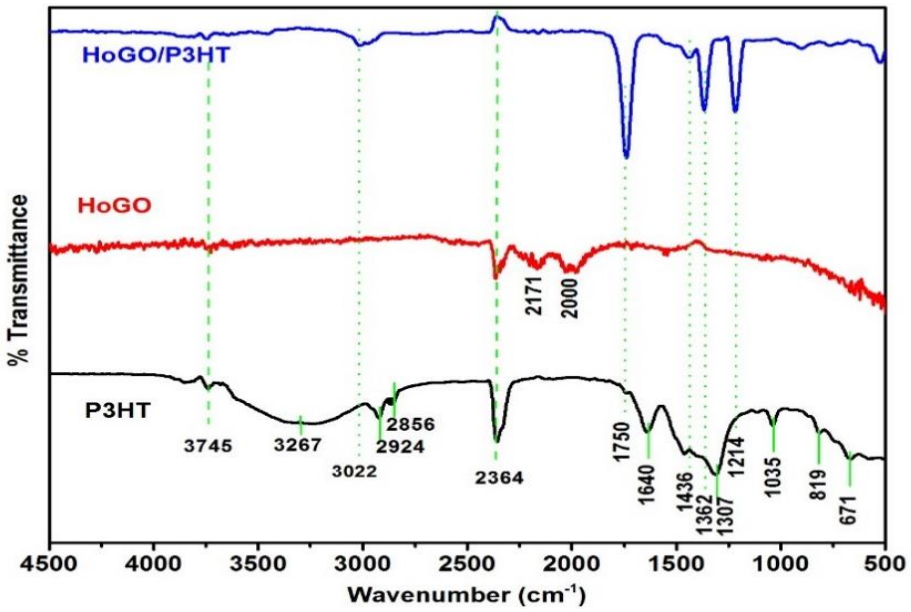

Figure 5. 3 FTIR spectra of P3HT, HoGO and HoGO/P3HT layered nanostructures.

From the acquired information on different layered nanostructures, there is a carbon related peak at ~ 2364 cm^{-1} which originates from environmental CO_2 due to its hygroscopic

property. The spectrum of pure P3HT presented primary vibration bands at the following positions ~ 671, ~ 819, ~ 1035 and ~ 1307 cm^{-1} which symbolize the aromatic out of plane =C-H vibration band. These vibration bands are well known to come from 2.5-disubstituted-3hexylthiophene for rr-P3HT chain conformation [16]. Moreover, we have seen the C-H vibration band at ~ 1460 cm^{-1} which relates to the symmetric and aliphatic C-H stretching vibrations at positions ~ 2856 and ~ 2924 cm^{-1}.

We have seen a small band at ~ 1750 cm^{-1} which is assigned to C=O stretching vibration. This band verifies the existence of the ester group and it is enhanced for the HoGO/P3HT layered nanostructure. The HoGO layered nanostructure has only small bands around ~ 2000 and ~ 2171 cm^{-1} which represent the oxygen containing groups on the surface. Four distinct, strong adsorption peaks were observed at ~ 1241, ~ 1362, ~ 1436 and ~ 1750 cm^{-1} for HoGO/P3HT layered nanostructure. These peaks are associated with the C-H vibration band, indicating that the thiophene has partially decomposed [17]. Only for P3HT there is a band centred at ~ 3267 cm^{-1} that indicate water absorption on the surface of P3HT. A decrease in HoGO/P3HT vibrational frequencies may be due to interface oxygenation.

5.3.4 UV/VIS/NIR analysis

Figure 5.4 represents a typical absorption measurement which is useful in assessing the level of intra and interchain order in layered nanostructures containing P3HT.

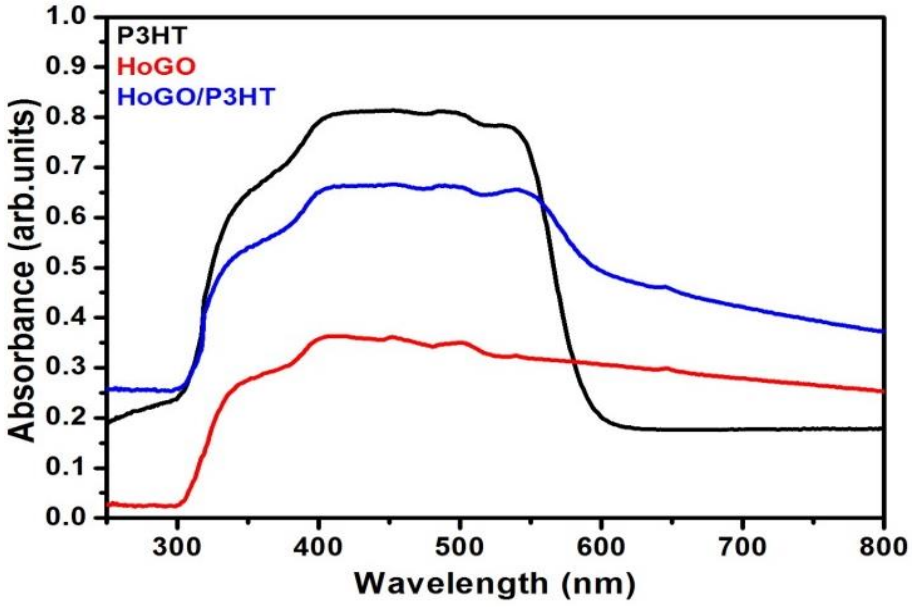

Figure 5. 4 UV-Vis spectra of P3HT, HoGO and HoGO/P3HT layered nanostructures.

When comparing individual layered nanostructures, P3HT appeared to be more absorbing in the wavelength region 300 - 600 nm. The spectrum for HoGO layered nanostructure has a smaller absorption in comparison to P3HT. The creation of multilayered HoGO/P3HT nanostructure improved the absorption characteristics that led to absorption increase in the wavelength range 600 - 800 nm. Moreover, we observed similar characteristics of absorption for HoGO and HoGO/P3HT layered nanostructures due to their interface interaction. This is due to the fact that the arrangement of organic elements remains the same after the thin layer has dried entirely. Some studies revealed that when the interchain interaction between organic compounds is altered, the absorption maxima frequently shift to the blue or red region [16, 18]. However, we found no wavelength shift, showing that the interchain interaction is not the cause of the increased absorption. We attribute the improved absorption to an increase in internal reflection brought on by a different configuration of organic components in thin films. Absorption increase for HoGO/P3HT between 600 - 800 nm may have been caused by extremely delocalized electrons with low charges generated along the backbone of the π-conjugated thiophene upon development of multilayered nanostructure [19].

5.4 Conclusion

The research conducted here extends the scope of growing thin film nanostructures by employing GO doped with Ho in the active layer of organic solar cells in conjunction with P3HT. The grown thin film nanostructures were characterized using various spectroscopic techniques to confirm the interactions at the interface. The XRD results revealed pure phases of the prepared nanostructures without impurities. The surface morphology of Ho doped GO resembled combination of sheets and rod-like structures which changed due to infiltration of polymer upon growing P3HT. Changes in FTIR stretching and vibrational modes provide evidence of chemical interaction at the interface of thin film nanostructures. From optical absorbance measurement we observed the enhancement in absorption for the HoGO/P3HT thin film nanostructure over a wide spectral range. These discoveries can be used to create hybrid nanostructures based on graphene in organic solar cell technology.

5.5 References

[1] R. Liu, *Materials*, **7** (2014) 2747.

[2] R. Zhang, B. Li, M.C. Iovu, M. Jeffries-EL, et al., *J. Am. Chem. Soc.* **128** (2006) 3480.

[3] G. Li, V. Shrotriya, J. Huang, Y. Yao, T. Moriarty, K. Emery and Y. Yang, *Nat. Mater.* **4** (2005) 864.

[4] K. Tremel and S. Ludwigs, *Adv. Polym. Sci.* **265** (2014) 39-82.

[5] Y. Wang, S. Yang, H. Wang, L. Zhang, H. Cheng, B. He, W. Li and B. Zou, *Curr. Appl. Phys.* **17** (2017) 343.

[6] Z. Yang, X. Shi, J. Yuan, H. Pu and Y. Liu, *Appl. Surf. Sci.* **257** (2010) 138.

[7] F. Vetrone, R. Naccache, V. Mahalingam, C.G. Morgan and J.A. Capobianco, *Adv. Funct. Mater.* **19** (2009) 2924.

[8] F.V. Molefe, M. Khenfouch, M.S. Dhlamini and B.M. Mothudi, *Adv. Mater. Lett.* **8** (2017) 246.

[9] M. Khenfouch, U. Buttner, M. Baitoul and M. Maaza, *Graphene* **3** (2014) 7.

[10] P. Ehrenreich, S.T. Birkhold, E. Zimmermann, H. Hu, K.-D. Kim, J. Weickert, T. Pfadler and L. Schmidt-Mende, *Scientific Reports* **6** (2016) 32434.

[11] K. Zhao, Zi. Ding, L. Xue and Y. Han, *Macromol. Rapid Commun.* **31** (2010) 532.

[12] S. Joshi, S. Grigorian, U. Pietsch, P. Pingel, A. Zen, D. Neher and U. Scherf, Macromolecules **41** (2008) 6800.

[13] Z. Wu, A. Petzold, T. Henze, T. Thurn-Albrecht, R.H. Lohwasser, M. Sommer and M. Thelakkat, *Macromolecules* **43** (2010) 4646.

[14] A. Zen, J. Pflaum, S. Hirschmann, W. Zhuang, F. Jaiser, U. Asawapirom, J.P. Rabe, U. Scherf and D. Neher, *Adv. Funct. Mater.* **14** (2004) 757.

[15] H. Tian, G. Boschloo and A. Hagfeldt, *Green Chemistry and Sustainable Technology*, Springer.

[16] R.K. Singh, J. Kumar, R. Singh, R. Kant, S. Chand and V. Kumar, *Materials Chemistry and Physics* **104** (2007) 390.

[17] P. Kovacikand and O. College, "Vacuum Deposition of organic molecules." PhD thesis University of Oxford.

[18] C.-X. Sheng and Z.V. Vardeny, *Fundamentals Materials devices and Fabrication*, ISBN:978-3-662-45508-1 (2015) 3.

[19] R.K. Singh, J. Kumar, R. Singh, R. Kant, R.C. Rastogi, S. Chand and V. Kumar, *New J. Phys.* **8** (2006) 112.

Chapter 6: The Effect of Deposition Method and Thickness Dependence on the Growth of P3HT Donor Material for Organic Photovoltaic Devices

6.1 Introduction

The on growing energy demand globally has led to serious environmental pollution and global energy shortages [1]. To overcome these challenges, renewable energy resources are promising as they can address the need for sustainable development by replacing fossil fuels [2]. Thus, organic photovoltaic (OPV) devices have been steadily developed to assist with energy shortages. Progress has been made on development of OPV solar cells but there is a lot of competition from traditional all-organic and arising perovskite solar cells. Poly(3-hexylthiophene-2,5-diyl) (P3HT), which can be easily synthesized at a large scale and is inexpensive to produce, is the material that is most frequently researched in OPV [3]. A lot need to be done on the molecular level engineering of P3HT in order to achieve highly efficient OPV devices. Over the past decade extensive research has been conducted on the use of P3HT but the effect of various deposition methods and thickness dependence is missing for application in OPV devices [4]. P3HT is one of the stable semiconducting organic polymers which can be utilised for fabrication of devices as it is amorphous in nature and when compared to inorganic semiconductors it has less mobility [5]. Mostly it is used as an electron donor due to its outstanding optoelectronic properties that allows devices to reach higher power conversion efficiency (PCE). Furthermore, it surpasses other conductive polymer materials due to its conjugated structure that provides π electrons which facilitates conduction [6]. Other advantages include good environmental and thermal stability, excellent chemical and physical properties, higher energy storage and increased electrochemical performance [7, 8]. The thin film characteristics such as crystallinity and thickness among others play a vital role on the entire device functioning. To obtain highly crystalline layers of P3HT, it is necessary to pre-aggregate nanofibrils in solution and then deposit those aggregates on a substrate. These enable the dissociation of crystallization from the process of thin film deposition. However, thin film formation for the device fabrication requires cheap and fast techniques to create homogenous films at a large scale.

Opting for the best deposition technique that gives uniform thin films is a unique feature for layered nanostructures for application in photovoltaic devices. It is noticeable that there are a lot known, well developed deposition techniques such as dip-coating [9], electro coating [10], spray pyrolysis [11], spin-coating [12], drop-casting [13] and electrospinning [14]

respectively, well implemented to achieve thin-films of high quality mainly for device fabrication. Some of these methods make the processing easily scalable and utilize the material in a cost-effective way than others. Noebels *et.al.* reported on the use of spray-coating method for growing polymers for photovoltaics, wherein they encountered roughness of the surface after coating to be the main drawback [15]. Additionally, the droplets formed in spray atomization translated into crater-like structure in films on substrates, with relatively flat central areas and markedly raised edges. It is well known that deposition of conjugated polymers is conducted from solutions prepared using some good solvents such as chloroform etc. with techniques such as spin-coating, doctor-blading, dip-coating and inkjet-printing [16]. Brinker *et al.* reported that the crystalline structure of thin films may be affected by the deposition method choice, such as dip-coating and spin-coating [17]. Spin-coating has been the industry standard for a long time when fabricating optoelectronic devices over length scale of up to 10 of cms [18, 19]. But there are limitations associated with this technique, whereby a huge fraction of the active materials is unavoidably wasted during deposition process. Recently, a variety of active materials have been used to examine this adaptable, trustworthy, and affordable technology for application in optoelectronic devices. On the other hand, drop-casting is a very simple and important technological method to manufacture single or multilayer films for various application [20]. In practice, this method produces thick films of good quality, but it is difficult to control the thickness. Among others, Dhatchinamurthy *et al.* explored the use of dip-coating method for solar cell applications and declared it to be easy, smooth to handle and cost effective [21].

It is worth noting that OSCs typically comprise a multilayer nanostructure from which the layers in the device may be formed by using different deposition techniques. To the best of our knowledge, there are only few reports on the use of dip-coating method into the world of polymer solar cells. The results obtained in this study will enlighten us of possible reasons why this method has not been fully followed. With regards to commercially viable techniques, production at a large scale is still a big challenge encountered by a lot of researchers. Therefore, it is of high importance to come up with new manufacturing processes and/or improve the existing to fine tune their capabilities so that thin films of large areas and various shapes can be developed.

We report a comparative study on various thin film deposition methods (spin-coating, dip-coating and drop-coating) and establish thickness dependence of P3HT thin film based on structure, morphology and optical properties. Thin films were deposited using P3HT solution

with the same concentration to get better control over nanoparticles distribution, quality and thickness. The interest in processing of OPV devices has mainly been on the properties of various materials used to produce polymer composites and we report on the capabilities of various deposition methods used to achieve enhanced charge transport from the donor material. Discovering simple, rapid and cost-effective deposition method for growth of thin-films using functional nanomaterials is of great importance for their potential applications. The results demonstrated that various deposition methods produced P3HT thin films with varying thicknesses that affected the thin film structure, surface morphology and optical properties.

6.2 Experimental

6.2.1 Nanomaterial preparation and coating procedure

We purchased pure regioregular poly (3-hexylthiophene-2,5-diyl) (rr-P3HT > 99%) and chlorobenzene (CB anhydrous, 99.8%) from Sigma-Aldrich Co. South Africa and utilised them in their analytical grade state without any purification for thin film deposition.

The 5% concentration of P3HT solution was prepared using chlorobenzene as a solvent for dispersion according to the procedure outlined in our previous studies [22]. Before the deposition, the 2 cm × 2 cm non-conductive glass substrates were carefully cleaned sequentially inside ultrasonic bath using deionised water, acetone, iso-propanol and ethanol, respectively. The non-conductive glass substrates were then treated with UV-ozone to improve the hydrophilia of the surface. Micropipette was used to extract 50 μl of P3HT solution for both spin-coating and drop-coating procedures. Spin-coating was performed at 4000 rpm for 50 s and for drop-casting we ensured that the solution is distributed all over the substrate. Dip-coating experiments were conducted by immersing a glass substrate into P3HT solution for 20 s and withdrawn at a speed of 2 mm/s, allowing the liquid solution to flow freely with self-gravity. The thin film formed at the backside of the non-conductive glass glass substrate was cautiously cleaned using polyester swabs moistened with ethanol. After dipping, the non-conductive glass substrate was dried on a hotplate at temperature of 60 ℃ for 20 min and the process was repeated 10 times to allow the solution to stick on the non-conductive glass substrate. Finally, the grown thin films were all soft annealed at 125 ° C for 5 min on a hot plate prior characterization. Typical P3HT thin film thicknesses were

determined using profilometer and were found to be ~ 31 nm spin-coated, ~ 83 nm dip-coated and ~ 148 nm drop-coated.

6.2.2 Thin film characterization

The crystal structure of the thin films was identified using Rigaku Smart-Lab X-ray diffractometer (XRD) equipped with nickel-filtered Cu Kα ($\lambda = 0.154$ nm) monochromatic radiation generated at 45 kV and 200 mA at room temperature over 2θ range 5-90°. Raman spectroscopy was used for structural analysis using Horiba Scientific Xplora with Laser light excitation wavelength ~ 532 nm. The morphological analysis of the thin-films was probed by the field emission scanning electron microscopy (FESEM), model JSM-7800F from JEOL Ltd. equipped with an Ultra-Dry EDS detector. The optical properties of thin films were recorded in absorption mode using PerkinElmer Lambda spectrometer, model 1050 UV/VIS/NIR equipped with integrating sphere in the wavelength range 300-800 nm. The emission characteristics of the material were probed using Horiba Fluorolog-3 - Photoluminescence (PL) system with Xenon lamp 450 W, as excitation source and signal was captured using PMT detector. The emission spectra were collected under an angle of 25° relative to the substrate normal. The PL decay dynamics were measured using time-correlated single photon counting (TCSPC), Model: F980 methodology, Edinburgh Instrument excited with 400 nm pulsed laser. The instrument response function (IRF) was < 100 ps. The thicknesses of P3HT thin-films were estimated using conventional contact-type surface profilometer with a 12 µm tip (Dektak 6M Veeco, US).

6.3 Results and Discussion

6.3.1 XRD analysis

In order to study the structure of P3HT thin films grown using different deposition methods, XRD spectra was acquired as illustrated in Figure 6.1. The obtained crystal structure of P3HT thin films from three different methods reveals two diffraction peaks with 2θ values around ~ 6.65 and ~ 22.2 °. The main diffraction peak at ~ 6.65 ° is attributed to the interchain arrangement of P3HT linked with the interdigitated alkyl chains [23].

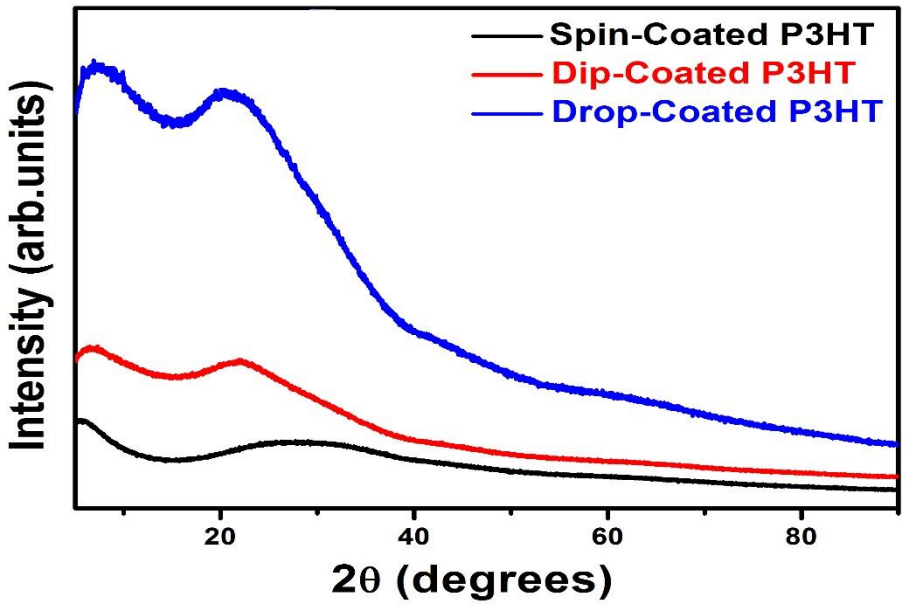

Figure 6. 1 XRD patterns of P3HT thin films grown using various deposition methods.

There is a gradual change in broadness and intensity of P3HT wherein drop-coated P3HT appears to be narrower and have the highest diffraction intensity. We confirmed differences in broadness by calculating the full width at half maximum (FWHM) by fitting a Gaussian curve to the peak at ~6.65 °. The FWHM were obtained to be: ~ 10.1 spin-coated, ~8.25 dip-coated and ~6.77 ° drop-coated, respectively. The cause of differences in broadness could be due to inhomogeneous strain related to lattice parameters [24]. Cheng *et al*. [25], attributed higher intensity and narrow half-width of [100] diffraction peak to the formation of large crystal size. This infer to agglomerated P3HT forming crystallite particles which diffracts more giving rise to the intensity than homogenously distributed particles from spin-coated and dip-coated thin films. Other than the variations in diffraction intensities and broadness of the peaks which indicates the order of organization of the structures, the spectra of P3HT thin films is dominated by the amorphous nature of the polymer. The observed variations on structure of P3HT agrees with the report by Brinker *et al.* [17], who suggested that the crystalline structure of thin films may be affected by the deposition method chosen. Shalu *et al.* [26], reported on crystallization of P3HT thin films cast in two different solvents (Chlorobenzene (CB) and Chloroform (CF)) mainly focusing on (100) diffraction peak in the lower 2θ region. They indicated that, spin coated pristine P3HT has a weak diffraction peak which corresponds to the ordered self-organised lamella structure with an interlayer spacing, created by stacks of P3HT main chains oriented in parallel. Those main chains are said to be divided by regions packed with alkyl side chains [27, 28]. The arrangement of the polymer

chains and crystallinity are shown to have a significant impact on the photo-response in optoelectronic devices [26]. The crystallinity is improved by increasing thin film thickness.

6.3.2 Raman analysis

Further structural analysis on P3HT thin films grown using various deposition methods has been conducted using Raman technique as shown by the spectra in Figure 6.2. From 500-1200 cm^{-1} region, weak vibration bands can be seen which symbolises P3HT molecules.

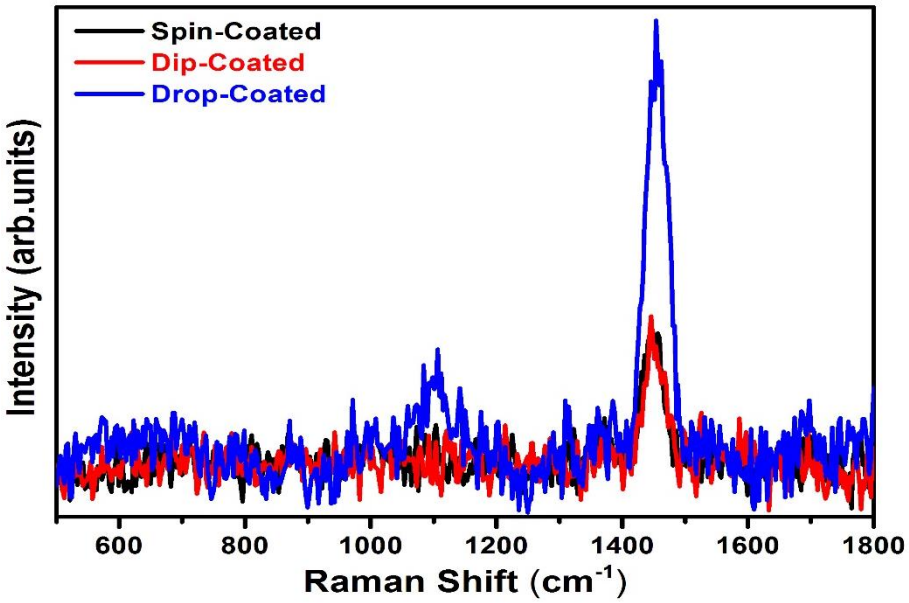

Figure 6. 2 Raman spectra of P3HT thin films grown using various deposition methods.

The obtained data as shown in the spectra elucidate the presence of resolved bands in the range 1400-1600 cm^{-1}. The most dominant peak is located at ~ 1452 cm^{-1}, which is attributed to symmetric $C=C$ stretching vibrations of the thiophene ring [27]. The peak position, line width and intensity for the ~ 1452 cm^{-1} Raman mode are said to be highly sensitive to the molecular ordering [28]. Moreover, the ~ 1452 cm^{-1} mode possess symmetry with respect to the conjugation direction. Rahmani *et al.* [29] reported on two peaks we did not obtain at ~ 1380 and ~ 1575 cm^{-1} assigned to the $C-C$ intra-ring stretching modes of P3HT. Studies showed that Raman bands of P3HT at positions ~ 1380 and ~ 1452 cm^{-1} are supposed to be sensitive to π-electron delocalization or conjugation length of P3HT molecules [30, 31]. Veerender *et al.* declared that the ~ 1380 cm^{-1} Raman band is insensitive to the degree of molecular order and to the excitation wavelength [32]. From our results, it

can be clearly seen that the ~ 1452 cm^{-1} vibration varies in intensities. The peak for drop-coated thin film is highly intense than the spin-coated and dip-coated thin films. Tsoi *et al.* indicated that the stronger the relative intensity of $C=C$ mode compared with $C-C$ mode represents a decrease in planarity of the P3HT chains and the enhanced electron-phonon coupling of $C-C$ mode, lastly the improved charge transfer from $C=C$ bonds [28]. Thus, this is the reason why $C-C$ mode is suppressed in our results symbolizing highly ordered drop-coated thin film over spin-coated and dip-coated P3HT thin films.

6.3.3 SEM analysis

In order to study the effect of deposition methods on the surface morphology of P3HT thin films, SEM images are presented in Figure 6.3. The SEM of P3HT deposited using spin-coater reveals clusters of nanoballs distributed uniformly over the surface as presented in Figure 6.3 (a). Figure 6.3 (b) presents SEM of the dip-coated P3HT showing nanoballs morphology with some islands in between.

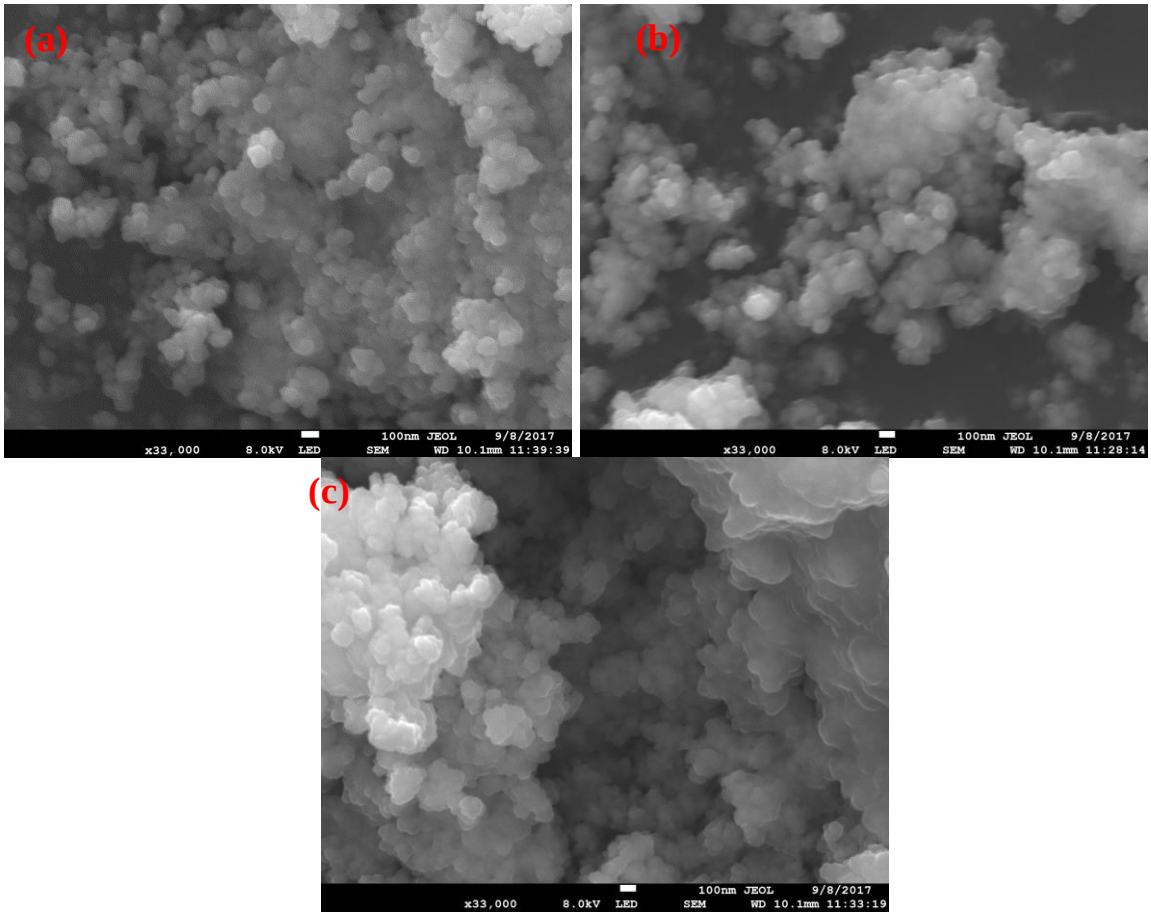

Figure 6. 3 SEM images of P3HT thin films grown using various deposition methods: (a) spin-coating, (b) dip-coating and (c) drop-coating.

The observed islands depict areas which were not well coated with P3HT during dip-coating process. This symbolizes strong thickness variations for dip-coated thin film that generated highly agglomerated particles in certain areas and isolated particles in other parts. Hu *et al.* [33], indicated that with dip coating, in terms of solvent evaporation and thin film formation, a room temperature of 20 °C produces a uniform film and dependable coating. P3HT thin film obtained from drop coating method presented in Figure 6.3 (c) shows nanoballs which are highly clustered with enlarged size than those from other methods. The enlargement in nanoballs morphology agrees with the increase in crystallite size observed in XRD for the drop-coated thin film. The clustering of nanoballs is due to gravitational agglomeration where clusters are formed as a result of particles that were settling more quickly catching slower settling particles [34]. Cluster formation is a dynamic process when coating using drop-casting method as drops come together under quiescent conditions caused by van der Waals forces and Buoyant force. In between nanoballs morphology there are some small pores attributed to degassing induced by soft annealing of the thin films.

Similar nanoballs morphology on electrodeposited TCTA polymer material was reported by Chai *et al.* [35]. Overall, the clustered morphology of P3HT indicates that it is highly cohesive, which is a crucial property that enables it to transfer charges when used in optoelectronic devices. It has been reported that distinct organic thin films (OTFs) have different morphologies since they can't be manufactured under the same fabrication conditions, which leads to these morphological variances [36].

6.3.4 FTIR analysis

Figure 6.4 presents the FTIR spectra of P3HT thin films grown using different deposition methods. The results obtained from three deposition methods are comparable to one another as they exhibit similar peaks at essentially identical frequencies, indicating similar structure of the deposited P3HT thin films. Other than that, there are negligible differences in the intensities or energies of certain peaks. Therefore, it can be reasonably deduced that vibrational modes of P3HT does not rely much on the method of deposition. Moreover, the change in thin film thickness produced neither an increase nor decrease in vibrational frequencies.

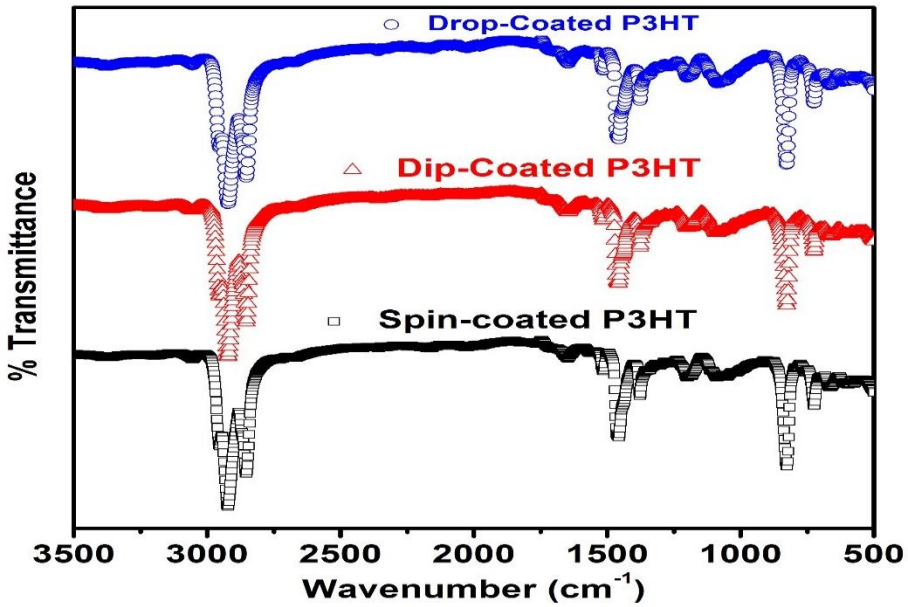

Figure 6. 4 FTIR spectra of P3HT thin films grown using various deposition methods.

The strongest absorption band is seen at ~ 2920 cm^{-1} due to $-CH_2$ stretch vibration with two significant absorption bands adjacent to it ~ 2958 and ~ 2852 cm^{-1} corresponding to the $-CH_3$ asymmetry and $-CH_2$ stretch vibration. The two bands observed near ~ 1462 and ~ 1506 cm^{-1} are assigned to the $C=C$ symmetric ring stretching vibration and $C=C$ asymmetric ring stretching vibrations, respectively. The thiophene peak prevails at ~ 1379 cm^{-1} and is attributed to the $C-S$ stretching mode. The elongated characteristic peak at ~ 821 cm^{-1} confirms the existence of aromatic $C-H$ out of plane vibrations which is a characteristic of (3-hexylthiophene-2, 5-diyl) [37]. The P3HT peak at ~ 735 cm^{-1} represents the methyl (CH_3) rock band. In general, the obtained results from three various methods of deposition are consistent with the work we reported earlier for pristine P3HT [22].

6.3.5 UV-vis analysis

Figure 6.5 (a) depicts the normalized absorption spectra of P3HT thin films grown using different deposition methods. The spin-coated P3HT thin film reveal the absorption maximum at ~ 450 nm that originates from π-π∗ transitions [38]. At ~ 590 nm there is a well resolved shoulder which is induced by vibronic advancement of the C=C stretching mode that assists with the formation of the P3HT crystalline domains in the film [39]. It is said to be indicative of the inter-chain modification of pristine P3HT thin films [31]. The absorption at ~ 450 nm is blue shifted for the dip-coated P3HT thin film and it is abnormal to see this

blue shift which is said to relate to defect states within the bandgap of P3HT thin films [40, 41]. This defect states can be attributed to variations observed in surface morphology formed by different deposition methods leading to different thicknesses of the thin films that alleviated the insertion of oxygen or humidity into P3HT thin films. The other absorption edge is observable at ~ 510 nm which is in line with the π-π^* transition of conjugated P3HT chains [42]. The drop-coated P3HT thin film present enhancement in absorbance maxima concomitant the change in shape and peak wavelength observed for the dip-coated P3HT thin film. This indicates that the drop-coated P3HT thin film has a higher degree of ordering. We presume the enhancement in absorbance is provoked by an increase in P3HT thin film thickness. Cavallari *et al.* [43], noticed modification of shape and shifting of peak position for P3HT with an increase in thin film thickness upon normalizing absorbance spectra of P3HT. This shows that the greater the thickness of an active layer the higher the chances of harvesting more photons. The energy band gap of P3HT thin films was estimated using Tauc's plot [44] by extrapolating the linear fitted line in the ($\alpha h\nu$) vs $h\nu$ plots corresponding to the fundamental absorption edge region as shown in Figure 6.5 (b). Upon increasing P3HT thin film thickness we observed a reduction in energy band gap at ~ 1.93 eV for spin-coated, ~ 1.91 eV dip-coated and ~ 1.92 eV drop-coated P3HT thin films, respectively. The variation in energy band gap is marginal. These smaller energy band gap values denote an increase in conjugation lengths than the spin-coated P3HT thin film [45].

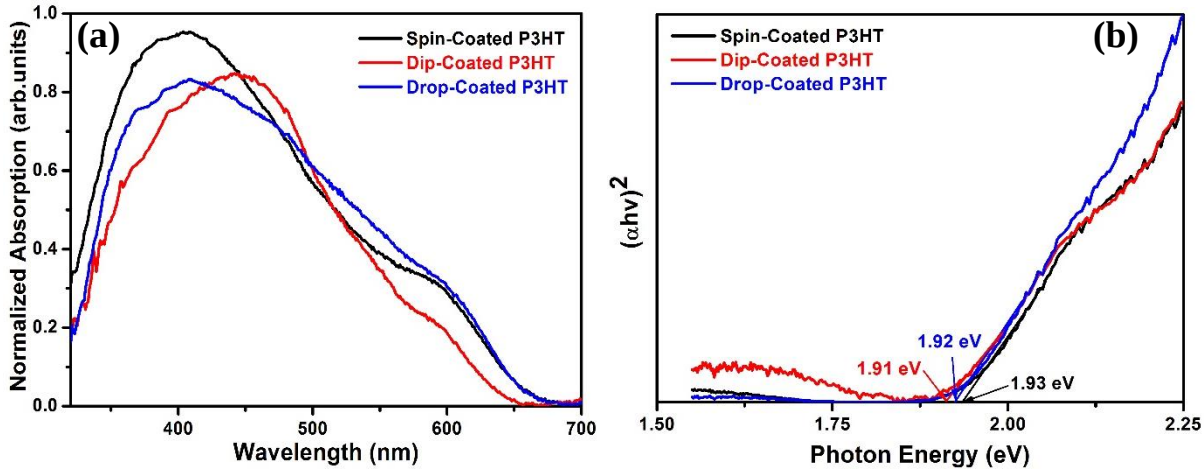

Figure 6. 5 (a) UV-Vis absorption spectra, (b) energy band gap of P3HT thin-films grown using various deposition methods.

6.3.6 Photoluminescence analysis

Figure 6.6 depicts the PL emission spectra of P3HT thin films over the range 500-800 nm grown using various deposition methods acquired at 410 nm photoexcitation which corresponds to the strongest vibronic state in the absorption spectra. The spin-coated spectra reveal partially two shoulders at ~ 637 nm and ~ 670 nm which corresponds to the (0-0) and (0-1) transitions of aggregates in P3HT thin films [46]. The peak emission in the higher wavelength region ~ 670 nm is said to indicate ordering in the P3HT lamella structure within spherulites [47]. The PL intensity of dip-coated thin film is enhanced compared with spin-coated thin film and further increase is noticed for drop-coated thin film which may be correlated with higher absorption of photons. The enhancement in the emission intensity denotes that the defect density increases with P3HT thin film thickness. This elucidates that as P3HT thickness increases, more photons are absorbed leading to the increase in the emission intensity. It is of noting that the enhancement mainly occurred to the ~ 637 nm peak which is also blue shifted denoting the change in polymer conformation while the ~ 670 nm peak remains at the same position. Based on literature reports, the enhancement in PL emission intensity is provoked by the increase in thin film thickness [48]. Moreover, the blue shift denotes the change in conjugation length and ordering in the polymer chains [31].

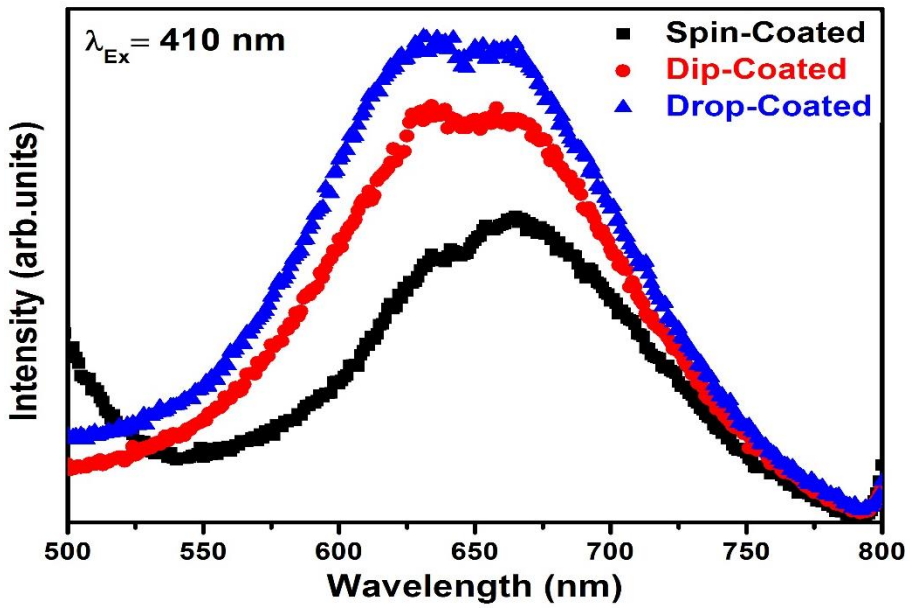

Figure 6. 6 PL emission spectra of P3HT thin films grown using various deposition methods.

6.4 Conclusion

In this work different deposition methods for growing P3HT thin films were investigated with the goal of identifying ideal coating techniques for OPV devices. A comparative study on P3HT thin films deposited using spin-coating, dip-coating and drop-coating methods is conducted and thin film thickness dependence is evaluated. XRD results indicated that drop-coating method yields highly crystalline P3HT thin film based on high intensity of the diffraction peak and a reduction in FWHM which is vital for photo-response in optoelectronics. SEM micrographs indicated that spin-coating produces uniformly distributed nanoballs morphology while other methods demonstrated agglomerates with voids in between. The increase in thickness of P3HT thin film led to enhanced optical properties with reasonable energy band alignment. We observed considerable differences in PL emission intensity of P3HT thin films from various deposition methods. The enhancement in PL intensity with the increase in thin film thickness was indicative of an increase in the number of defect states. In terms of crystallinity and optical characteristics the drop-coated P3HT thin film provides the potential to lead to efficient charge transfer as a donor material in OPV devices.

6.5 References

[1] M.Z. Jacobson, *Energy Environ. Sci*., **2** (2009) 148-173.

[2] M. Liserre, T. Sauter and J.Y. Hung. *IEEE. Ind. Elecron. Mag*., **4** (2010) 18-37.

[3] M.T. Dang, L. Hirsch and G. Wantz, *Adv. Mater.*, **23** (2011) 3597-3602.

[4] D. Baran, R.S. Ashraf, M. Abdelsamie et.al, Nat. Mater., **16** (2016) 363-369.

[5] L. Peng, L. Hu and X. Fang, Adv. Mater. 25(2013)5321-5328.

[6] L. Liu, P. Hu, Y. Li, W. An, J. Lu and W. Cui, *Appl. Surf. Sci*., **466** (2019) 928-936.

[7] D. Motaung, G. Malgas, C. Arendse, S. Mavundla, C. Oliphant and D. Knoesen, *Sol. Energy Mater. Sol. Cells*, **93** (2009) 1674-1680.

[8] Y. Zhu and Y. Dan, *sol. Energy Mater. Sol. Cells*, **94** (2010) 1658-1664.

[9] M. Behpour and V. Atouf, *App. Surf. Sci*., **258** (2012) 6595-6601.

[10] A. Saini, F.S. Etheridge, K.C. Peters, S.Pejić, L. Gao, S.D. Hellring, D.E. Schuele, G. Sauvé and K.D. Singer, *Org. Electron.* **53** (2018) 332-338.

[11] F. Matteocci, G. Mincuzzi, F. Giordano, A. Capasso, E. Artuso, C. Barolo, G. Viscardi, T.M. Brown, A. Reale and A.D. Carlo, *Org. Electron.* **14** (2013) 1882-1890.

[12] A. Timoumi, H.M. Albetran, H.R. Alamri, S.N. Alamri and I.M. Low, *Superlattices Microstruct.* **139** (2020) 106423.

[13] A.F. Huq, A. Ammar, A.M. Al-Enizi and A. Karim, *Polymer* **113** (2017) 200-213.

[14] W. Serrano-Garcia, I. Bonadies, S. Thomas and V. Guarino, *Mater. Lett.* (2020) 127458 in-Press.

[15] M. Noebels, R.E Cross, D. Evans and C.E. Finlayson, *J. Mater. Sci.* **49** (2014) 4279-4287.

[16] K. Tremel and S. Ludwigs, *Adv. Polym. Sci.* 265 (2014) 39-82.

[17] C.J. Brinker, A.J. Hurd, P.R. Schunk, G.C. Fryeand C.S. Ashley, *J. Non-Cryst. Solids*, 147-148 (1992) 424-436.

[18] C. McNeill, and N. Greeham, *Adv. Mater*., **21** (2009) 3840-3850

[19] F. Krebs, *Sol. EnergyMater. Sol. Cells*. **93** (2009) 394-412.

[20] Y. Mu, L. Hang, G, Zhao, X. Wang, Y, Zhou and Z. Cheng, *Mathematics and Computers in Simulation*, 169 (2020) 88–102.

[21] L. Dhatchinamurthy, P. Thirumoorthy, L. Arunraja, S. Karthikeyan, *Materials Today: Proceedings* (Article in Press).

[22] F.V. Molefe, M. Khenfouch, M.S. Dhlamini and B.M. Mothudi, *Advanced Material Letters* **8** (2017) 246-250.

[23] B. Kadem and A. Hassan, The effect of fullerene derivatives ratio on P3HT-based organic solar cells, *Energy Procedia* **74** (2015) 439-445.

[24] T. Morita, V. Singh, S. Nagamatsu, S. Oku, W. Takashima and K. Kaneto, Enhancement of Transport Characteristics in Poly(3-hexylthiophene) Films Deposited with Floating Film Transfer Method, *Applied Physics Express* **2** (2009) 111502.

[25] H.-L. Cheng, W.-Q. Lin and F.-C. Wu, "Effects of solvents and vacancies on the electrical hysteresis characteristics in regioregular poly(3-hexylthiophene) organic thin-film transistors," Appl. Phys. Lett. **94** (2009) 223302.

[26] C. Shalu, M. Shukla, A. Tiwari, J. Agrawal, A. Bilgaiyan and V. Singh, *Physics E: Low-dimensional Systems and Nanostructures* **115** (2020) 113694.

[27] V. Singh, S.S. Pandey, W. Takashima, K. Kaneto, *Jpn. J. Appl. Phys.* **48** (2009) 061503

[28] K. Bhargava, V. Singh, *Appl. Phys. Express* **9** (2016) 091601.

[29] M. Rahmani, L. Jerbi and A, *J. Lumin.* **217** (2020) 116805.

[30] Y. Yacoby, E. Ehrenfreund, in: M. Cardona, G. Gfintherodt (Eds.), *Springer, Berlin/Heidelberg*, **68** (1991) 73.

[31] T. Sharma, R. Singhal, R. Vishnoi, G.B.V.S. Lakshmi, S. Chad. D.K. Avasthi, A. Kanjilal and S.K. Biswas, *Vacuum* **135** (2017) 73-85.

[32] P. Veerender, V. Saxena, A.K. Chauhan, S.P. Koiry, P. Jha, A. Gusain, S. Choudhury, D.K. Aswal, S.K. Gupta, Sol. Energy Mater. Sol. Cells 120 (2014) 526-535.

[33] Z. Hu, J. Zhang, S. Xiong and Y. Zhao, Performance of polymer solar cells fabricated by dip coating process, *Sol. Energy Mater. Sol. Cells* **99** (2012) 221-225.

[34] A. Singer, Z. Barakat, S. Mohapatra and S.S. Mohapatra, *Nanocarriers for Drug Delivery*, *Nanoscience and Nanotechnology in Drug Delivery*, *Micro and Nano technologies* (2019) 395-419.

[35] J. Chai, Y. Zhang, F. Liu, H. Zhang, X. Zhang, J. Xu and G. Zhang, *J. Electroanal. Chem.* **852** (2019) 113502.

[36] Y. Shi, J. Liu, and Y. Yang, Device performance and polymer morphology in polymer light emitting diodes: The control of thin film morphology and device quantum efficiency, *J. Appl. Phys.* **87** (2000) 4254-4263.

[37] T. Sharma, R. Singhal, R. Vishnoi, G.D. Sharma and S.K. Biswas, *Physica B: Condensed Matter* **537** (2018) 306-313.

[38] S. Kumar, J. Kumar, S.N. Sharma and S. Srivastava, *Optik* **178** (2019) 411-421.

[39] M. Chevrier, G. Lopez, W. Zajaczkowski, J. Kesters, R. Lenaerts et al. Synthesis and properties of a P3HT-based ABA triblock copolymer containing a perfluoropolyether central segment, *Synthetic Metals* **252** (2019) 127-134.

[40] S. Kim, B. Kang, M. Lee, S.G. Lee, K. Cho, H. Yang and Y.D. Park, Sequential solvent casting for improving the structural ordering and electrical characteristics of polythiophene thin films. *RSC Adv* 4 (2014) 41159‑41163.

[41] F. Landgrave-Barbosa, A.F. Marmolejo-Valencia, A. Baray-Calderón, et al., Impact of thickness of spin-coated P3HT thin films, over their optical and electronic properties. *J Solid State Electrochem.* **26** (2022) 649–661.

[42] M.T. Khan, A. Kaur, S.K. Dhawan and S. Chand, *Journal of Applied Physics* **110** (2011) 044509/1-7.

[43] M.R. Cavallari, J.E.E. Izquierdo, E.F.G. Rodríguez, M.A. Pereira-da-Silva and F.J. Fonseca, Optical absorbance of P3HT thin films used to estimate simultaneously thin film thicknesses and morphology for gas sensing. Proc. of SPIE Organic Photonics + Electronics **9568** (2015) 95682B-1 - 95682B-9.

[44] P. Mahendia, G. Chauhan, H. Wadhwa, G. Kandhol, S. Mahendia, R. Srivastava, O.P. Sinha, T.D. Clemons and S. Kumar, *J. Phys. Chem. Solids*, **148** (2021) 109644.

[45] C. H. García-Escobar, M.E. Nicho, Hailin Hu, G. Alvarado-Tenorio, P. Altuzar-Coello, G. Cadenas-Pliego and D. Hernández-Martínez, Effect of Microwave Radiation on the Synthesis of Poly(3-hexylthiophene) and the Subsequent Photovoltaic Performance of CdS/P3HT Solar Cells. *Int. J. Polym. Sci.* 1926972 (2016) 1-9.

[46] G.L. Kabongo, P.S. Mbule, G.H. Mhlongo, B.M. Mothudi, K.T. Hillie and M.S. Dhlamini, Photoluminescence Quenching and Enhanced Optical Conductivity of P3HT-Derived Ho^{3+}-Doped ZnO Nanostructures. *Nanoscale Research Letters* 11 (2016) 1-11.

[47] F. Alam, N. Kumar and V. Dutta, Effect of thickness on the performance of hybrid solar cells fabricated using surfactant free lead sulphide quantum dots and poly(3-hexylthiophene-2,5-diyl) polymer. *Thin Solid Films* **631** (2017) 180-188.

[48] A. Gundimeda, M. Mishra, R. Ahmad, R. Srivastava, U.K. Dwivedi and G. Gupta, Influence of active layer thickness on electrical properties of P3HT /n-Si based hybrid heterostructure, *Indian I. Pure & Appl. Phys.* **56** (2018) 468-474.

Chapter 7: Interactions in GO/P3HT Layered Nanostructures: Spectroscopic Investigation for Organic Solar Cells

7.1 Introduction

Currently photovoltaic (PV) devices are more viable and promising non-polluting way of generating electricity that would replace conventional fossil fuels. Nanotechnology is a wide interdisciplinary research area that has the capacity to solve global energy problems in our societies. The use of graphene has grown very rapidly all over the world for the past decade as a super star nanomaterial for tackling energy challenges [1]. It is applicable in various applications such as field-effect transistors (FETs), transparent electrodes and optoelectronics devices [2, 3]. Graphene is widely used because of its remarkable characteristics like high specific surface area, (theoretically 2630 m^2/g for single-layer-layer graphene), electron transport capabilities and extraordinary electronic properties as well as high thermal conductivity (~5000 $Wm^{-1}K^{-1}$) [3, 4]. Furthermore, the unique characteristics of graphene lead to tremendous attention on its derivatives that includes graphene oxide (GO) and reduced graphene oxide (rGO) [1, 2]. The graphene derivatives have also gained attention of researchers which led to wide usage in consumer products and industrial applications globally [5, 6]. In particular, there are numerous ways to create composite materials based on graphene using GO because the processes are readily scalable and may be less expensive [6].

GO nanostructures can be prepared using physical and chemical methods following the top-down and bottom-up approaches. Among different methods implemented in efforts to prepare GO nanostructures, there is microwave method [7], mechanical exfoliation from graphite [8] and chemical exfoliation (chemical oxidation of graphite and subsequent reduction of the exfoliated graphite oxide sheets) also called Hummer's method [9]. Amongst these methods, mechanical exfoliation is an easy method for producing graphene, although the yield is quite small, and it is quite difficult to obtain high quality industrial production. Hummer's method which is a top-down approach is chosen in this study particularly because of the benefits like cheap cost, big scale and high yield preparation of graphene sheets. Furthermore, it improves the dispersion stability of the produced GO and is environmentally friendly, with no visible surface flaws [4].

Graphene has been widely studied for functionalization using P3HT on the basis of π-π^* interactions between them [10]. Making use of the knowledge that both graphene and GO

share the common features of delocalized and conjugated electron structures, we expect that P3HT would show similar interactions with GO as it has shown with graphene. To our advantage, the existence of oxygen containing functional groups such as (-OH, -COOH, -O- etc.) in GO facilitates chemical functionalization in addition to bringing solubility for film production through solution processes such layer-by-layer self-assembling [10,11]. To create layered nanostructures in this study, we coated polymeric P3HT on top of GO layer. It is widely known that P3HT-derived thiophene derivatives are high hole mobility materials with substantial electron delocalization along the chemical backbone. Thus, P3HT/GO layered nanostructured material have the capacity to improve device performance due to their increased charge carrier mobility [12]. GO attracted a lot of attention as a new class of efficient hole and electron extraction nanomaterial in solar cells. The creation of layered nanostructures using GO and P3HT is likely to show enhanced interactions for the emerging area of photovoltaic technology. The present work reports on simple and effective approach for the preparation of layered P3HT and GO/P3HT nanostructures.

Hummer's method was employed during synthesis of GO which is utilized for creating layered nanostructures of GO/P3HT on a glass substrate. A comparison research between P3HT and GO/P3HT is conducted to demonstrate potential applications of bilayer structure in optoelectronic devices. The main objective is to investigate the chemical interaction between GO/P3HT layered nanostructures. We discovered that π-π^* interactions at the interface of GO/P3HT play a vital role in generating highly dispersible GO sheets. This work provides the direction on growing P3HT and tailoring its properties with GO in layered nanostructure form, thus creating perspectives for photovoltaic devices.

7.2 Material and Methods

7.2.1 Materials preparation and deposition

The graphite powder (99 %), $KMnO_4$ (98 %), H_2SO_4 (98 %), H_2O_2 (30 %), H_3PO_4, chlorobenzene (99 %) and P3HT (99 %) respectively, were purchased from Sigma Aldrich (South Africa) and were used as given without any additional purification. The solvents and reagents employed during synthesis, characterization and fabrication of photovoltaic devices were also purchased from Sigma Aldrich.

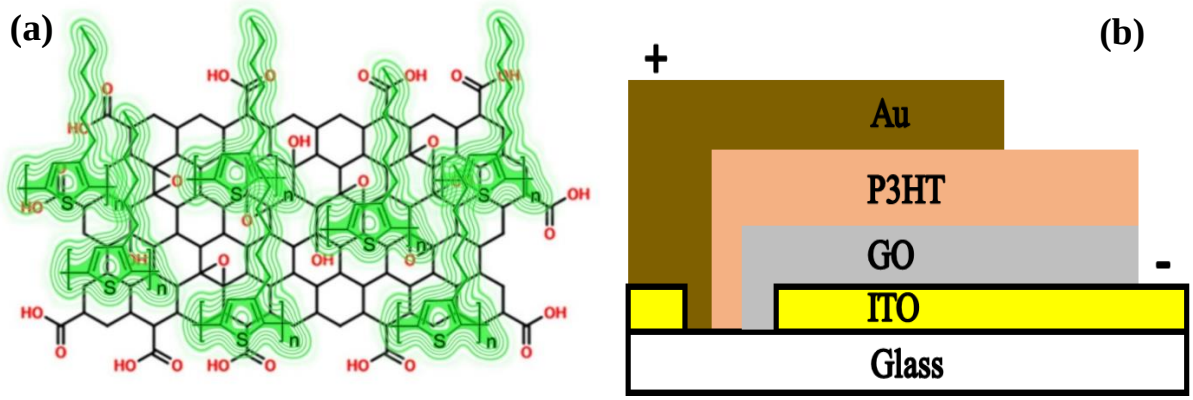

Figure 7. 1 Schematic representation of (a) P3HT and GO upon interaction (b) GO/P3HT layered nanostructures and their device architecture.

Figure 7.1 demonstrates the chemical structures of P3HT and GO upon interaction and the fabricated solar cell device. The GO sheets were prepared following modified Hummers method as reported elsewhere [13]. To create a 5% concentration solution, P3HT was dispersed in chlorobenzene. On a magnetic hot plate with an ambient temperature of 80 °C, the solution was agitated for 10 minutes. Then, the temperature was lowered to 50 °C while the solution was constantly stirred for 1 hour, and it was cooled at room temperature after that. The resulting orange suspension was used to grow layered nanostructures. The $2cm \times 2cm$ glass substrates were first cleaned in the ultrasonic bath sequentially using acetone, ethanol and deionized (DI) water for 10 min each respectively. Thereafter, substrates were dried at 50 ℃ prior coating. Micropipette was used to extract 50 μl of both GO and P3HT solution for spin-coating. GO solution was spin-coated at 1400 rpm for 1 min on a bare substrate while P3HT solution was coated at 800 rpm for 50 sec on both bare substrate and GO coated substrate. After coating, the P3HT and GO/P3HT layered nanostructures were soft annealed for 5 min at 100 ℃ on a hot plate to remove residual solvents.

7.2.2 Materials and device characterization

The crystalline phases of the layered nanostructures were identified by Rigaku Smart Lab Xray-diffractometer with CuKα (1.5418Å) radiation. Scanning Electron Microscope (SEM) (Shimadzu model ZU SSX-550 Superscan) was used to determine the shape of layered nanostructures. Fourier transformed infrared (FTIR) spectrum of the layered nanostructures was acquired by PerkinElmer spectrometer in the spectral range 400 - 4000 cm^{-1}. The optical reflectance analysis was carried out in the 200 - 900 nm spectral range using a PerkinElmer Lambda spectrometer, model 1050 UV/VIS/NIR. The time-resolved photoluminescence

(TRPL) were conducted using a 400 nm pulsed laser and the response was captured using time-correlated single photon counting (TCSPC), Model: F980 methodology, Edinburgh Instrument. The instrument response function (IRF) was < 100 ps. The electrical measurements were acquired under illumination using Keithley model 2400 digital source meter. The voltage was swept between -0.5 to 0.5 V at the voltage interval of 0.01 V with the current fixed at 2.5 A. The spectral mismatch between the solar simulator's emission (NEWPORT class A, 1 600 W) and the global AM1.5G solar spectrum (IEC 60904-3 Ed. 2) was rectified using a mismatch factor, and the solar simulator's irradiance was adjusted correspondingly using a certified silicon reference cell in order to produce an equivalent AM1.5G irradiance of one sun (100 $mW\,cm^{-2}$) on the test cells.

7.3. Results and discussion

7.3.1 XRD analysis

The XRD pattern of layered P3HT and GO/P3HT nanostructures are presented in Figure 7.2. The pristine P3HT is dominated by a major diffraction peak at ~ 6.65 ° which is comparable to (100) orientation of the P3HT polymer and its interlayer spacing is ~ 16.8 Å. The most intense diffraction found in polymer crystallites corresponds to the a-axis orientation (100) pointing in the direction of the alkyl chains i.e. main polymer chains are parallel and alkyl side chains are perpendicular to the substrate [14]. This peak is associated with the lamella structure of thiophene rings in P3HT [15]. Furthermore, a broader peak is observed at ~ 22.08 ° which is induced by the stacking of the chains within the main chain layer [16]. The observed diffraction peaks are not sharp, which indicates that P3HT has an amorphous structure.

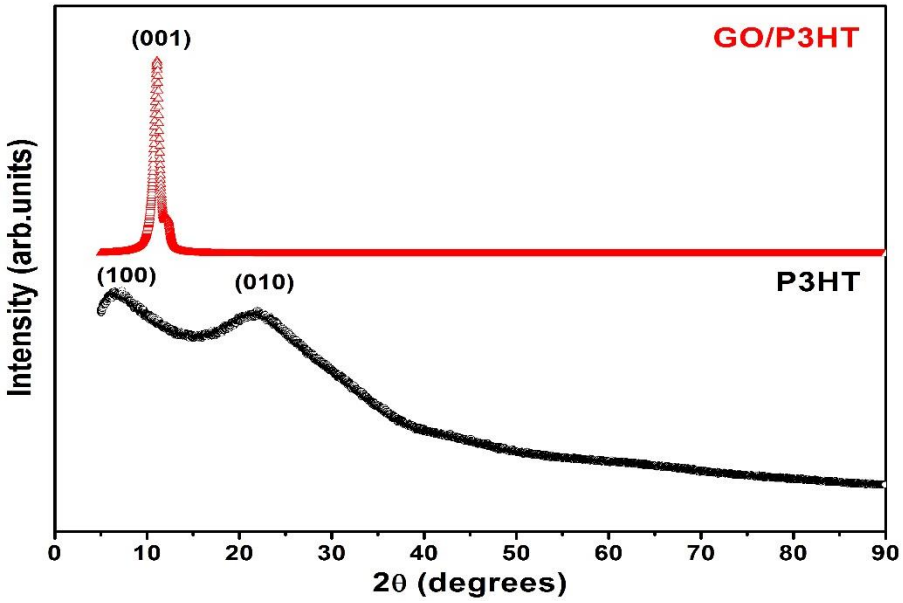

Figure 7. 2 The XRD patterns of the P3HT and GO/P3HT layered nanostructures.

The layered GO/P3HT nanostructure reveals a (001) reflection at ~ 11.1 ° which has an interlayer spacing of ~ 7.23 Å. Interestingly, no P3HT characteristic diffractions were observed in the layered GO/P3HT nanostructure, indicating that highly crystalline GO reflection masked diffractions coming from amorphous P3HT. The obtained (001) reflection of GO seen in GO/P3HT has been shifted to higher diffraction angles due to interaction with P3HT compared to diffraction of pure GO prepared using Hummer's method which is reported to be at $2\theta = 10.36$ °, which corresponds to interlayer spacing of 8.53 Å [17]. The observed shift is due to decrease in interlayer spacing as the "edge-on" orientation of P3HT lamellae facilitates the insertion of GO layers between P3HT lamellae [13]. The aforementioned insertion enhanced interaction between layered GO/P3HT nanostructures by increasing the number of interfaces. The highly crystalline diffraction of layered GO has been reported elsewhere [12]. Stylianakis *et al.* [15], reported on the (002) main reflection of stacks of GO with a 6.7 Å interlayer distance and a finite number of layers ~ 18 positioned at ~ 13.2 °.

7.3.2 SEM analysis

Figure 7.3 (a) and (b) shows the surface morphology of the prepared P3HT and GO/P3HT layered nanostructures studied using the SEM analysis technique. The surface aspects of pristine P3HT layer depicted in Figure 7.3 (a) appear featureless. This smoother surface

shows that P3HT was uniformly distributed without cracks and segregation. The observed surface morphology is consistent with the results reported by Khan *et al.* [18].

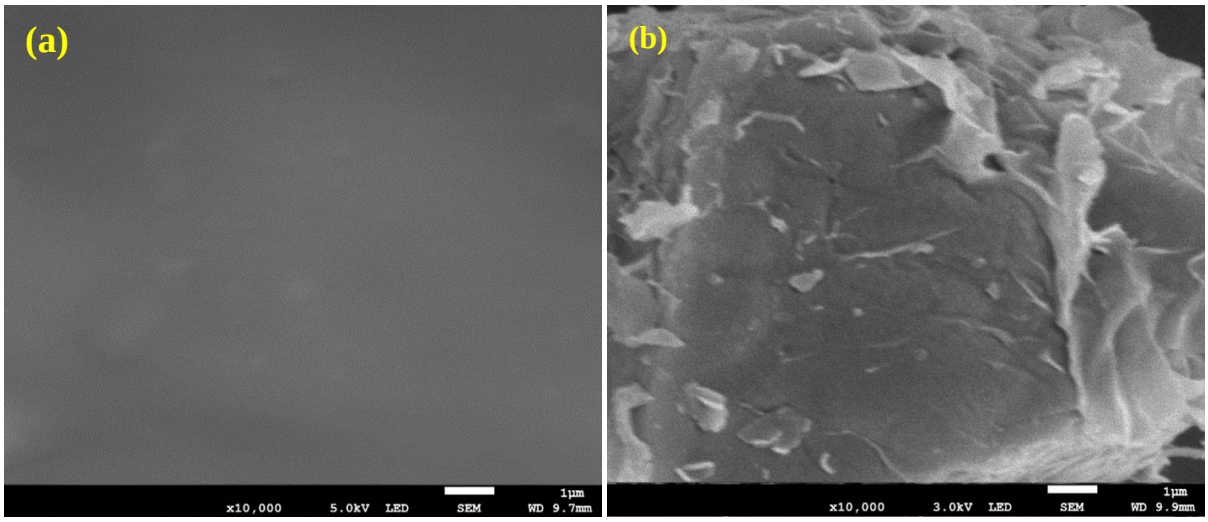

Figure 7. 3 The SEM images of (a) P3HT and (b) P3HT/GO layered nanostructures.

The SEM image for layered GO/P3HT nanostructure in Figure 7.3 (b) reveals slightly wrinkled surface at the centre with stacked sheets towards the edges indicating GO layers. These sheets are well connected and wrapped with thin layer of P3HT polymer. It can be deduced that slight wrinkles dictate region of uniformly distributed GO sheets, while the formation of stacks indicates agglomerated GO sheets. We believe the agglomerated GO sheets towards the edges are induced by GO solution that drifted while experiencing centripetal force that drove it radially outward to cover the surface of the substrate during spin coating. One should notice that thinner layer and well dispersed P3HT allowed us to observe the sheets of GO. This is presumably due to well intimate contact between the basal plane of GO and P3HT that lead to strong interactions most probably between the π-orbitals of the thiophene ring and GO. Sriram *et al.* [19], reported rod-like structures for pristine P3HT and they indicated that GO/P3HT composites morphology changes between spherical, particulate, flake-like and crumbled structures is based on the concentration of GO.

7.3.3 FTIR analysis

The linkage at the interface of GO/P3HT layered nanostructures were analysed in order to investigate the bonding interactions using FTIR measurements in transmission mode as shown in Figure 7.4 (a). From pristine P3HT layer we observed the primary bands at positions ~ 2960, ~ 2925 and ~ 2855 cm^{-1} that symbolizes aliphatic $C-H$ stretching of

P3HT. The absorption band at ~ 2960 cm^{-1} corresponds to the $-CH_3$ asymmetry stretch vibration, while bands at ~ 2925 and ~ 2855 cm^{-1} represents $-CH_2$ stretch vibration [16].

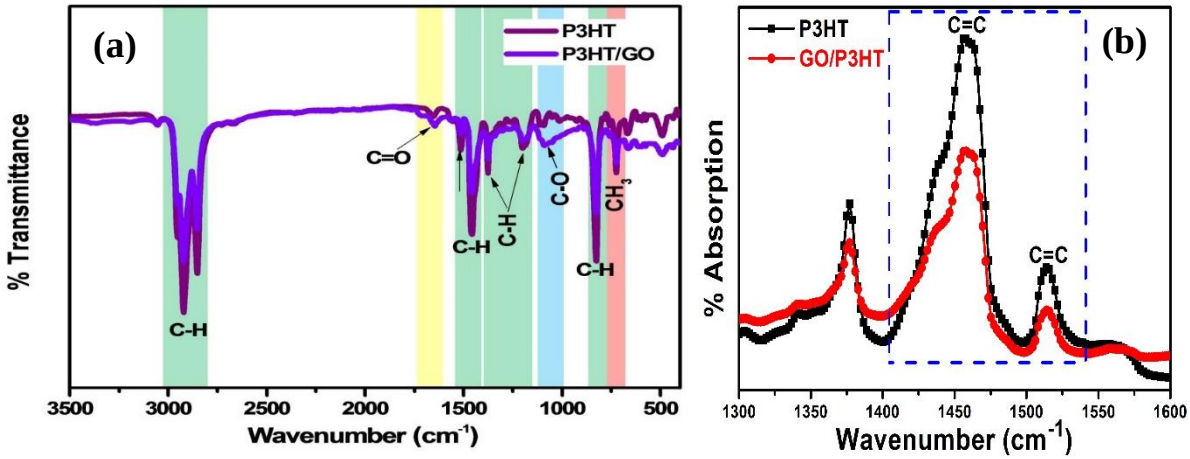

Figure 7. 4 (a) FTIR spectra (b) enlarged view of P3HT and GO/P3HT layered nanostructures.

The spectra further show a band at ~ 1462 cm^{-1} which is related to bending vibration of $C-H$ bond and the band at ~ 1510 cm^{-1} is associated with asymmetric $C=C$ ring stretching vibrations. The observed ~ 1378 cm^{-1} $C-H$ vibration band could be as a result of partial decomposition of the thiophene [20]. Detailed evaluation of GO/P3HT layered nanostructure reveals the emergence of vibrational bands at ~ 3372, ~ 3194 and ~ 1081 cm^{-1} which are characteristic to contribution from GO. The $C-O$ bond at ~ 1081 cm^{-1} represent the stretching vibrations which affirm the existence of oxide functional groups after the oxidation process [21]. Furthermore, GO/P3HT spectrum reveals a band at ~ 1648 cm^{-1} which is assigned to the amide carbonyl stretching mode also called Amide I vibrational stretch $\nu(C=O)$ [22]. These variations indicate that interactions between GO and P3HT leads to the derivatization of both the edge carboxyl and surface hydroxyl functional groups via formation of amides [21]. The vibration band positioned at ~ 821 cm^{-1} corresponds to aromatic $C-H$ out of plain vibration and it is the characteristic of (3-hexylthiophene) which indicates the structure of P3HT contains rr-P3HT chains [10]. The characteristic band at ~ 721 cm^{-1} represents both methyl rock mode and the CH_3 rocking vibration. The obtained characteristic features of P3HT and GO/P3HT layered nanostructures are similar to those reported earlier [13].

It is worth noting that P3HT and GO/P3HT layered nanostructures exhibited similar vibrational frequencies with most peaks at essentially identical positions, but the relative intensities of GO/P3HT layered nanostructures are reduced. To examine the structural alteration, we are only using the ratio of two peaks (I_{1510}/I_{1462}) shown in Figure 7.4 (b) from which the average conjugation length of P3HT is decreased from ~ 1.20 to ~ 1.12 upon growing GO/P3HT layered nanostructure. According to Furukuwa *et al*. [23], the relative intensity of the IR mode at 1510 cm^{-1} (asymmetric $C=C$ stretching) is enhanced when the average conjugation length increases. Smaller conjugation length is obtained corresponding to a decrease in ordering of polymer matrix. We presume that, the observed decrease in intensity of GO/P3HT vibrational frequencies signifies reduction in ordering of polymer structure due to oxygenation when GO interacts with P3HT leading to structural deformation. Therefore, the decrease in conjugation length further supports the XRD results where decrease in interlayer spacing was observed due to insertion of GO layers within polymer structure as the number of interfaces increase.

7.3.4 UV/VIS/NIR analysis

Figure 7.5 (a) shows the diffuse UV-vis reflectance spectra of the layered P3HT and GO/P3HT used to investigate the absorption behaviour of the nanostructures. The reflectance spectrum of pristine P3HT layer indicates absorption edge below 600 nm and it has highest % reflectance of ~ 97 %. The absorption edge of GO/P3HT is red shifted compared to that of P3HT. The observed red shift is associated with sufficiently increased chain motion, which indicates an increase in the crystalline ordering that results in stabilization of the P3HT chains [24]. According to study by Li *et al*. [25], the red shift is in accordance with the improvement of light absorption capability of P3HT upon growing GO layer. It is observed that, upon growth of the GO/P3HT layers the absorption band is a bit stronger indicated by decrease in % reflectance. The observed stronger absorption is attributed to π-π* transition between P3HT and GO because of presence of nanoparticles of various sizes [26]. This may possibly be the result of a decrease in the chain segments' effective conjugation lengths in the amorphous P3HT, which more closely localizes the exciton wave function and raises its energy [27]. The undertaken interaction is linked to inter-chain order (a rise in P3HT chains' disorder), which improves the absorption spectrum [28]. Thus, the decrease in % reflectance for GO/P3HT provides proof that the donor polymer and acceptor GO underwent a charge transfer reaction that produced a highly absorbent multilayer nanostructure.

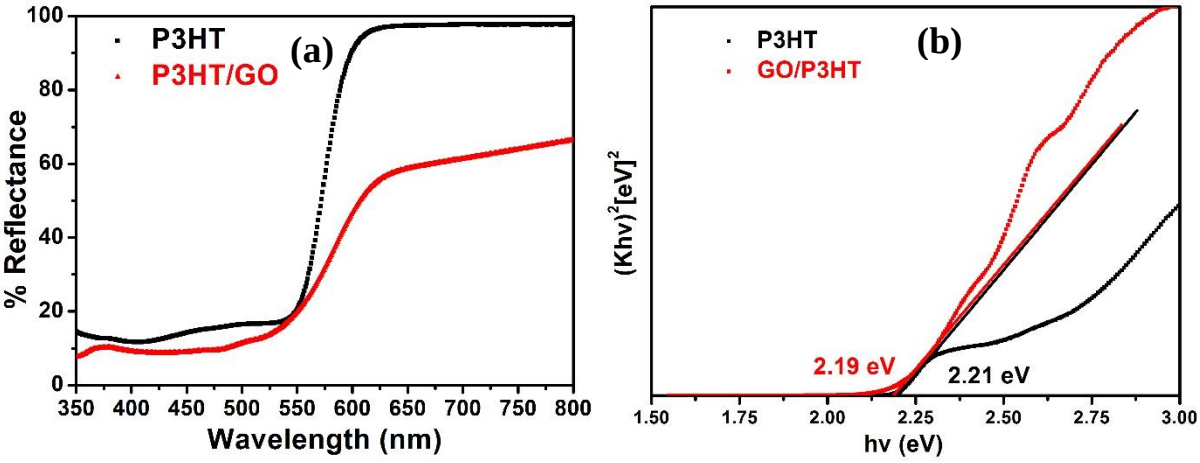

Figure 7. 5 (a) Diffuse reflectance spectra, (b) bandgap energy of P3HT and GO/P3HT layered nanostructures.

The bandgap energy of the P3HT and GO/P3HT layered nanostructures was estimated using Kubelka Munk reemission function [29]. Figure 7.5 (b) depicts the relationship between $(Khv)^2$ versus the photon energy (hv) from which the optical bandgap of the layered nanostructures was extrapolated by fitting the linear part of the spectrum to the value $hv = 0$. The estimated bandgap energy values of P3HT and GO/P3HT layered nanostructures are ~ 2.21 and ~ 2.19 eV, respectively. Thus, we observe a slight decrease in bandgap energy of P3HT induced by the interaction with GO nanoparticles. Therefore, due to the low optical bandgap of the acceptor - GO than that of donor - P3HT, this resulted in reduction of bandgap energy for GO/P3HT. According to the study by Ansari *et al.* [30], the band gap energy below 1.9 eV is a prerequisite for enhancing the power conversion efficiency (PCE) in organic solar cells (OSCs). However, larger energy bandgap ~ 2.00 eV acts as a limitation associated with P3HT which hamper efficient absorption of wider region of the solar radiation. The solar spectrum's red and near infrared (IR) wavelengths are the most powerful to be only absorbed by polymer with narrow bandgap in the range (1.2-1.9 eV) [31]. Theoretical study by Bendavid *et al.* [32], showed that pristine P3HT has bandgap of 2.21 eV which gets reduced when experiencing interface with other materials. Saini *et al.* [33] reported that work function (4.50 eV) of graphene-based materials lies between HOMO and LUMO of polymeric composites. GO will therefore serve as an electron acceptor and improve electric conductivity by slightly reducing the bandgap energy.

7.3.5 TRPL analysis

The TCSPC photoluminescence decays of layered P3HT and GO/P3HT nanostructures acquired at an excitation wavelength of 400 nm while monitoring emission at 600 nm are shown in Figure 7.6. The fluorescence decay of the films was analyzed by fitting data to single exponential function shown in equation (7.1) from the instrument analysis software:

$$I(t) = I_0 e^{-(t/\tau_i)} \qquad 7.1$$

where $I(t)$ is the fluorescence intensity at time t, I_0 is the initial fluorescence intensity, and τ_i represents lifetime, respectively.

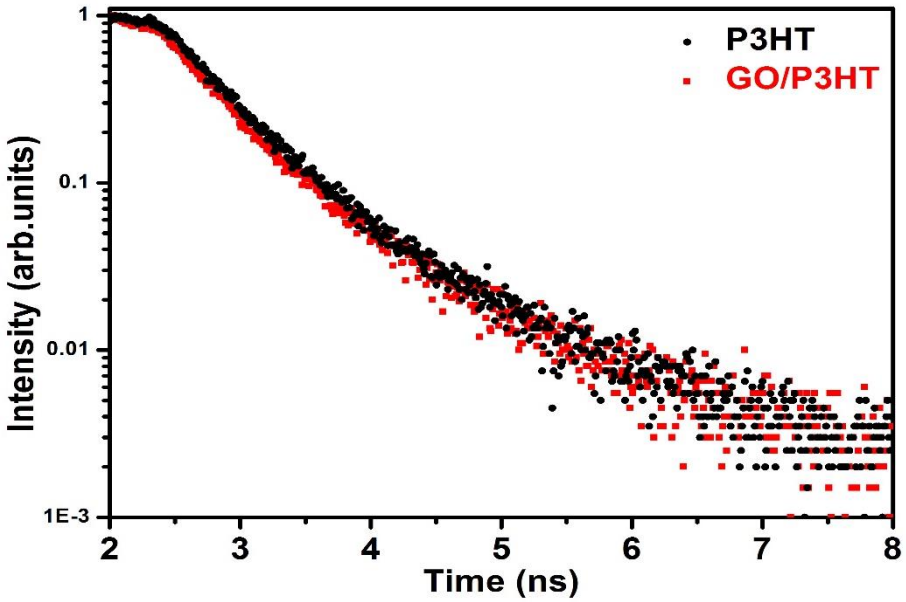

Figure 7. 6 PL decay curves of P3HT and GO/P3HT layered nanostructures.

The decay curve of pure P3HT showed an exciton lifetime of ~ 27.1 ns which is considered as lifetime of excitons from un-adhered P3HT molecules. Contrary to that GO/P3HT revealed a shorter lifetime of ~ 25.8 ns. The reduction in lifetime of GO/P3HT is indicative of exciton dissociation before emission which gives rise to faster charge transfer from P3HT to GO layer. The shortened lifetime is assigned to the existence of extra non-radiative decay pathway due to charge or energy transfer from P3HT to GO [34]. Furthermore, we believe the decrease in lifetime represents low concentration of traps and defects, thus inducing the enhanced quality of the interface between GO and P3HT. This is in line with the results by Zheng *et al.* [35], for whom features in the lifetime of GO/P3HT. From the obtained lifetime

we estimated the exciton diffusion length of the layered nanostructures using equation (7.2) to get more insight into the conformation of the layered nanostructures [36]:

$$L_D = \sqrt{D \times \tau} \qquad 7.2$$

where τ is the exciton lifetime, D is the diffusion constant ($D = 1.8 \times 10^{-7} m^2 s^{-1}$). The calculated exciton diffusion lengths are ~ 69.8 and ~ 67.1 nm for P3HT and GO/P3HT, respectively. Based on literature that ascertained hypothesis of the dependence of electron transfer on energetic driving force, we can speculate that the decreased exciton lifetime for GO/P3HT layer depicts that quicker charge transfer process occurs at the GO/P3HT interface.

7.3.6 Proposed mechanism during charge transfer

In light of lifetime results and by referring to studies conducted on similar architecture, we propose the possible recombination paths in GO/P3HT heterostructure. To understand the transitions between P3HT and GO, a tentative proposed model to illustrate the mechanism by schematic band diagram is shown in Figure 7.7.

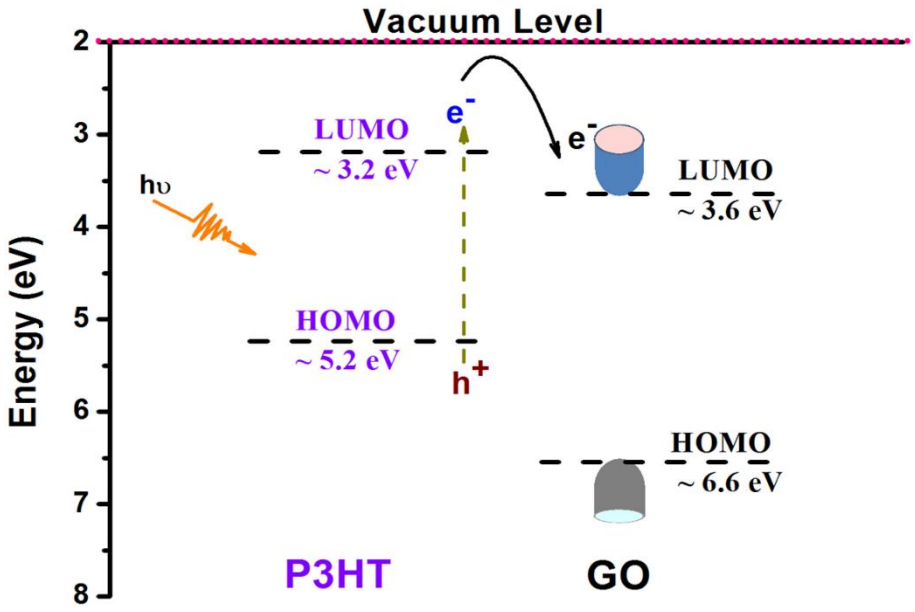

Figure 7. 7 Schematic representation of the energy level diagram showing transitions at the interface between P3HT and GO upon interaction.

In the process, large number of carriers are excited and absorption takes place as electrons are raised from the valence state to the conduction state leaving behind holes in P3HT material thus creating excitons. Herein we are looking at the interface between GO/P3HT frequently

used in solar cell materials [37]. McGehee *et al.* [38], reported that upon creation of exciton due to photon absorption, a powerful driving force is required to divide the electrons and holes in order to overcome the exciton-binding energy between (0.1-0.4 eV) for effective photocurrent creation. Thereafter, the generated excitons diffuse to the heterojunction interface between materials with various ionisation potentials where they dissociate.

In order to attain efficient charge separation, the HOMO and LUMO for the P3HT should be 0.2-0.3 eV higher than that of GO. If the energy difference is too small, it would be difficult to attain efficient charge separation; and if the energy difference is too big, a lot of charges would be lost. Once excitons are dissociated, then follows the ultrafast electron transfer process which mainly depends on interfacial energetic driving force for efficient charge transfer in the heterostructure [36]. The energetic driving force can be expressed by equation (7.3) [39]:

$$\Delta E_{L-CB} = E_L - (IP - E_{CB}) \qquad 7.3$$

where ΔE_{L-CB} represents the interfacial energetic driving force, E_L is the singlet energy of the donor, IP is the ionisation potential of the donor and E_{CB} depicts the conduction band energy level of the acceptor. The Kubelka Munk analysis revealed that P3HT and GO/P3HT layered nanostructures yield bandgap values ~ 2.21 and ~ 2.19 eV, respectively. These values served to estimate the energetic driving force as described in equation (7.3). The energetic driving force for P3HT and GO/P3HT were found to be ~ 0.87 and ~ 0.85 eV, respectively.

Due to the fact that prominent interfacial energetic driving force leads to enhanced electron transfer rate, GO/P3HT needs to be tuned for enhanced photovoltaic properties [35]. Thus, because the LUMO and HOMO for P3HT are higher compared to the ones for GO, the dissociated electron travels through LUMO of GO and the holes travels through the HOMO in P3HT. Lastly, these charges are collected by the electrodes where they induce photocurrent.

7.3.7 IV- analysis

In order to investigate the photovoltaic performance of P3HT and GO/P3HT layered nanostructures, current-voltage characteristic was measured. The photo-current density-voltage curves (J-V) of the P3HT and GO/P3HT devices are presented in Figure 7.8.

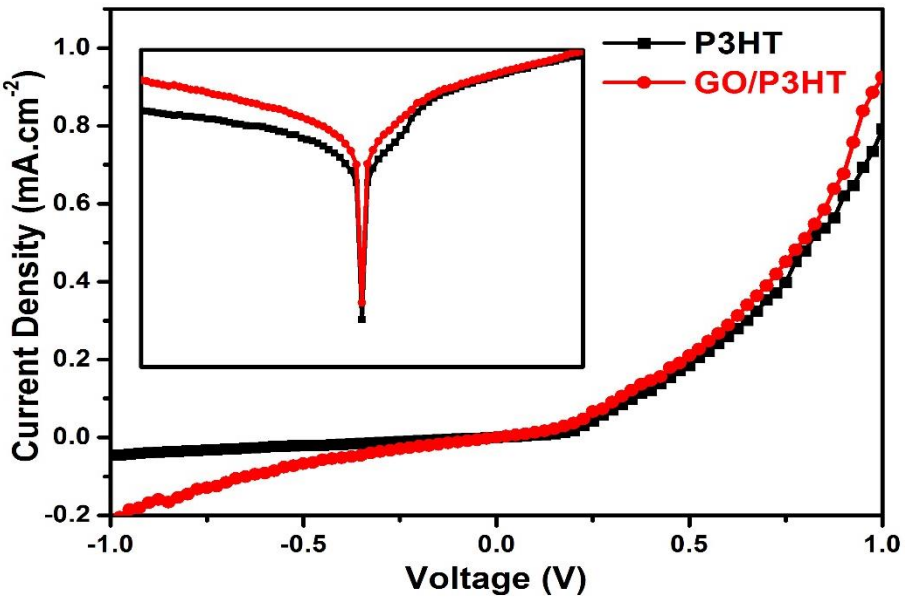

Figure 7. 8 Current density versus voltage (*J-V*) characteristics of P3HT and GO/P3HT devices, insert shows the log of current density (*J*) versus voltage.

The photovoltaic parameters for the P3HT and GO/P3HT devices are recorded in Table 7.1. A GO/P3HT device shows a decrease in V_{OC} and fill factor (FF) compared to those of P3HT, which lead to decrease in PCE. We assume that the reduction in efficiency is caused by irregular interface between GO and P3HT that lead to low interconnectivity for carrier transport. Studies have shown that V_{OC} of BHJ solar cells decreases with higher donor/acceptor interfacial area [34]. However, P3HT is known to produce remarkable results for commercial polymers, this is because the synthesized one contains metal impurities which act as charge trapping centers that causes poor photovoltaic performance [41].

Table 7.1: The photovoltaic parameters of P3HT and GO/P3HT solar cell devices.

Nanostructure	V_{OC} (V)	J_{SC} (mA/cm^2)	FF (%)	η (%)
P3HT	0.434	0.495	0.204	0.0438
GO/P3HT	0.288	0.543	0.196	0.0307

The J_{SC} for GO/P3HT is enhanced, resembling the improved charge mobility associated with formation of continuous pathways for charge transport. These findings support the PL decay measurements where we saw a decrease in exciton lifetime for GO/P3HT. In addition, the increase in J_{SC} may also depict the improvement in light absorption for GO/P3HT, which we witnessed in reflectance measurements. Our results agree with the report by Khan *et al.* [18], who indicated that light harvesting is more in hybrid systems which causes current density to increase. From the insert, it is evident that in forward bias at the low voltage values, the current density rises linearly. But as the voltage increases to higher values, the current density increases exponentially. Similarly, in the reverse bias the current density follows the trend observed in the forward bias.

7.4 Conclusion

In conclusion, the present study was carried out on developed P3HT and GO/P3HT layered nanostructures utilizing a variety of spectroscopic techniques. It was discovered that the structural, morphological, and optical features of GO were affected by its interaction with P3HT. The results from FTIR confirmed the interaction via the presence of oxygen-containing groups and reduction of C-H bands. It was demonstrated that P3HT and GO interacted as donor and acceptor by the decline in percentage reflectance. It is worth mentioning that, the work contributes on growth of layered nanostructures that will be applied in photovoltaics. The reduced lifetime of GO/P3HT than that of P3HT suggests that the photoinduced charge transfer took place from P3HT to GO layer. This charge transfer symbolised by fast decay of GO/P3HT is highly favoured for efficient solar cell devices. The performance of the device was deteriorated by irregular interface between GO and P3HT that lead to low interconnectivity for carrier transport.

7.5 References

[1] K.S. Novoselov, A.K. Geim, S.V. Morozov, D. Jiang, Y. Zhang, S.V. Dubonos, I.V. Grigorieva, A.A. Firsov, *Science* 306 (2004) 666-669.

[2] T. Enoki, *Carbon* 49 (2011) 2579.

[3] T. Lim, C.S. Kim, M. Song, S.Y. Ryu, S. Ju, *Synth. Met.* 205 (2015) 1-5.

[4] J. Song, X. Wang, C. Chang, *J. Nanomater.* (2014) 1-6.

[5] C.K. Chua, M. Pumera, *Chem. Soc. Rev.* 43 (2014) 291-312.

[6] B. Li, Y. Nan, P. Zhang, Z. Wang, Q. Lu, X. Song, *Diamond Relat. Mater.* 55 (2015) 87-94.

[7] N. Kim, G. Xin, S.M. Cho, C. Pang, H. Chae, *Curr. Appl. Phys.* 15 (2015) 953-957.

[8] X.C. Dong, D.L. Fu, W.J. Fang, Y.M. Shi, P. Chen, L.J. Li, *Small* 5 (2009) 1422.

[9] S. Park, R.S. Ruoff, *Nat. Nanotechnol.* 4 (2009) 217.

[10] D. Yu, S.Y. Yang, M. Durstock, J.B. Baek, L.M. Dai, *ACS Nano* 4 (2010) 5633-5640.

[11] Y. Liu, D. Yu, C. Zeng, Z. Miao, L. Dai, *Langmuir* 29 (2010) 6158-6160.

[12] A.C. Obreja, D. Cristea, R. Gavrila, V. Schiopu, A. Dinescu, M. Danila, F. Comanescu, *Appl. Surf. Sci.* 276 (2013) 458-467.

[13] F.V. Molefe, M. Khenfouch, M.S. Dhlamini and B.M. Mothudi, *Adv. Mater. Lett.* **8** (2017) 246-250.

[14] T. Sharma, R. Singhal, R. Vishnoi, G.D. Sharmaa and S.K. Biswas, *Physica B: Condensed Matter* **537** (2018) 306-313.

[15] M.M. Stylianakis, E. Stratakis, E. Koudoumas, E. Kymakis, S.H. Anastasiadis, *ACS Appl. Mater. Interfaces* 4 (2012) 4864-4870.

[16] A.D. Nega, E.K. Pefkiana, G.C. Vougioukalakis, E. Glynos and G. Sakellariou, *Europian Polymer Journal* **83** (2016) 148-160.

[17] C. Hintze, K. Morita, R. Riedel, E. Ionescu and G. Mera, *J. Eur. Ceram.* **36** (2016) 2923-2930.

[18] M.T. Khan, A. Kaur, S.K. Dhawan and S. Chand, *J. Appl. Phys.* **110** (2011) 044509/1-7.

[19] P. Sriram, R. Nutenki, V.R. Mandapati, M. Karupiah and S.I. Kattimuttathu, *Polym. Compos.* **38** (2017) 852-862.

[20] P. Kovacik, O. College, "Vacuum Deposition of organic molecules." PhD thesis University of Oxford.

[21] F.Y. Ban, S.R. Majid, N.M. Huang, H.N. Lim, *Int. J. Electrochem. Sci.* 7 (2012) 4345-4351.

[22] D. Romero-Borja, J.-L. Maldonado, O. Barbosa-García, M. Rodríguez, E. Pérez-Gutiérrez, R. Fuentes-Ramírez, G. de la Rosa, *Synth. Met.* 200 (2015) 91-98.

[23] Y. furukawa, M. Akimoto and I. Harada, *Synth. Met.* **18** (1987) 151-156.

[24] T. Erb, U. Zhokhavets, G. Gobsch, S. Raleva, B. Stuhn, P. Schilinsky, C. Waldauf, C.J. Brabec, *Adv. Funct. Mater.* **15** (2005) 1193-1196.

[25] G. Li, V. Shrotriya, J. Huang et al., *Nat. Mater.* **4** (2005) 864-868.

[26] V. Shrotriya, J. Ouyang, R.J. Tseng, G. Li, Y. Yang, *Chem. Phys. Lett.* 411 (2005) 138-143.

[27] P.J. Brown, D.S. Thomas, A. Köhler, J.S. Wilson, J.-S. Kim, C.M. Ramsdale, H. Sirringhaus, R.H. Friend, *Phys. Rev. B* 67 (2003) 1-16.

[28] J. Arranz-Andrés, W.J. Blau, *Carbon* 46 (2008) 2067-2075.

[29] F.V. Molefe, L.F. Koao, B.F. Dejene and H.C. Swart, *Opt. Mater.* **46** (2015) 292-298.

[30] M.A. Ansari, S. Mohiuddin, F. Kandemirli and M.I. Malik, *RSC Adv.* **8** (2018) 8319-8328.

[31] Y. Gao, M. Liu, Y. Zhang, Z. Liu, Y. Yang and L. Zhao, *Polymers* **9** (2017) 39.

[32] L.I. Bendavid and L.H. Kugelmass, *Surface Science* **695** (2020) 121575.

[33] V. Saini, O. Abdulrazzaq, S. Bourdo, E. Dervishi, A. Petre, V.G. Bairi, T. Mustafa. L. Schnackenberg, T. Viswanathan and A.S. Biris, *J. Appl. Phys.* **112** (2012) 054327.

[34] F. Zheng, X.-Y. Yang, P-.Q. Bi, M-.S. Niu, C-.K. Lv, L. Feng, W. Qin, Y-.Z. Wang, X-.T. Hao and K.P. Ghiggino, Organic Electronics 44 (2017) 149-158.

[35] F. Zheng, W.-L. Xu, Han-Dong Jin, X.-T. Hao and K.P. Ghiggino, RSC Adv., **5** (2015) 89515-89520.

[36] G.L. Kabongo, P.S. Mbule, G.H. Mhlongo, B.M. Mothudi and M.S. Dhlamini, *Bull. Mater. Sci.* (2020) 43:48.

[37] J. Liu, M. Durstock and L. Dai, *Energy Environ. Sci.*, 7 (2014) 1297-1306.

[38] M.D. McGehee and C. Goh, *AIP Conf. Proc.* **1044** (2008) 322.

[39] N. Bansal, L.X. Reynolds, A. MacLachlan, T. Lutz, R.S. Ashraf, W. Zhang et al., *Sci. Rep.* **3** (2013) 1531.

[40] O. Usluer, M. Abbas, G. Wantz, L. Vignau, L. Hirsch, E. Grana, C. Brochon, E. Cloutet, G. Hadziioannou, *ACS Macro Lett.* 3 (2014) 1134-1138.

"I have seen further than other; it is by standing upon the shoulders of Giants"

Isaac Newton

Chapter 8: Simple Approach to Growth, Characterization and Fabrication of GO/ZnO/P3HT Layered Nanostructures for Organic Solar Cell Devices

8.1 Introduction

There is ongoing research into ecologically friendly and renewable energy sources. Photovoltaic (PV) appear to be an attractive alternative replacement of the conventional energy sources. Various generations of solar cells have been explored such as crystalline silicon, thin film and emerging ones [1]. Hybrid solar cells falls within new emerging generations with a vow to address the energy demand globally although they have not been used in the PV market so far. The study of science in the nanometre realm could assist in developing PV technologies for renewable energy harvesting [2]. The superstar nanostructured material that is promising to resolve energy crisis is graphene experimentally discovered in 2004 using mechanical exfoliation [3]. It has attracted the interest of many researches from various discipline because of its exotic properties which were not observed before at the nanoscale.

Practical routes have been adopted to extract individual layers of graphene from graphite through the process of oxidation and exfoliation in aqueous medium which yields graphene oxide (GO) [4]. GO is a derivative of graphene loaded with oxygen - hence the oxide with varying properties to those of graphene which is a pure carbon. It possesses various oxygen - containing functional groups (epoxy, hydroxyl, carbonyl, and carboxyl) as a result, gained interest for potential applications [5]. Many groups have used GO in hybrid solar cells to act both as an exciton dissociation centre and electron selective contact in a hole transport layer [6, 7]. Lately, researchers consider processing of GO by modifying it with other nanomaterials. These structural modifications may reveal new applications that includes solar cells. As a result, a lot of effort has gone into functionalizing or altering the surface of GO sheets with semiconductor nanoparticles [7].

ZnO which is a wide band gap semiconductor with superior charge transport properties is employed in the current research. It has been under intensive focus due to its unique characteristics that includes greater electron mobility in the undoped state, good transparency, greater thermal conductivity and room temperature thermal excited energy (25 MeV) [8]. Furthermore, it has band energies that allows the formation of a heterojunction with organic donor materials such as poly(3-hexylthiophene) (P3HT). Thus, regioregular P3HT is

employed due to its high hole mobility (~0.1 $cm^2V^{-1}s^{-1}$), low bandgap (~1.9 eV), good solubility and processability [9]. This organic semiconductor is widely used because of its p-type transport characteristics, which are crucial factors for performance of solar cells. Therefore, the growth of ZnO layer between GO and P3HT layers is favored to assist with internal electric field. This is due to its multifunctional capabilities where it can act as (i) hole blocking layer due to its wide energy band gap [10], (ii) optical spacer [11], and (iii) it forms an ohmic contact with P3HT blends in inverted structures [12].

In this study, we present the scalable way of growing layered nanostructures using facile synthesis routes to lower the cost of solar cells. The obtained layered nanostructures were characterized by XRD, SEM, FTIR, UV/VIS/NIR and PL. These techniques help to understand the interactions such as covalent, coordination, and ionic bonds within the formed hybrid. Furthermore, we presented the mechanism undergone upon interaction. One of the findings for this research is the enhanced charge transportation from donor to the acceptor through transport layer interesting for application in solar cell devices.

8.2 Experimental

8.2.1 Chemical details

The following chemicals – Poly (3-hexylthiophene), zinc acetate dihydrate, monoethanolamine and methanol (99.8%), Potassium permanganate, Sulphuric acid, Hydrogen peroxide, chlorobenzene, were supplied by Sigma-Aldrich. Natural flakes of graphite powder and hydrazine were imported from Germany. These compounds were all of the analytical variety and were utilized without additional purification.

8.2.2 Materials synthesis, growth and fabrication of layered nanostructures

8.2.2.1 Preparation of P3HT

To create a solution with a 5% concentration, the P3HT was disseminated in chlorobenzene. A magnetic hot plate set at 80 °C was used to agitate the solution for 10 minutes. The temperature was reduced to 50 ℃ while the solution was constantly stirred for 1 hour, followed by cooling to room temperature.

8.2.2.2 Preparation of ZnO nanoparticles

The sol-gel process was used to prepare ZnO nanoparticles. The zinc supply was zinc acetate dihydrate, with methanol and MEA serving as the solvent and stabilizer, respectively. The 0.2 M zinc precursor solution was prepared by dissolving zinc acetate dehydrate in methanol. MEA was then added into the Zn solution where an equal volume ratio (1:1) was considered for Zn/MEA. The mixed solution was stirred using magnetic stirrer at 50 ℃ for 30 min. The transparent and homogenous solution was obtained after 72 hrs.

8.2.2.3 Preparation of GO nanoparticles

GO nanoparticles were prepared using graphite powder and potassium permanganate ($KMNO_4$) as starting materials following modified Hummer's method. In a typical preparation of GO, 2 g of graphite powder was dissolved in 46 ml of concentrated sulphuric acid (H_2SO_4) and stirred for 15 min in a cooled ice bath. 6 g $KMNO_4$ was slowly added to GO solution under vigorous stirring for 30 min. Finally, the GO solution was dispersed in 20 ml of H_2O_2. GO solution was then centrifuged at (4000 rpm) and repeatedly washed with 10 % hydrochloric acid (HCL) to remove the residual metal ions followed by washing with distilled (DI) water and the supernatant was discarded.

Transparent glass substrates were used for deposition of nanomaterials prior to studying their structural and optical properties. Identical layered nanostructures were grown on aluminium foil substrates in place of glass substrates for morphological and FTIR measurements. All substrates were cleaned ultrasonically with acetone, ethanol and deionized (DI) water, respectively for 10 min to remove contaminants from the surface and dried in an oven at 50 ℃ for 10 min prior coating. The solutions were then spin coated on to the glass substrates as shown in Figure 8.1 (a), using VTC-100 Vacuum Spin Coater. After deposition, the films were dried in an oven at 230 ℃ for 10 min to evaporate the solvent and remove organic residuals. Three sets of layered nanostructures are grown with the following designs and the final structure is well presented in Figure 8.1 (b): Film 1: Glass/P3HT, Film 2: Glass/ZnO/P3HT and Film 3: Glass/GO/ZnO/P3HT. Here we used P3HT as an active layer for absorbing photon energy from the sun. The ZnO layer in between serves as electron-transporting/hole blocking layer. This layer allows the efficient extraction and transfer of photo-induced electron to the GO layer.

8.2.2.4 Deposition process

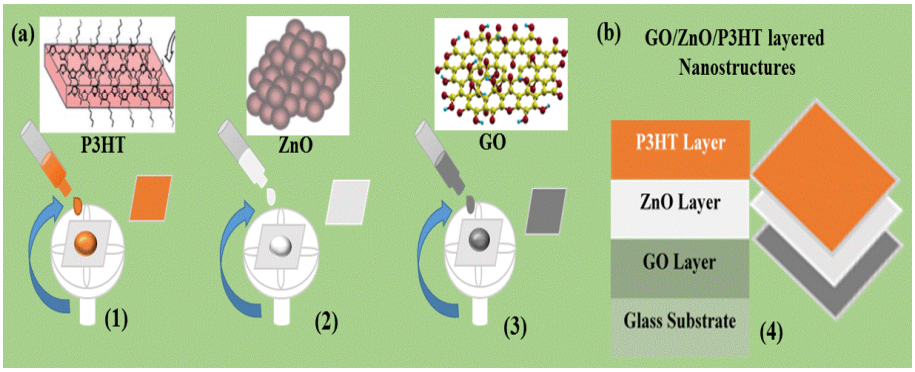

Figure 8. 1 Schematic (a) illustrating the growth of layered nanostructures (b) layered nanostructures on glass substrate depicting solar cell structure.

8.2.2.5 Device fabrication

Similar design was followed for fabrication of devices where layered nanostructures were deposited on an ITO coated glass. Prior deposition, substrates were cleaned sequentially as explained above before being treated with UV-ozone for 5 min. Different layers of ZnO and GO were deposited by spin-coating in the fume hood. P3HT solution was filtered using $0.45\mu m$ Polytetrafluoroethylene (PTFE) filter prior to spin-coating and was deposited inside a glove box. Finally, gold top electrode was evaporated in vacuum (10^{-6} mbar) using shadow masks that gives two active areas per substrate (~ 0.15 cm^2 each).

8.2.3 Materials and device characterization

The crystallite phases of the layered nanostructures were identified using Rigaku Smart Lab diffractometer in a wide-angle X-ray diffraction mode with CuKα (1.5418 Å) radiation at a scanning rate of 0.005 degree (2θ/s). Surface morphology measurements were recorded using field emission scanning electron microscope (FESEM), model JSM-7800F FESEM JEOL Ltd. coupled with an Ultra Dry EDS detector. Functional groups and structural information were studied using PerkinElmer FTIR spectrometer in the wavenumber region 400 - 4000 cm^{-1} in specular transmittance mode. The steady state absorption measurements were acquired in the 200 - 900 nm wavelength range using a PerkinElmer Lambda spectrometer, model 1050 UV/VIS/NIR, equipped with integrated sphere in absorbance mode. Luminescence measurements were acquired using a Horiba Jobin Yvon Fluorolog tunable-photoluminescence (PL) spectrofluorometer system. The performance of fabricated solar cell devices was evaluated in the dark and under illumination using the current density-voltage (J-

V) features with Keithley model 2400 digital source meter by providing independent external voltage to the cell while measuring the photogenerated current. The voltage was swept between -0.5 to 0.5 V at a voltage interval of 0.01 V with the current limit fixed at 2.5 A. The spectral mismatch between the emission of the solar simulator (NEWPORT class A, 1 600 W) and the global AM1.5G solar spectrum (IEC 60904-3 Ed.2) was corrected using a mismatch factor and the solar simulator irradiance was adjusted accordingly using a certified silicon reference cell in order to achieve an equivalent AM1.5G irradiance of one sun (100 $mW\,cm^{-2}$) on the test cells.

8.3 Results and Discussion

8.3.1 XRD analysis

The XRD patterns shown in Figure 8.2 (a) depict the out-of-plane crystal structure of P3HT, ZnO and GO layers deposited on separate substrates. For P3HT layer, the pattern is dominated by a diffraction peak at 2θ = 5.36° along the (100) orientation [13].

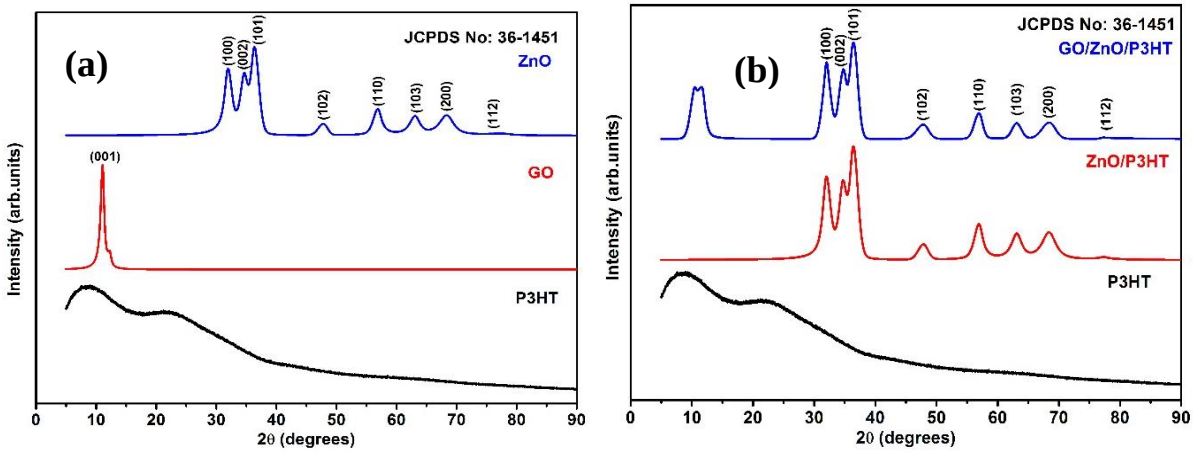

Figure 8. 2 (a) XRD patterns of P3HT, GO and ZnO film layers, (b) P3HT, P3HT/ZnO and P3HT/ZnO/GO layered nanostructures.

The GO layer shows a strong (001) peak at 2θ = 11.1° which signals the existence of oxygen functional group which alleviate the exfoliation and hydration of graphene sheets in aqueous media [14]. Then we have the ZnO layer with characteristic diffraction peaks that are representative of the (100), (002), (101), (102), (110), (103), (200) and (112) planes of its hexagonal wurtzite structure [15]. These set of planes matched with the patterns of hexagonal wurtzite ZnO with a standard file indexed by JCPDS 36-1481.

Figure 8.2 (b) presents XRD patterns of P3HT, ZnO/P3HT and GO/ZnO/P3HT layered nanostructures. The XRD pattern of ZnO/P3HT only shows the existence of ZnO hexagonal phase. This is due to complex microstructure of P3HT consisting of network of crystalline but dominated by amorphous domains. Thus, what causes broader and less intense diffraction in P3HT is not fairly crystals but superstructures having certain ordering. For GO/ZnO/P3HT the diffraction peaks from ZnO were observed, and within its wurtzite symmetry there is (001) GO reflection. Herein, one can see that there is a splitting and broadening in the (001) GO peak, presumably due to increase in carbon to oxygen ratio upon covalent interaction with ZnO and polymer. The broadening of GO peak may be induced by greater polar-polar interaction of oxygen containing groups of GO and the polar parts of nanoparticles, with possible formation of hydrogen bonds to provide greater stability of the layered nanostructures [16]. Pristine GO showed interlayer distance of 0.79 nm and the growth of GO/ZnO/P3HT nanostructure revealed shift in (001) reflection of GO to 2θ = 11.0° corresponding to interlayer distance of 0.80 nm. It is evident that the shift in diffraction peaks to low diffraction angles lead to the increase in d-spacing as ZnO is restructured. The improvement of the interlayer distance within GO planes is ascribed to the intercalation of oxygen functional groups into GO layers [17]. The average crystallite size of ZnO, ZnO/P3HT and GO/ZnO/P3HT layered nanostructures was estimated using well known Debye Scherrer's equation presented in equation (8.1) [18, 19].

$$D = \frac{K\lambda}{\beta \cos\theta} \qquad 8.1$$

The estimated average crystallite sizes were 4.54, 4.51 and 4.50 nm respectively, confirming the nano property of layered structures. The observed decrease in crystallite size behaviour relates to broadening of diffraction peaks when growing ZnO with other nanostructures. The obtained smaller sized crystallites conform with higher surface to volume ratio and provide higher probability of GO/ZnO/P3HT nanoparticles distributed all over the substrate for enhanced photon absorption.

8.3.2 SEM analysis

It is widely acknowledged that morphology plays a crucial role when targeting solar cell devices for their performance. The surface morphology of all the P3HT, ZnO, GO and layered nanostructures are depicted in Figure 8.3. FE-SEM analysis measurements were undertaken carefully on P3HT, ZnO and GO deposited on individual substrates.

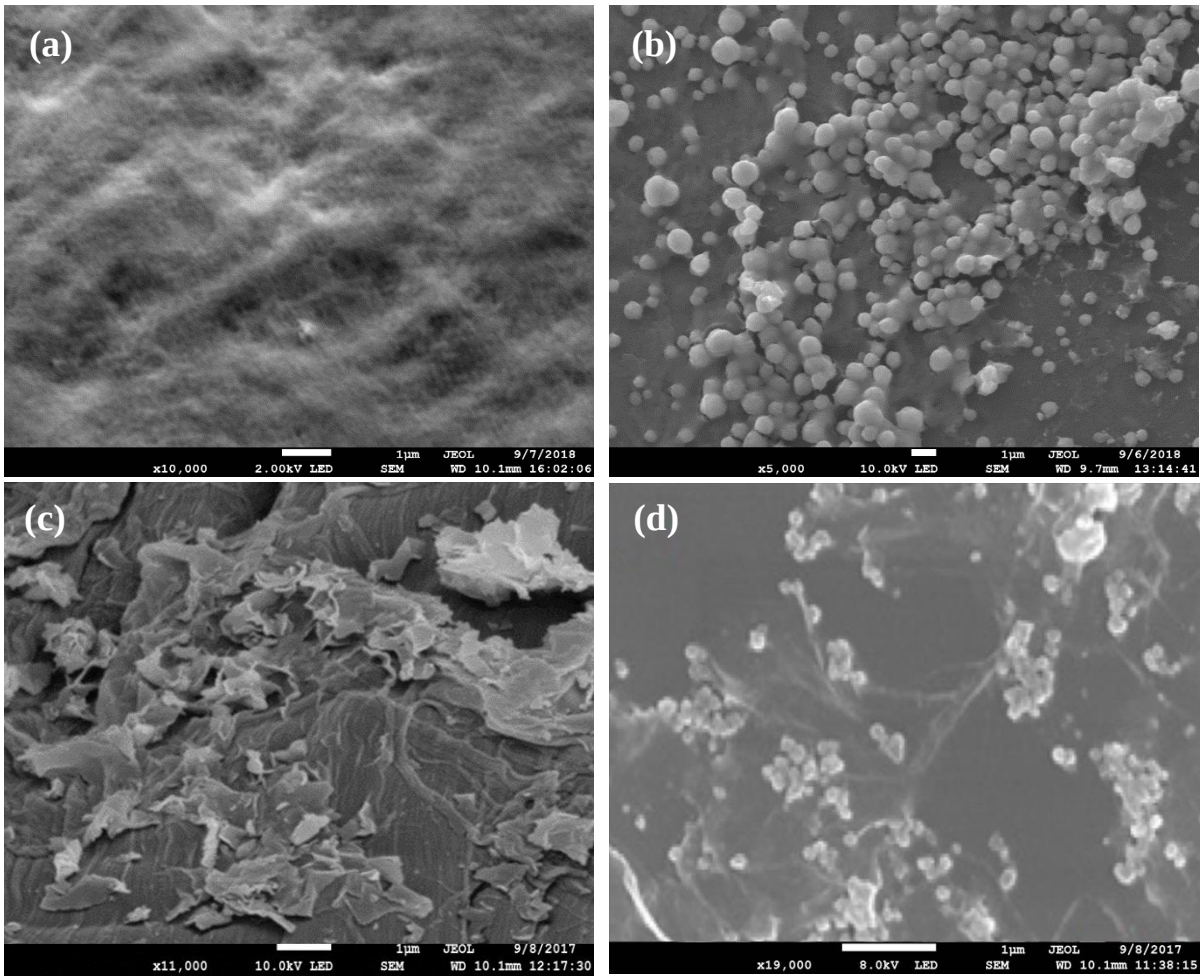

Figure 8. 3 SEM images of (a) P3HT, (b) ZnO (c) GO and (d) GO/ZnO/P3HT layered nanostructures.

Figure 8.3 (a) presents the SEM image of P3HT quite uniformly distributed on the substrate. For ZnO nanoparticles in Figure 8.3 (b), we observed small nanospheres with different sizes distributed unevenly. These nanospheres are highly agglomerated in other areas of this morphology while others are randomly distributed. Those agglomerated nanospheres will facilitate larger interface area between ZnO/P3HT layers leading to enhanced exciton dissociation and photo response. Figure 8.3 (c) shows the morphology of GO nanoflakes revealing some aggregation of wrinkled nanosheets with crimps at the edges. On the other regions we observed graphene sheets overlapped with the neighbouring ones forming plate-like morphology due to strong $\pi - \pi$ stacking interactions between GO sheets. Han *et al.* [20] indicated that the wrinkled GO sheets are associated with dynamical annealing and one can initially dry in air to obtain wrinkle-free GO films. Paulchamy *et al.* [21] exhibited a porous network of well-defined and connected three-dimensional graphene sheets that resembled a loose sponge-like structure. In Figure 8.3 (d) we have GO/ZnO/P3HT layered nanostructures

which shows disordered ZnO nanospheres covalently bonded to GO sheets. It is evident that ZnO nanospheres are intercalated into the GO sheets.

8.3.3 EDS analysis

The chemical stoichiometry of GO/ZnO/P3HT layered nanostructures are presented in Figure 8.4. The layered nanostructure consists of carbon (C), oxygen (O), and zinc (Zn) elements that originates from GO, ZnO and P3HT compounds used during growth of the layered nanostructure. Additionally, the peak of nickel (Ni) and aluminum (Al) in the composition comes from the aluminum foil substrate used for morphological and compositional analysis. Other than that, we observed no elements suggesting presence of impurities.

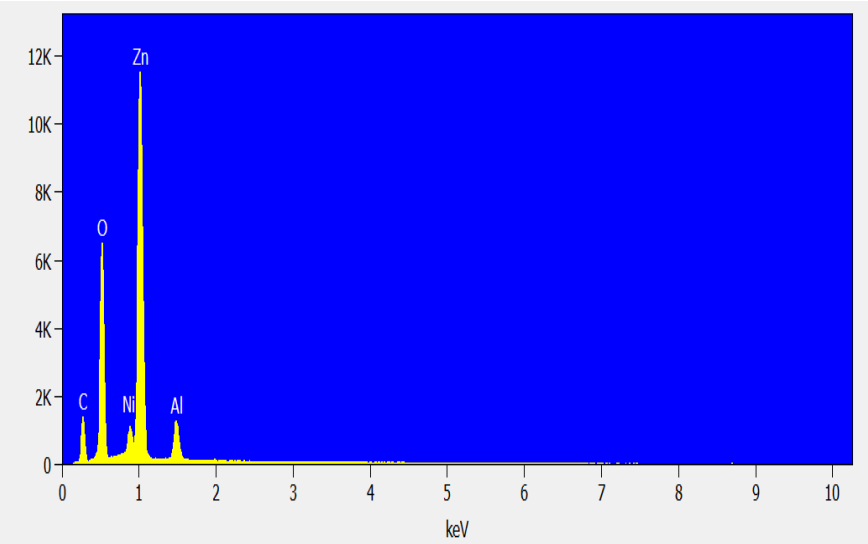

Figure 8. 4 EDS spectrum of GO/ZnO/P3HT layered nanostructures.

8.3.4 FTIR analysis

The FTIR spectra of P3HT, ZnO/P3HT and GO/ZnO/P3HT are presented in Figure 8.5. The pristine P3HT is dominated by well-known bands located at ~ 2960, ~ 2925 and ~ 2850 cm^{-1} which corresponds to aliphatic C-H stretching of P3HT [22]. At ~ 1456 and ~ 826 cm^{-1} there are prominent bands assigned to the C-H vibration band and in-plane symmetric deformation of CH_3, respectively [23].

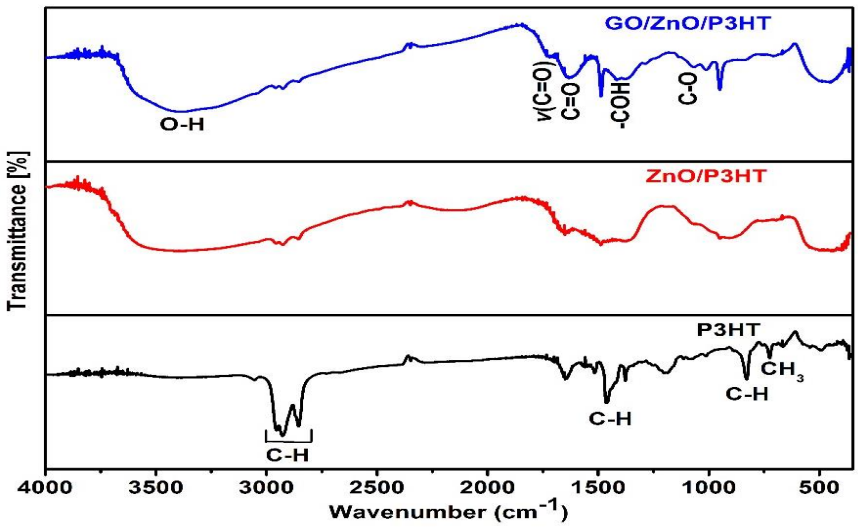

Figure 8. 5 FTIR spectra of P3HT, ZnO/P3HT and GO/ZnO/P3HT layered nanostructures.

The spectra further show a band at 1375 cm^{-1} which relates to bending vibrations of $–CH_2–$. The peak and band with low intensity between ~ 1260 and ~ 1040 cm^{-1} are ascribed to C-H in-plane bending and the dipole derivative vector that is vertical to the ring plane [24]. A sharp CH_3 band located at 723 cm^{-1} associated with CH_3 rocking also assigned to methyl rock mode was observed. Our results show correlation with FTIR reports on P3HT from previous studies.

From FTIR spectra of ZnO/P3HT we observed signals associated with C-H from P3HT, indicating that growing P3HT layer on ZnO results in chemical reactions. The intensity of various vibrations of P3HT chains were decreased due to the presence of ZnO nanostructures. The main differences in the layered nanostructure are observed in the finger print region i.e. below 1000 cm^{-1} due to interatomic vibrations of metal oxides [25]. In the region 450-600 cm^{-1} a broad band is observed consisting of the frequency vibrations corresponding to stretching modes of ZnO [26]. The C-O bond at 1081 cm^{-1} is ascribed to the stretching modes which verifies the existence of oxide functional groups. Furthermore, there is a usual band that represent stretching of hydroxyl. The absorbed water within ZnO/P3HT layered nanostructures, is shown by broad peak between 3700 – 3150 cm^{-1} indicating O-H stretching of H_2O molecules.

The chemical changes occurring upon growing GO layer can be observed indicating that its sheets have been anchored by the matrix of P3HT and ZnO nanoparticles through noncovalent bonding. We say this based on clarity by Lonkar *et al.* [27] stating that the surface of GO is very vast and atomically flat, providing a platform for the anchoring of

diverse chemical species. These happens through secondary interactions, which does not change the structural integrity leading to preserved electronic conductivity as a prerequisite. The main absorption band in FTIR of layers including GO reveals stretching band at 1720 cm^{-1} attributed to carboxyl groups v(C=O) vibrational formation C=O carbonyl at 1727 cm^{-1}, O-H at [28]. Ghoreishi *et al.* [29] attributed C=O band at 1632 cm^{-1} to the skeletal vibrations of unoxidized graphitic domains. Then we also have absorbance band of in-plane -COH band at 1400 cm^{-1} indicating high oxidation of graphite. Manifolds of stretching bands for C-O bonds from COOH were observed in the range 1068-750 cm^{-1}. These bands confirm the occurrence of oxide functional groups after the oxidation process [21]. Within that range we saw band emerging at ~ 947 cm^{-1} presumed to indicate charge transfer complexes arising between nanostructures. Moreover, charge transfer is witnessed by shifting of the ~ 1456 cm^{-1} to the higher wavenumber region for ZnO/P3HT and GO/ZnO/P3HT layered nanostructures. Mkawi *et al*. [24], also reported on the redshift of C-H stretching mode indicative of charge transfer after doping P3HT: PCBM blend with nanoparticles.

The isolated hydroxyl group of intercalated water in GO/ZnO/P3HT layer at ~ 3417 cm^{-1} is much bigger than that of ZnO/P3HT indicating that the graphite was heavily oxidized. This emphasizes how incredibly absorbent GO is, as seen by its capacity to create gel-like solutions. However, most oxygen functional groups observed in ZnO/P3HT appear with significantly higher intensities in the spectra of GO/ZnO/P3HT layered nanostructures. Additionally, the characteristic peaks of P3HT were observed in the region 2960 – 2850 cm^{-1} with significant reduction in intensity. These findings demonstrate that there was no covalent connection between the stacked nanostructures, instead a simple π-π stacking, which caused a reduction in vibrational response of the P3HT moiety [30]. This correlates with a decrease in crystallinity observed during XRD analysis after growth of other layered nanostructures.

8.3.5 UV-Vis analysis

Figure 8.6 (a) presents the UV/VIS/NIR absorption spectra of P3HT, P3HT/ZnO and P3HT/ZnO/GO layered nanostructures. The P3HT layered nanostructure reveals the capability to absorb more light in the visible range of the electromagnetic spectrum.

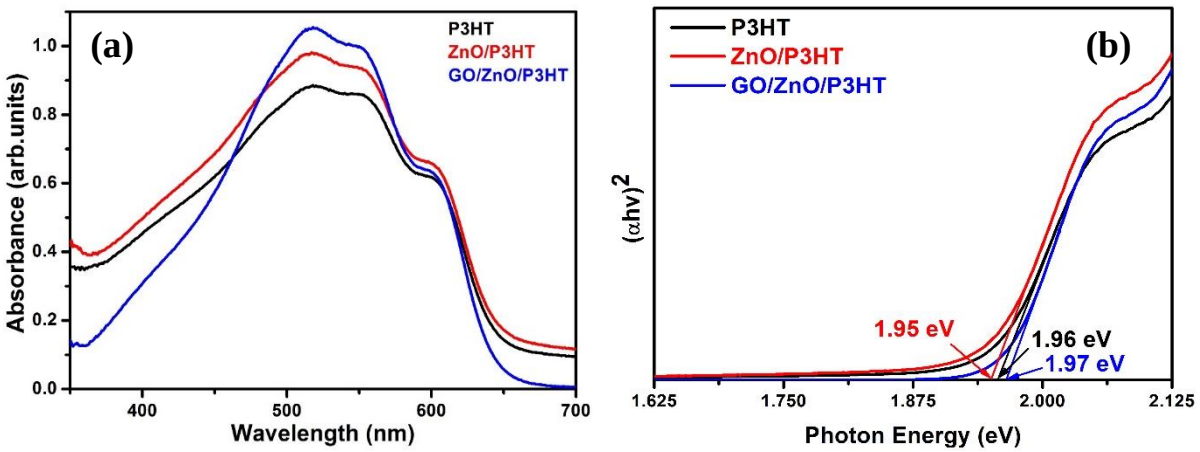

Figure 8. 6 (a) Steady state absorption spectra, (b) Tauc's plot of P3HT, ZnO/P3HT and GO/ZnO/P3HT layered nanostructures.

Three absorption peaks at ~ 518, ~ 552 and ~ 601 nm were observed which originate from the electronic transitions and the interchain interactions [31]. The highest absorption is observed at ~ 518 nm. However, mutation of P3HT is observed where there is an increase in absorption upon growing ZnO/P3HT with further increase for GO/ZnO/P3HT. These indicates an increase in absorption corresponding to transition from valance to conduction band. The enhancement in absorption emanates from structural defects brought by ZnO and GO, which reduces the intra-chain orders leading to the increase in absorption [32]. Furthermore, multilayered nanostructures revealed absorption shift towards the higher wavelength region. The redshift symbolizes the enhancement in semiconductor characteristic features of P3HT as GO and ZnO affect the π-π^* absorption band of P3HT polymer molecules [33]. It can be deduced that photovoltaic properties of GO/ZnO/P3HT layered nanostructures could be improved with intense absorbance that increases the light harvesting efficiency. Figure 8.6 (b) shows the optical bandgap of the layered nanostructures estimated using Tauc's plot [34]. The energy bandgap values were obtained by extrapolating linear part of $(\alpha h\nu)^2$ with $h\nu$ plot to $\alpha = 0$. The variation in energy bandgap is marginal where for P3HT we obtained ~ 1.96 eV while ZnO/P3HT and GO/ZnO/P3HT are ~ 1.95 and ~ 1.97 eV, respectively.

8.3.6 PL analysis

The excitation dependence was conducted as shown in Figure 8.7, 8.8 and 8.9 using 3-D PL emission spectra and the corresponding 2-D contour map. These measurements assisted to investigate the presence of different emissive states in Figure 8.7 for P3HT, Figure 8.8 for ZnO/P3HT and Figure 8.9 for GO/ZnO/P3HT layered nanostructures, respectively.

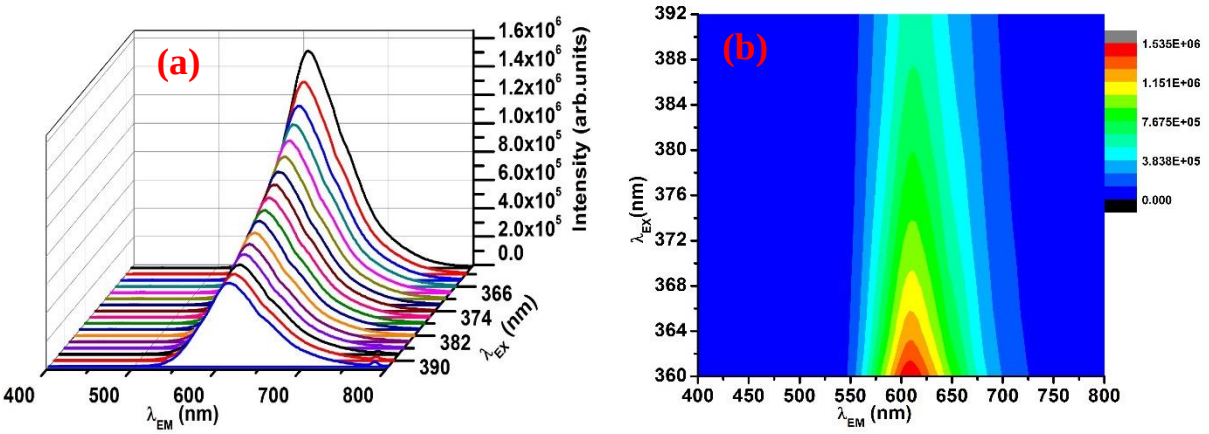

Figure 8. 7 (a) 3-D PL emission spectra, (b) 2-D contour map profile of P3HT layered nanostructure.

In Figure 8.7 (a) we have noted a gradual drop in emission intensity of P3HT upon increasing the excitation wavelength which symbolizes the excitation-based charge transfer where luminescence signal is strong at high energy excitation. This shows that at low excitation wavelength the carriers acquire the necessary energy for the radiative recombination while the increase in excitation wavelength disrupts the carries [35]. Figure 8.7 (b) illustrates the contour map dominated by blue color between 400 nm to 550 nm and 725 nm to 800 nm at various excitation wavelengths. The map shows that P3HT is emissive in the range 550 – 725 nm with the optimum emission at ~ 620 nm obtained at low excitation wavelength. The emergence of varying colors with the increase in excitation denotes areas of low emission intensity.

Figure 8.8 (a) demonstrates ZnO/P3HT nanostructures acquired at different excitations where we witnessed a monotonic increment of emission intensity upon increasing excitation values.

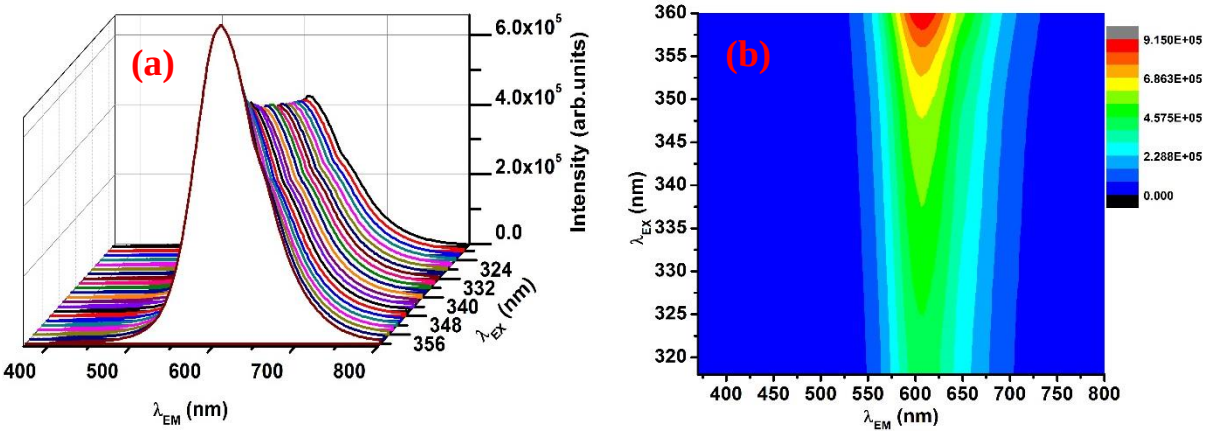

Figure 8. 8 (a) 3-D PL emission spectra (b) 2-D contour map profile of ZnO/P3HT layered nanostructures.

It is worth noting that the growth of ZnO with P3HT brought the inverse of what we observed in Figure 8.7 (a). Herein, with the highest excitation, the optimal emission was attained. The shape of the emission spectra is similar to that of pristine P3HT which indicates no distinct peak corresponding to ZnO. This shows that P3HT defects surpassed those of ZnO due to lack of energy transfer from P3HT to ZnO when varying the excitation wavelength [36].

It is evident from Figure 8.8 (b) that the contour map of ZnO/P3HT nanostructures irradiated at different wavelengths differs from pristine counterpart. The increase in excitation led to the emersion of various colors in the same wavelength range suggesting the increase in intensity.

Figure 8.9 (a) shows the emission variations on GO/ZnO/P3HT layered nanostructures acquired at various excitation wavelengths. Upon increasing the excitation wavelength, we observed a gradual increase in luminescence intensity. The emission reached the highest intensity when excited at 356 nm and thereafter began to quench. The PL quenching with the increase in excitation (λ_{ex} > 356 nm) can be attributed to low optical absorption in the range 350 – 450 nm as seen in the absorption spectrum of GO/ZnO/P3HT layered nanostructures. A detailed view of variation in intensity is presented on the contour map in Figure 8.9 (b). The contribution of GO is observed via the broadening of the emission (475 – 725 nm) contrary to the counterparts (550 – 725 nm). The observed broadening concomitant the increase in intensity testifies that GO increased concentration of defects (emission centers).

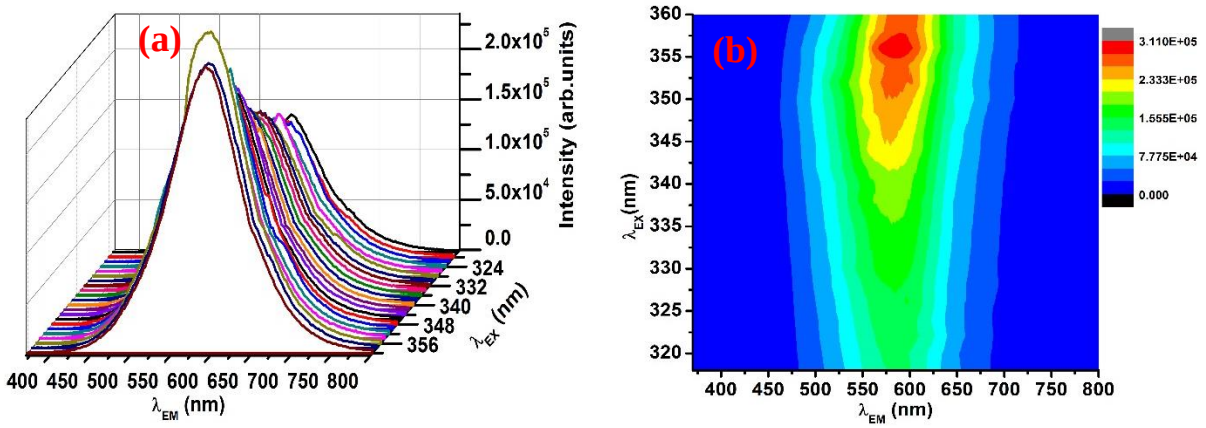

Figure 8. 9 (a) 3-D PL emission spectra (b) 2-D contour map profile of GO/ZnO/P3HT layered nanostructures.

The inset in PL spectra shown in Figure 8.10 is a spectrum of pristine ZnO acquired at 320 nm excitation to confirm the applicable defects. The spectrum reveals a UV near band emission (NBE) at ~ 380 nm and a visible broad deep level emission (DLE) at ~ 550 nm. For

sol-gel derived ZnO, the chemical composition of ZnO nanoparticles is nonstoichiometric and it contains excess Zn atoms and oxygen vacancies, indicating lattice flaws and surface defects. These defects act as non-radiative centres and reduce light emission hence we saw weak UV and strong visible emission. The observed UV emission is ascribed to exciton-related recombination of ZnO [37]. The green emission at 550 nm is said to arise from intrinsic defects of ZnO with oxygen vacancies accepted to be the main contributor [38].

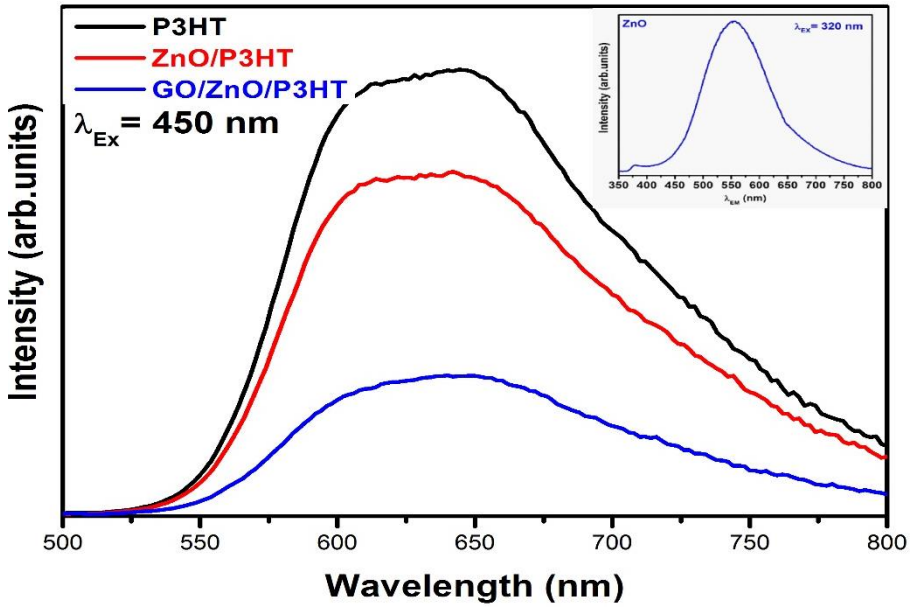

Figure 8. 10 PL emission spectra of P3HT, ZnO/P3HT and GO/ZnO/P3HT layered nanostructures.

The PL spectra of the P3HT, ZnO/P3HT and GO/ZnO/P3HT layered nanostructures are shown in Figure 8.10 for determination of electronic interaction between the layers. An emission of P3HT in the range 525 – 800 nm has two peaks at positions ~ 612 and ~ 650 nm which are commonly assigned to the transitions between the vibrational energy levels (0-0) and (0-1) [39]. The growing of ZnO layer with P3HT yields a decrease in relative intensity of the two characteristic peaks. Further reduction in intensity is observed for GO/ZnO/P3HT and is indicative of the degree of intermolecular interaction between the layered nanostructures which changes the conformation of P3HT chains [40]. The drastically quenched emission shows that efficient exciton dissociation happens at the interface of layered nanostructures. The quenching behaviour is due to fast photoinduced charge transfer from P3HT to GO through Zn at the donor/acceptor interfaces [6]. This supports the work of Chawla *et al.* [41] who showed that the optimum charge transfer agents for P3HT-based heterostructures are the acceptor materials that most help to reduce the fluorescence intensity

of P3HT. Moreover, we observed a slight blue shift of the emission peaks upon growing ZnO and GO layers due to the alteration of P3HT crystalline order [42].

The electron transfer process is evaluated by determination of the quenching efficiency parameter η using equation (8.2) [43]:

$$\eta = 1 - (I / I_0) \tag{8.2}$$

where I_0 and I represents the integrated PL intensities of the donor (P3HT) prior and after growth of the accepter of electrons. The obtained η values are ~ 0.23 and ~ 0.69 indicating the electron transfer process improved with the growth of multilayers due to large specific surface area of GO. In addition, there is an overlap between emission spectrum of P3HT located in the range 550 – 750 nm and the electronic absorption of layered nanostructures acquired in the range 400 – 650 nm indicative of resonance energy transfer process.

8.3.7 IV analysis

To ensure success in fabrication of a working solar cell device three parameters were evaluated: The open-circuit voltage (V_{OC}), the short circuit current density (J_{SC}) and the fill factor (FF). Table 8.1 summarizes the aforementioned photovoltaic parameters of the organic solar cells (OSCs) and the PCE calculated from the current density versus voltage (J-V) spectra in Figure 8.11 acquired under solar illumination.

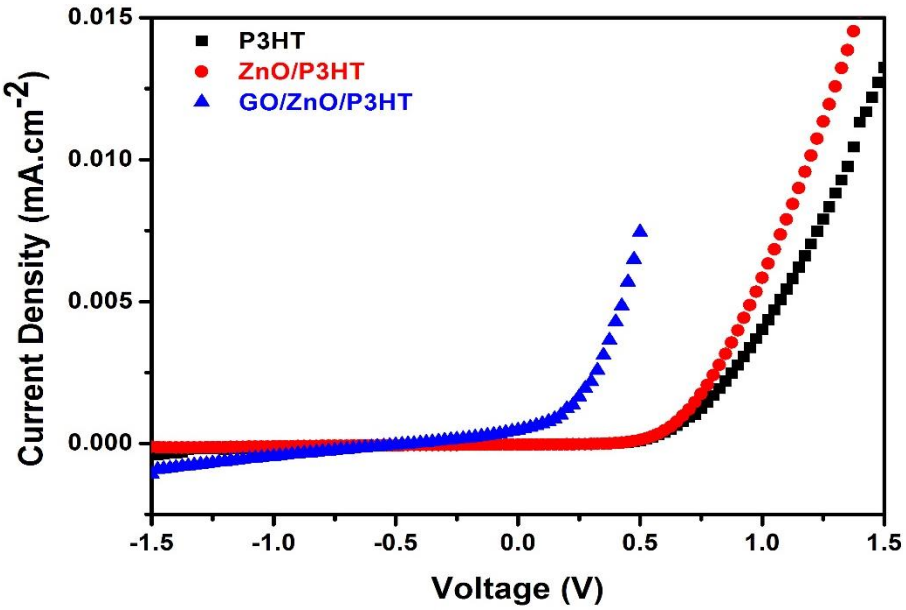

Figure 8. 11 I-V characteristics of P3HT, ZnO/P3HT and GO/ZnO/P3HT devices under light illumination.

As presented in Figure 8.11, from a device constructed using only P3HT as an active layer we obtained an efficiency of 0.0208 %. However, the incorporation of ZnO for the formation of ZnO/P3HT device amplified the V_{OC}, J_{Sc} and FF parameters which resulted in the optimum PCE. The device based on GO/ZnO/P3HT experienced a decrease in V_{OC} and FF hence the reduction in efficiency. It has been reported that the V_{OC} of bulk heterojunction (BHJ) polymer solar cells (PSC) decreases with higher donor/acceptor interfacial area [44]. However, both devices witnessed the enhancement in J_{SC} due to the charge-separation effect that appeared at their band alignment. It is worth noting that the highest FF for ZnO/P3HT device resemble the efficient and effective energy conversion system.

Table 8.1: Photovoltaic parameters of P3HT, ZnO/P3HT and GO/ZnO/P3HT solar devices.

Device structure	V_{OC} (V)	J_{SC} (mA/cm^2)	FF (%)	η (%)
ITO/P3HT/Au	0.303	0.206	0.332	0.0208
ITO/ZnO/P3HT/Au	0.361	0.231	0.481	0.0402
ITO/GO/ZnO/P3HT/Au	0.172	0.394	0.247	0.0167

According to the conventional theory on charge transportation in the organic semiconductors, the more ordered or crystalline thin films should have the higher charge carrier mobility than their less ordered counterparts [45]. This explains the reduction in efficiency upon incorporating GO which is due to the reduced intergrain transport insinuating poor connectivity between the grains and the increased number of insulating grain boundaries. The poor performance was caused by the hydrophobic property of GO and its low conductivity.

8.4 Conclusion

Layered nanostructures were successfully grown using materials prepared based on simple growth processes. The XRD results showed amorphous nature of P3HT and the diffraction peaks of ZnO and GO were well pronounced. The absorption measurements revealed greater light absorption for GO/ZnO/P3HT layered nanostructures. From FTIR we saw remarkable interactions at the GO/ZnO/P3HT interface. PL showed enhanced charge transfer through the quenching of PL intensity and the increase in quenching efficiency factor. The attained photovoltaic parameters signify an improvement in the efficiency for ZnO/P3HT device contrary to which GO/ZnO/P3HT device resembled a drastic decline in the efficiency due to low conductivity of GO.

8.5 References

[1] E. Placzek-Popko, Top PV market solar cells 2016, *Opto-Electronics Reviews*, **25** (2017) 55-64.

[2] K. Yang, C. Xu, L. Huang, L. Zou and H. Wang, ZnO nanotubes grown on reduced graphene oxide, *Nanotechnology* **22** (2011) 405401.

[3] K.S. Novoselov, A.K. Geim, S.V. Morozov, D. Jiang, Y. Zhang, S.V. Dubonos, I.V. Grigorieva, A.A. Firsov, *Science*, **306** (2004) 666-669.

[4] M. Acik, G. Lee, C. Mattevi, A. Pirkle, R.M. Wallace, M. Chhowalla, K. Cho and Y. Chabal, The role of oxygen during thermal reduction of graphene oxide studied by infrared absorption spectroscopy, *J. Phys. Chem. C*, **115** (2011) 19761-19781.

[5] S.D. Dabhi and P.K. Jha, Tuning of electronic properties and dynamical stability of graphene oxide with different functional groups, *Physica E* **93** (2017) 332-338.

[6] Y. Wang, S. Yang, H. Wang, L. Zhang, H. Cheng, B. He, W. Li, B. Zou, Surfactant-treated graphene oxide in organic solvents and its application in photovoltaic cells, *Current Applied Physics*, **17** (2017) 343-350.

[7] M.I. Ahmed, Z. Hussain, M. Mujahid, A.N. Khan, S.S. Javaid and A. Habib, Low resistivity ZnO-GO electron transport layer based $CH_3NH_3PbI_3$ solar cells, *AIP Advances*, **6** (2016) 065303-1 – 065303-13.

[8] F.V. Molefe, L.F. Koao, J.J. Dolo, B.F. Dejene, Effect of reaction time on structural, morphology and optical properties of ZnO nanoflakes prepared by chemical bath deposition method, *Physica B,* **439** (2014) 185-188.

[9] M.F. Ahmed and I.A. Hümmelgen, Determination of Electron and Hole Mobility in Poly(3-hexylthiophene) Using Space-Charge-Limited-Current Measurements, *Int. J. Electroactive Mater.* **1** (2013) 60-63.

[10] A. Hayakawa, O. Yoshikawa, T. Fujieda, K. Uehara and S. Yoshikawa, High performance polythiophene/fullerene bulk-heterojunction solar cell with a TiO_x hole blocking layer, *Appl. Phys. Lett.* **90** (2007) 163517.

[11] J. Gilot, I. Barbu, M.M. Wienk and R.A.J. Janssen, The use of ZnO as optical spacer in polymer solar cells: theoretical and experimental study, *Appl. Phys. Lett.* **91** (2007) 113520.

[12] J. Gilot, M. M. Wienk, R. A. J. Janssen, Double and triple junction polymer solar cells processed from solution, *Appl. Phys. Lett.* **90** (2007) 143512.

[13] P. Aruna, S.M. Naveena and C.M. Joseph, Color sensing ability of spin coated poly(3-

hexylthiophene-2, 5-diyl) thin films.

[14] N.S. Suhaimin, M.F.R. Hanifah, M. Azhar, J. Jaafar, M. Aziz, A.F. Ismail, M.H.D. Othman, M.A. Rahman, F. Aziz, N. Yusof and R. Mohamud, The evolution of oxygen-functional groups of graphene oxide as a function of oxidation degree. *Mater. Chem. Phy.* **278** (2022) 125629.

[15] P. Pachamuthu, A.P. Jeyakumari, N. Srinivasan, R. Chandrasekaran, K. Revathi and P. Karuppannan, Structure, Surface analysis and bioactivity of Mn doped zinc oxide nanoparticles, *Journal of the Indian Chemical Society* **99** (2022) 100342.

[16] P. Bhawal, S. Ganguly, T.K. Chaki and N.C. Das, Synthesis and characterization of graphene oxide filled ethylene methyl acrylate hybrid nanocomposites, *RSC Adv.* **6** (2016) 20781-20790.

[17] M. El Achaby, F.Z. Arrakhiz, S. Vaudreuil, E.M. Essassi and A. Qaiss, Piezoelectric *β*-polymorph formation and properties enhancement in graphene oxide - PVDF nanocomposite films, *Appl. Surf. Sci.* **258** (2012) 7668-7677.

[18] B.D. Cullity, Elements of X-Ray Diffraction, 2nd edn. (Addition-Weasley, London, 1978).

[19] F.V. Molefe, L.F. Koao, B.F. Dejene and H.C. Swart, Phase formation of hexagonal wurtzite ZnO through decomposition of $Zn(OH)_2$ at various growth temperatures using CBD method, Opt. Mater. **45** (2015) 292-298.

[20] F. Han, S. Yang, W. Jing, Z. Jiang, H. Liu, L. Li, A study on near-UV blue photoluminescence in graphene oxide, prepared by Langmuir–Blodgett method, Applied Surface Science 345 (2015) 18–23.

[21] B. Paulchamy, G. Arthi and B.D. Lignesh, A Simple Approach to Stepwise Synthesis of Graphene Oxide, Nanomaterial, J. Nanomed. Nanotechnol. 6 (2015) 1-4.

[22] D. Yu, S.Y. Yang, M. Durstock, J.B. Baek and L.M. Dai, *ACS Nano*, 4 (2010) 5633–5640.

[23] C. Uludag, E. Alveroglu, K. Koc, Y. Karabul, M. Kilic and Z.G. Ozdemir, Dielectric properties of P3HT/CSA composites for energy applications. *Physica B* **626** (2022) 413508.

[24] E.M. Mkawi, Y. Al-Hadeethi, R.S. Bazuhair, A.S. Yousef, E. Shalaan, B. Arkook, A.M. Abdel-Daiem and E. Bekyarova, Fabricated Cu_2ZnSnS_4 (CZTS) nanoparticles as an additive in P3HT: PCBM active layer for efficiency improvement of polymer solar cell, *J. Lumin.* **240** (2021) 118420.

[25] M. Hamzah, R.M. Ndimba, M. Khenfouch and V.V. Srinivasu, Blue luminescence

from hydrothermal ZnO nanorods based PVA nanofibers, *J. Mater. Sci. Mater. Electron*. 28 (2017) 11915-11920.

[26] S.J. Mofokeng, V. Kumar, R.E. Kroon, O.M. Ntwaeaborwa, Structure and optical properties of Dy^{3+} activated sol-gel ZnO-TiO_2 nanocomposites, J. Alloys Comp. 711 (2017) 121-131.

[27] S.P. Lonkar, Y.S. Deshmukh and A.A. Abdala, Recent advances in chemical modifications of graphene, *Nano Research* 8 (2015) 1039-1074.

[28] M. Khenfouch, U. Buttner, M. Baitoul, M. Maaza, *Graphene* 3 (2014) 7-13.

[29] F.S. Ghoreishi, V. Ahmadi and M. Samadpour, Synthesis and Characterization of Graphene-ZnO Nanocomposite and its Application in Photovoltaic Cells, *JNS* 3 (2013) 453-459.

[30] V. Saini, O. Abdulrazzaq, S. Bourdo, E. Dervishi, A. Petre, V.G. Bairi, T. Mustafa, L. Schnackenberg, T. Viswanathan, A.S. Biris, Structural and optoelectronic properties of P3HT-graphene composites prepared by in situ oxidative polymerization, *J. App. Physics* **112** (2012) 054327-1 - 054327-9.

[31] J. Wang, W. Tao, J. Sun, F. Wang, Y. Lian, K. Zhang, W. Wu and B. Guo, Polaron lifetime enhancement of P3HTthin film under femtosecond laser irradiation and its ultrafast mechanism, *Optics and Laser Technology* **153** (2022) 108191.

[32] J. Clark, C. Silva, R.H. Friend and F.C. Spano, *Phys. Rev. Lett.* 98 (2007) 206406.

[33] A. Benchaabane, M.E. Hajlaoui, N. Hnainia, A. Al-Tabbakh, A. Zeinert and H. Bouchriha, Optical properties enhancement of hybrid nanocomposites thin films based on P3HT matrix and ZnO@SiO_2 core-shell nanoparticles, *Opt. Mater.* **102** (2020) 109829.

[34] P.R. Jubu, O.S. Obaseki, A. Nathan-Abutu, F.K. Yam, Y. Yusof and M.B. Ochang, Dispensability of the conventional Tauc's plot for accurate bandgap determination from UV-vis optical diffuse reflectance data, *Results in Optics* **9** (2022) 100273.

[35] T. Hidouri, H. Saidi, C. Amri, F. Saidi and A. Bouazizi, Effect of wavelengths and excitation density on the optical properties of P3HT: SiNWs bulk heterojunction for photovoltaic applications, *Superlattices and Microstructures* **97** (2016) 409-416.

[36] S. Dey and A.K. Kar, Composition and excitation wavelength dependent photoluminescence color tuning in nanocomposite of PMMA and ZnO nanorods for PLED, *J. Alloys Comp.* **879** (2021) 160450.

[37] F. Han, S. Yang, W. Jing, K. Jiang, Z. Jiang, H. Liu and L. Li, Surface plasmon enhanced photoluminescence of ZnO nanorods by capping reduced graphene oxide

sheets, *Optics Express*, **22** (2014) 11436-11445.

[38] N. Kumar and A. Srivastava, Green photoluminescence and photoconductivity from screen-printed Mg doped ZnO films, *J. Alloys Compd.* **735** (2018) 312-318.

[39] A. Bakour, O. Bajjou, M. Baitoul, F. Massuyeau, J. Wéry, M. Maaza and E. Faulques, A study of the temperature effect on photoluminescence of the P3HT/ MWNT nanocomposites, *Materials Today: Proceedings* **36** (2021) 549-552.

[40] A.R. Inigo, Y.F. Huang, J.D. White, Y.S. Huang, W.S. Fann, K.Y. Peng and S.A. Chen, Review of morphology dependent charge carrier mobility in MEH-PPV, *J. Chin. Chem. Soc.* **57** (2010) 459-468.

[41] P. Chawla, S. Singh and S.N. Sharma, *Beilstein J. Nanotechnol.* **5** (2014) 1235.

[42] G.L. Kabongo, P.S. Mbule, G.H. Mhlongo, B.M. Mothudi, K.T. Hillie and M.S. Dhlamini, Photoluminescence Quenching and Enhanced Optical Conductivity of P3HT-Derived Ho^{3+}-Doped ZnO Nanostructures. *Nanoscale Research Letters* 11 (2016) 1-11.

[43] Bkakri, R.; Kusmartseva, O. E.; Kusmartsev, F. V.; Song, M.; A. Bouazizi.; *J. Lumin.* **161** (2015) 264-270.

[44] F. Zheng, X.-Y. Yang, P-.Q. Bi, M-.S. Niu, C-.K. Lv, L. Feng, W. Qin, Y-.Z. Wang, X-.T. Hao and K.P. Ghiggino, *Organic Electronics* **44** (2017) 149-158.

[45] C.H. Garcia-Escobar, M.E. Nicho, H. Hu, G. Alvarado-Tenorio, P. Altuzar-Coello, G. Cadenas-Pliego and D. Hernandez-Martinez, *Int. J. Polym. Sci.* (2016) 1-9.

It's written in scars and it's written in the stars.

Chapter 9: Summary and Future Work

9.1 Summary

In the research work carried out in this thesis, we were able to tackle some of the challenges in the preparation of materials and their use in development of cost effective organic photovoltaic cells. Multiple studies have been conducted to tackle energy related issues using graphene as an electron acceptor. However, our work focused on graphene derivative (graphene oxide) with its superior structural and spectroscopic properties as an electron acceptor. The main goal was to form GO/P3HT, HoGO/P3HT, and GO/ZnO/P3HT layered nanostructures with engineered interface for efficient optical absorption, charge carrier mobility and higher light-to-electric efficiency in organic photovoltaic cells. The simple synthesis routes for nanomaterials preparation and environmentally friendly deposition methods for thin film growth were adopted. In order to achieve our set goals, we systematically characterized the developed layered nanostructures using structural, morphological, spectroscopic and electrical techniques.

The interaction between drop cast GO/P3HT thin films and doping with Ho affected the structural, optical and luminescent properties of the thin films. The interaction was confirmed through shifting of the diffraction peak and derivatization of edge carboxyl and surface hydroxyl functional groups through the formation of amide vibrational frequencies. Upon doping with Ho, the crystalline entities of P3HT were hampered leading to less ordering of moieties. The crinkly and flaky surface morphology resembled the presence of GO within the P3HT matrix as a result of intimate contact between their basal planes. This intimate contact led to disordering of P3HT chains which caused an increase in absorption. Furthermore, Ho incorporation played a pivotal role by increasing absorption over a wide spectral range. The PL emission spectra revealed that GO confines the photoemission coming from P3HT hence the emission quenching symbolic of charge transfer process.

The investigation on deposition of donor P3HT using various deposition methods (that led to various thicknesses) was necessary to ensure good quality and scalable thin film before fabrication of devices. In the comparative study, structural and optical properties illustrated favourable results in terms of thicker P3HT thin film thickness with potential for efficient charge transportation. The calculated full width at half maximum (FWHM) values decreased with the increase in thin film thickness which shows that crystallinity increases with thin film

thickness. We witnessed a correlation between XRD and SEM results following which, particle morphology increases with thin film thickness. The structural analysis from Raman revealed suppressed C-C mode relative to C=C mode which shows higher ordering with respect to thicker thin film. The increase in thickness of P3HT thin film led to enhanced optical property with reasonable energy band gap alignment. A gradual increment of emission intensity with the increase in thin film thickness was observed as a result of the increase in the number of defect states.

Because of uniformity and reproducibility of thin films produced using spin coating method, we adopted the aforementioned method for device fabrication. XRD results presented pure formation of P3HT, ZnO and GO nanomaterials without impurities and we employed those materials for growing GO/P3HT, ZnO/P3HT and GO/ZnO/P3HT layered nanostructures. The average crystallite size for ZnO, ZnO/P3HT and GO/ZnO/P3HT layered nanostructures was found to be 4.54, 4.51 and 4.50 nm, respectively confirming their nano property. Other than peaks coming from the substrate, the EDS entails intense peaks of C, O, and Zn elements, confirming the formation of GO/ZnO/P3HT layered heterostructure. The results from FTIR confirmed the interaction by the reduction of relative intensity of some vibrational frequencies of P3HT and the emergence of oxygen containing groups leading to a decrease in conjugation length. The absorption measurements of multi-layered structures were found to improve leading to modification of band gap energy. Improved electron mobility from P3HT to GO was observed through the reduced lifetime of GO/P3HT nanostructure. As such, *J-V* measurements confirmed the increase in charge mobility by the improvement of J_{SC} for GO/P3HT device. The PL investigation revealed that ZnO and GO layers were efficient quenchers of P3HT emission with the increase in quenching efficiency values. This shows that P3HT donated the charges that were redistributed by ZnO within GO/ZnO/P3HT layered nanostructures as an optical spacer for absorption optimization and transportation to the acceptor. The current density-voltage (*J-V*) characteristics shows that the device structure is functional leading to improved performance of ZnO/P3HT photovoltaic cells. The devices based on GO/P3HT and GO/ZnO/P3HT resembled efficiency deterioration as a result of irregular interface upon incorporating GO that lead to low interconnectivity for carrier transport. In any case, the process followed is compatible with low cost heterojunction organic solar cell device fabrication at a reduced process time, which is more beneficial for actual mass production.

9.2 Future work

Graphene as promising nanomaterial for various optoelectronic applications has many challenges including synthesis, characterization, application etc. Although a lot of effort have been made on growth of layered nanostructures and their use in fabrication of solar cell devices, only limited improvement has been seen on achieving a working device. This prompts studies for modification of GO as an acceptor material to get changes in its energy levels. In view of excellent electronic properties of reduced graphene oxide (rGO) such as high electron mobility and well dispersion ability in organic solvents, we opt to use rGO as an acceptor material in future. The controlled modification of GO is very important to safeguard the material characteristics while extending the use of graphene in solar cell devices. To construct high-performance heterostructure for organic solar cells using GO as the hole extraction layer (HEL), the conductivity of GO layer must be highly improved by reduction method. Thus, to obtain efficient photovoltaic cells we need to tailor our materials such that they possess relatively high charge mobility and large donor-acceptor (D-A) for efficient exciton dissociation and transport.

"There is always something new to learn and there is always a new adventure around the corner"

- Odyssey

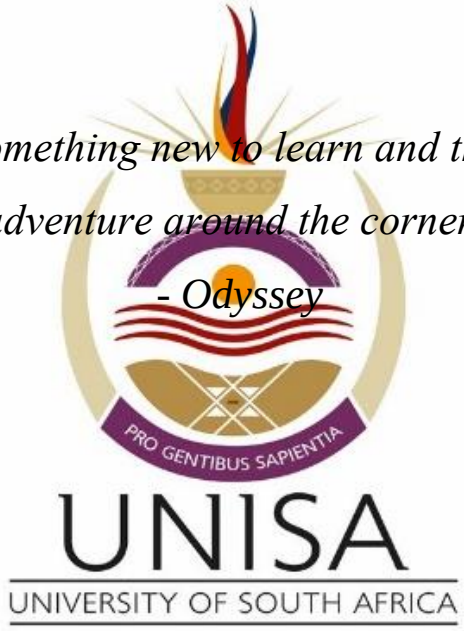

9.3 Publications

1. F.V. Molefe, B.M. Mothudi, M.S. Dhlamini, Interactions in GO/P3HT layered nanostructures: Spectroscopic investigation for organic solar cells. *Chemical Physics Letters* **x** (2023) xxx-xxx. (Submitted).
2. Sefako John Mofokeng, Fokotsa V. Molefe, Luyanda L. Noto, Robin E. Kroon, Hendrick C. Swart, Mokhotjwa S. Dhlamini, Up-conversion luminescence properties of Er^{3+}/Yb^{3+} co-doped $ZnTiO_3$ thin films synthesized by pulsed laser deposition, *Heliyon* (2023) (Accepted).
3. S.J. Mofokeng, F.V. Molefe, L.L. Noto, M.S. Dhlamini, **The Luminescence properties of Up-and-Down-Converting Rare Earth Ions Doped $ZnTiO_3$ Nanoparticles**, *Jenny Stanford Publishing Pte. Ltd., ISBN 9781003277385 (Hardcover), 978-1-000-00000-0 (eBook),* (2022) 281-298.
4. Luyanda L. Noto, Sefako J. Mofokeng, Fokotsa V. Molefe, Hendrik C. Swart, Angelina S. Tebele, Mokhotjwa S. Dhlamini, **Luminescent dynamics of Rare Earth doped $CaTiO_3$ phosphors**, *Spectroscopy of Lanthanide Doped Oxide Materials*, *Woodhead Publishing Series in Electronic and Optical Materials* (2020) 57-86.
5. F.V. Molefe, S.J. Mofokeng, M. Khenfouch, M. Achehboune, M.S. Dhlamini, B.M. Mothudi, L.F. Koao, **The effect of Zn^{2+} on the anion vacancies in ZnO thin-films grown using chemical bath deposition**. *Journal of Physics: Conf. Series* **1292** (2019) 012016.
6. Fokotsa V. Molefe, Luyanda L. Noto, Mokhotjwa S. Dhlamini, Bakang M. Mothudi, Victor R. Orante-Barrón, **Structural, photoluminescence and thermoluminescence study of novel Li^+ co-activated lanthanum oxide activated with Dy^{3+} and Eu^{3+} obtained by microwave-assisted solution combustion synthesis**, *Opt. Mat.* **88** (2019) 540-550.
7. F V Molefe, M Hamzah, M Khenfouch, M S Dhlamini and B M Mothudi, **Growth and characterization of hybrid (HoGO/P3HT) graphene-based nanostructures for photovoltaic (PV) applications** *Journal of Physics: Conf. Series* **984** (2018) 012003.
8. Fokotsa V. Molefe, Luyanda L. Noto, Mduduzi Mbongo, Mokgaotsa J. Mochane and Mokhotjwa S. Dhlamini, **Organic waste converted into energy producing and storing systems, "Waste-to-Profit (W-t-P)"**, *Nova Science Publishers, Inc.* 2018 *ISBN*: 978-1-53613-235-9 (pp.83-106)

9. Fokotsa V. Molefe, Mohammed Khenfouch, Mokhotjwa S. Dhlamini, Bakang M. Mothudi, **Spectroscopic investigation of charge and energy transfer in P3HT/GO nanocomposite for solar cell applications** *Advanced Materials Letters* **8** (2017) 246-250.
10. L.L. Noto, F.V. Molefe, P.S. Mbule, G. Kabongo, M. Khenfouch, B.M. Mothudi, M.S. Dhlamini, **Nanotechnology, Nanomaterials and Thin Films for Energy Applications, "Science and applications of Tailored Nanostructures",** *One Central Press (OCP), 2016 ISBN (eBook): 978-1-910086-19-3.*
11. Fokotsa V. Molefe, Lehlohonolo F. Koao, Birhanu F. Dejene, Hendrik C. Swart **Phase formation of Hexagonal wurtzite ZnO through decomposition of $Zn(OH)_2$ at various reaction temperatures using CBD method** *Opt. Mater.* **46** (2015) 292-298.
12. Molefe F.V, Koao L.F, Dejene B.F, Swart H.C. **Influence of zinc acetate concentration in the preparation of ZnO nanoparticles via chemical bath deposition** Proceedings of SAIP ISBN: 978-0-620-65391-6 (2015) 79 – 84.
13. F.V. Molefe, L.F. Koao, J.J. Dolo, B.F. Dejene. **Effect of reaction time on structural, morphology and optical properties of ZnO nanoflakes prepared by chemical bath deposition method** *Physica B.* **439** (2014) 185 – 188.

9.4 Research Presentations

1. F.V. Molefe, S.J Mofokeng, M. Khenfouch, M. Achehboune M.S. Dhlamini, B.M. Mothudi, L.F. Koao **The effect of Zn^{2+} on the anion vacancies in ZnO thin films grown using CBD,** 1st International Online Conference on Nanoscience and Nanotechnology 2nd Edition,(N@NO'2018) 29-30 December 2018.
2. F.V. Molefe, M. Khenfouch, M.S. Dhlamini, B.M. Mothudi **Interactions in GO/P3HT layered nanostructures: Spectroscopic investigation for solar cells application**, NANOSMAT-AFRICA, Western Cape, 19 – 23 November 2018.
3. F.V. Molefe, M. Khenfouch, M.S. Dhlamini, B.M. Mothudi **Hybrid GO/ZnO/P3HT heterojunction devices for solar cell applications**, 8th Annual Symposium of SANi-NYRS 16 November 2018 Vaal University of technology.
4. F.V. Molefe, S.J. Mofokeng, L.L. Noto, M.S. Dhlamini, B.M. Mothudi, **Luminescent materials to enhance the efficiency of Photovoltaic Solar Cells**, 3rd Young Scientist

Forum – BRICS Southern Sun Hotel Durban, 25-29 June 2018 (International Conference).

5. F.V. Molefe, M. Khenfouch, M.S. Dhlamini, B.M. Mothudi **P3HT/GO nanolayer for photovoltaic applications,** 1st International Online Conference on Nanoscience and Nanotechnology (N@NO'2017) 02-03 December 2017.
6. F.V. Molefe, M.S. Dhlamini, B.M. Mothudi **Luminescence study on Li^{+} co-activated La_2O_3 activated with Dy^{3+} and Eu^{3+}**, 7th Annual Symposium of SANi-NYRS 20th October 2017 Tshwane University of technology.
7. F.V. Molefe, M. Khenfouch, M.S. Dhlamini, B.M. Mothudi **Simple approach to growth and characterization of GO/ZnO/P3HT layered nanostructures for solar cell devices** 62nd Annual conference of the SAIP Stellenbosch University, 3-7 July 2017 (National Conference).
8. F.V. Molefe, M. Khenfouch, M.S. Dhlamini, M. Maaza, B.M. Mothudi **Spectroscopic investigation of interactions in P3HT/GO layered nanostructures for solar cells application** International Conference on Materials & Environmental Science, December 1-3, 2016 Oujda, Morocco (International conference).
9. F.V. Molefe, M.S. Dhlamini, B.M. Mothudi **Steady state and time resolved measurements on ZnO nanoflakes**, 6th Annual Symposium of SANi-NYRS 18 November 2016 Mintek.
10. F.V. Molefe, M. Khenfouch, M.S. Dhlamini, M. Maaza, B.M. Mothudi **Spectroscopic investigation of charge and energy transfer in P3HT/GO nanocomposites** 61st Annual conference of the SAIP University of Cape Town, 4-8 July 2016 (National Conference).
11. Molefe F.V, Koao L.F, Dejene B.F, Swart H.C. **Influence of zinc acetate concentration in the preparation of ZnO nanoparticles via chemical bath deposition** 59th Annual Conference of the SAIP University of Johannesburg, 7-11 July 2014 (National Conference).
12. F.V. Molefe, L.F. Koao, J.J. Dolo, B.F. Dejene. **Effect of reaction time on structural, morphology and optical properties of ZnO nanoflakes prepared by chemical bath deposition method** *Physica B.* **439** (2014) 185 – 188 5th South African Conference on Photonic Materials (SACMP 2013), Kariega, South Africa, 2013 (International conference)

Research is a key; it tremendously expands our thinking capacities and fuel enthusiasm to learn more and invent.